DYNAMIC BEHAVIOUR OF THE HIGH CONFINEMENT MODE OF FUSION PLASMAS

Hartmut Zohm

IPP 1/286 May 1995

MAX-PLANCK-INSTITUT FÜR PLASMAPHYSIK

85748 GARCHING BEI MÜNCHEN

MAX-PLANCK-INSTITUT FÜR PLASMAPHYSIK

GARCHING BEI MÜNCHEN

DYNAMIC BEHAVIOUR OF THE HIGH CONFINEMENT MODE OF FUSION PLASMAS

Hartmut Zohm

IPP 1/286 May 1995

Die nachstehende Arbeit wurde im Rahmen des Vertrages zwischen dem Max-Planck-Institut für Plasmaphysik und der Europäischen Atomgemeinschaft über die Zusammenarbeit auf dem Gebiete der Plasmaphysik durchgeführt.

This paper describes the dynamic behaviour of the High Confinement mode (H-mode) of fusion plasmas, which is one of the most promising regimes of enhanced energy confinement in magnetic fusion research. The physics of the H-mode is not yet fully understood, and the detailed behaviour is complex. However, we establish a simple physics picture of the phenomenon. Although a first principles theory of the anomalous transport processes in a fusion plasma has not yet been given, we show that within the picture developed here, it is possible to describe the dynamic behaviour of the H-mode, namely the dynamics of the L-H transition and the occurrence of edge localized modes (ELMs).

Contents

Chapter 1

Introduction

1.1 Controlled Nuclear Fusion

The aim of controlled nuclear fusion research is to generate energy from fusion of light nuclei. There are a lot of possible fusion reactions, but the most prominent ones are

$$p + p = D + e^+ + \nu_e + 1.5 \text{ MeV} \quad (1.1)$$

$$D + p = {}^3\text{He} + \gamma + 5.4 \text{ MeV} \quad (1.2)$$

$${}^3\text{He} + {}^3\text{He} = {}^4\text{He} + 2p + 12.9 \text{ MeV} \quad (1.3)$$

$$D + D = p + T + 4.032 \text{ MeV} \quad (1.4)$$

$$D + D = n + {}^3\text{He} + 3.27 \text{ MeV} \quad (1.5)$$

$$D + T = {}^4\text{He} + n + 17.6 \text{ MeV} \quad (1.6)$$

$$D + {}^3\text{He} = {}^4\text{He} + p + 18.4 \text{ MeV} \quad (1.7)$$

Reactions (1.1), (1.2) and (1.3) provide the sun's energy source. Due to the weak interaction processes involved in reaction (1.1), the cross-section for the whole cycle is low compared with the reactions (1.4) to (1.7). Thus, for controlled nuclear fusion on earth, only the latter two are possible. The most suitable one is (1.6). Here, a resonant metastable state is formed (^{5}He) providing the highest cross-section of all fusion reactions. In addition, the energy gain is high.

Reaction (1.7) has the advantage that all nuclei are stable and no neutrons are generated (a high neutron flux leads to technological problems with wall materials). However, the cross-section is lower by a factor of 10-100 compared to the $D-T$ reaction. Thus, in today's experiments, it is not considered a suited candidate for generating fusion energy. Fig. 1.1 shows the different cross-sections σ_{Fus} as a function of the kinetic energy of the nuclei in the center-of-mass system.

The realisation of fusion reactions is difficult because the cross-section for elastic Coulomb scattering is higher than σ_{Fus} by a factor of 10^4 at 10 keV and even higher at lower

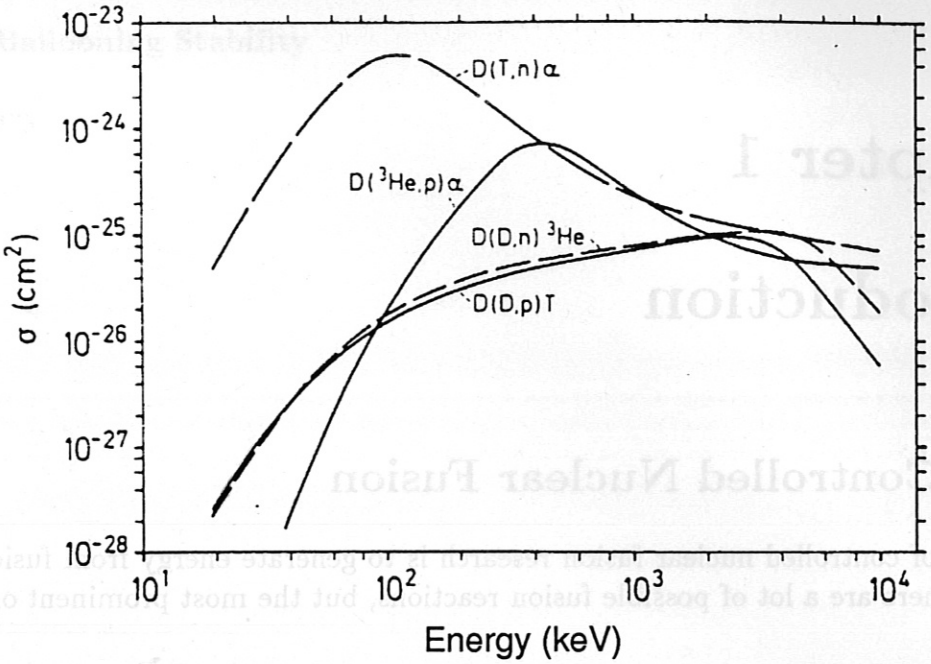

Figure 1.1: *Cross-section σ_{Fus} for different fusion reactions as function of the kinetic energy of the nuclei.*

temperatures. Therefore, the particles must be confined to a volume long enough in order to perform many collisions. This is the reason why crossed particle beams are not suited for generating fusion energy; the kinetic energy of the particles has to be *thermal* energy. The fusion reaction rate is obtained by averaging the cross-section σ_{Fus} over the velocity distribution of the particles. In a thermal plasma, the distribution is Maxwellian and the parameter $< \sigma_{Fus}\, v >$ has a broad maximum at $T \approx 10 - 50$ keV (in fusion research, temperatures are usually expressed in eV, i.e. 1eV $\equiv$ 11600 K). At these temperatures, the hydrogen gas becomes fully ionized, i.e. a plasma. Thus, the goal of nuclear fusion is to produce and control a thermal plasma of $T \geq 10$ keV. In present experiments, a $D - D$ mixture is used, but for a burning plasma, $D - T$ isrequired.
In order to ignite a $D-T$ plasma, the energy loss from the plasma has to be compensated by the fusion power. The neutrons generated in the fusion reaction escape from the plasma without further interaction so that only the fusion generated α-particles directly contribute to plasma heating. Thus, the requirement for an ignited hydrogen plasma ($n_D = n_T = n_e/2$) can be written as (see e.g. [Wesson, 1987])

$$P_{loss} \leq P_\alpha \quad \rightarrow \quad \frac{3 n_e k T}{\tau_E} + \text{const.} n_e^2 \sqrt{kT} \leq \frac{1}{4} n_e^2 \langle \sigma_{Fus}\, v \rangle E_\alpha \tag{1.8}$$

We have characterized the energy loss from the plasma by conduction and convection through the empirical quantity τ_E, the energy confinement time

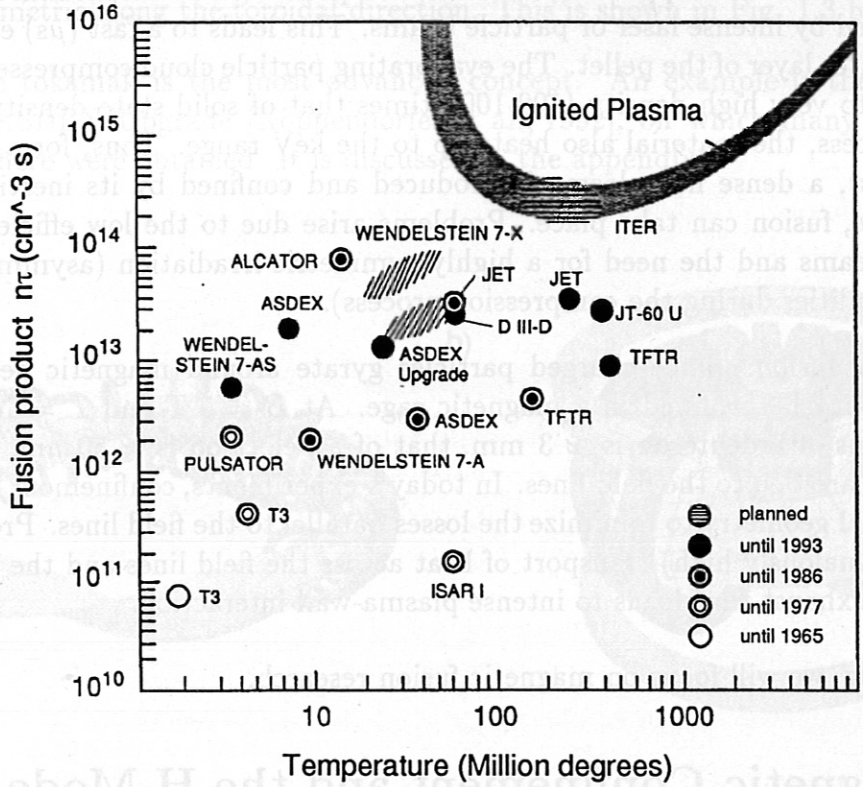

Figure 1.2: *Experimentally obtained values of $n\tau_E$ in several magnetic confinement experiments as a function of temperature.*

$$\tau_E = \frac{W}{P - dW/dt} \tag{1.9}$$

where W is the energy content of the plasma. The second loss term in (1.8)is the loss by bremsstrahlung radiation.

Evaluation of Eqn. (1.8) shows that, for given T (and therefore fixed $\langle \sigma_{Fus} v \rangle$), the figure of merit is the product of density and energy confinement time. Under the constraint of a fixed plasma pressure, this function has a minimum at $T \approx 10 - 15$ keV. At this optimum temperature, a detailed study of the criterion for ignition yields $n\tau_E > 1.6 \times 10^{20}$ m^{-3} s. However, a non-zero impurity content of the D-T plasma leads to fuel dilution and additional bremsstrahlung and line radiation losses (for a detailed study, see [Reiter et al., 1990]). Therefore, the impurity content has to be kept as low as possible. Fig. 1.2 gives an overview of $n\tau_E$ values obtained in today's experiments. In addition, the ignition curve for a pure D-T plasma is shown. For experiments that do not obtain the optimum temperature, the figure of merit is sometimes expressed as the triple product $nT\tau_E$, also called the 'fusion product'.

In fusion research, two different approaches are investigated to achieve an ignited plasma:

- *Inertial Fusion:* This approach uses small D-T pellets (radius in the mm range) that are heated by intense laser or particle beams. This leads to a fast (μs) evaporation of the outer layer of the pellet. The evaporating particle cloud compresses the inner volume to very high density (100-1000 times that of solid state density). During this process, the material also heats up to the keV range. Thus, for a very short time (μs), a dense hot plasma is produced and confined by its inertia. During this time, fusion can take place. Problems arise due to the low efficiency of the driver beams and the need for a highly symmetric irradiation (asymmetries lead to instabilities during the compression process).

- *Magnetic fusion:* Since charged particles gyrate around magnetic field lines, a plasma may be confined in a magnetic cage. At $B = 5$ T and $T = 10$ keV, the gyroradius of a deuteron is ≈ 3 mm, that of an electron is ≈ 50 μm. Thus, the particles are tied to the field lines. In today's experiments, confinement is achieved in toroidal geometry to minimize the losses parallel to the field lines. Problems are the (anomalously high) transport of heat across the field lines and the power and particle exhaust that leads to intense plasma-wall interaction.

In the following, we will focus on magnetic fusion research.

1.2 Magnetic Confinement and the H-Mode

The idea of magnetic confinement of a fusion plasma first led to linear machines, where the magnetic field lines end on a material wall. Even if special care is taken of the field geometry at the wall (e.g. magnetic mirrors to reflect particles), these devices suffer from end losses. To overcome these problems, magnetic confinement today is mostly realized in toroidal devices. For reasons of stability, these consist of a strong toroidal field and a weaker poloidal component, so that the field lines helically wind around the torus and form the so-called magnetic surfaces. An example can be seen in Fig. 1.3.

As the particles can move freely along the field lines, but gyrate around them at radii in the millimeter range and below, density and temperature are constant on the magnetic surfaces but can exhibit large gradients from the hot plasma centre to the outer boundary perpendicular to the magnetic surfaces.

Today, two major lines of toroidal magnetic confinement devices exist. They are distinguished by their symmetry and the way the magnetic field is produced:

- In the *Stellarator*, all fields are produced by coils. An optimization procedure for best stability and transport properties leads to a concept in which the shape of the plasma cross-section varies along the toroidal cross-section. An example for a stellarator configuration is shown in Fig. 1.3 a).

- In the *Tokamak*, the toroidal field component is produced by coils. The poloidal component comes from a strong toroidal current induced in the plasma via the

action of a transformer (normally a central solenoid). Thus, the tokamak is axisymmetric along the toroidal direction. This is shown in Fig. 1.3 b)

Today, the tokamak is the most advanced concept. An example is the tokamak experiment ASDEX Upgrade [Köppendörfer et al., 1992], on which many of the results presented here were obtained. It is discussed in the appendix.

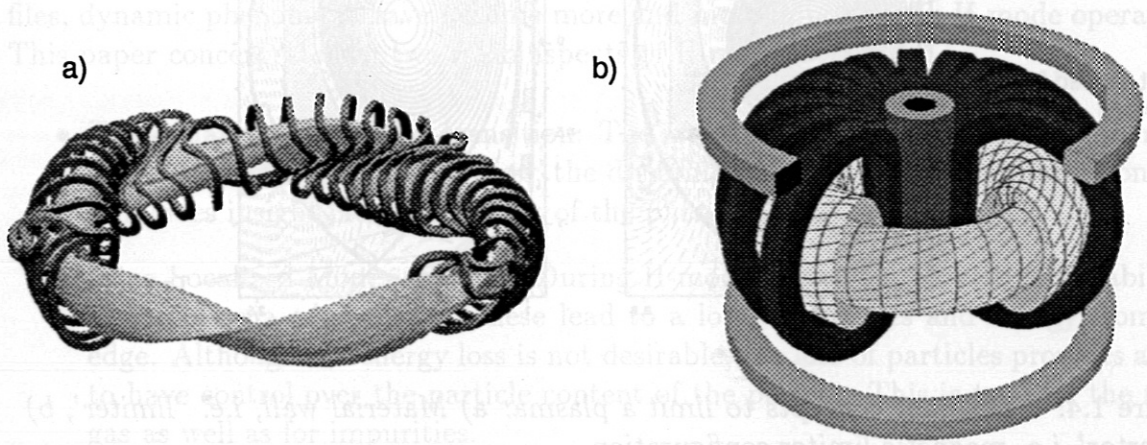

Figure 1.3: *Schematic of a stellarator (a) and a tokamak (b).*

A major problem in fusion research is the interaction of the plasma with the wall; this is strongly connected with the need to exhaust of particles and energy from the plasma in a controlled manner. The simplest approach to this problem is the limitation of the plasma by a material wall, i.e. a so-called 'limiter' (see Fig. 1.4 a)). This has the disadvantage that the plasma-wall interaction leads to the production of impurities (normally of the limiter material, e.g. carbon) that enter the plasma and lead to fuel dilution and radiation losses. In present tokamaks, heat and particles are removed by means of a so-called 'divertor', i.e. a magnetic configuration in which energy and particles passing the last closed magnetic surface, the so-called 'separatrix', are guided along field lines to target plates localized far away from the hot core plasma (see Fig. 1.4 b)). Thus, the impurity production by plasma wall interaction is located far away from the core plasma and the probability for an impurity atom to penetrate the plasma is much lower. In addition, the divertor region can be pumped to obtain good particle control. Finally, the long way along field lines into the divertor region opens up the possibility to remove some of the particle's energy before it hits the target plate, thus reducing erosion and sputtering. This can be done e.g. by enhancing radiation losses due to the injection of additional impurities.

The divertor configuration leads to another beneficial effect: in limiter tokamaks it was found that the energy confinement time τ_E reaches values much lower than those predicted by theories based on binary collisions. Including the effects of toroidal geometry

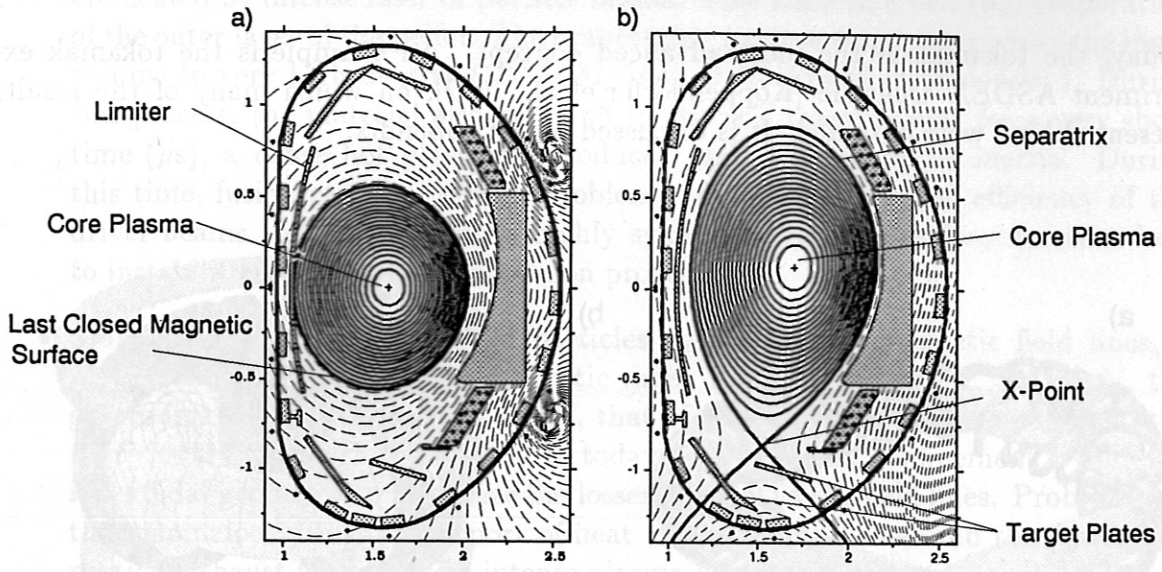

Figure 1.4: *Different concepts to limit a plasma: a) Material wall, i.e. 'limiter', b) 'divertor', i.e. magnetic limiter configuration.*

(so-called 'neoclassical transport') leads to transport coefficients that are insufficient to explain the experimentally observed transport coefficients. In particular, the electron heat conductivity is found to be enhanced by a factor of $\approx 10 - 100$ with respect to neoclassical values. This phenomenon has been dubbed 'anomalous transport'. It is believed that it is due to turbulent fluctuations of the plasma. In this case, binary collisions are not an appropriate description and a hydrodynamic approach has to be undertaken. Work on this subject is still in progress.

In the experiment, anomalous transport manifests itself in particular in the occurrence of the so-called L(low confinement)-mode regime. Here, the confinement time is found to roughly scale proportional to the plasma current I_p, but inversely with the square root of the heating power P. By using the divertor operation, a new regime of improved confinement was found in the ASDEX tokamak [Wagner et al., 1982]. This is the so-called H(high confinement)-mode. It is characterized by a parameter dependence similar to the L-mode, but an increased absolute value of the confinement time:

$$f_H = \tau_{E,H}/\tau_{E,L} \approx 2 \tag{1.10}$$

Note that this is still much smaller than the value predicted by transport theory based on binary collisions (i.e. the anomalous transport is reduced but not fully suppressed).

As pointed out above, at fixed T_i, the figure of merit for fusion is $n\tau_E$. Usually, τ_E is increased by increasing the machine size; an improved confinemnet will thus lead to a smaller unit size for a future reactor. In the present experiments, operation in the H-

mode leads to higher performance in a given device at fixed heating power and density. For example, the next step to be undertaken on the path to a fusion reactor, ITER (International Thermonuclear Experimental Reactor), is based on H-mode operation. It is therefore desirable to characterize and understand the H-mode in detail.

Analysis of H-mode discharges shows that the confinement improvement cannot be described by a global decrease of transport coefficients, but is characterized by an edge transport barrier where large gradients of density and temperature can be sustained (see e.g. Ref. [The ASDEX Team, 1989]). In addition to the analysis of the steady-state profiles, dynamic phenomena have become more and more important in H-mode operation. This paper concentrates on two main aspects of H-mode dynamics:

- The dynamics of the L-H transition: The transition from low to high confinement shows signatures of a bifurcation; the dynamical behaviour of this bifurcation system gives insight into the physics of the phenomenon.
- Edge Localized Modes (ELMs): During H-mode operation, repetitive instabilities of the plasma edge occur. These lead to a loss of particles and energy from the edge. Although the energy loss is not desirable, the loss of particles provides a tool to have control over the particle content of the plasma. This is true for the main gas as well as for impurities.

The paper is therefore organized as follows: In Chapter 2, an overview of the experimental signatures of the H-mode as well as a description of existing theoretical models to explain the H-mode is given. Chapter 3 deals with the dynamic behaviour of the L-H transition and gives a tentative explanation of the phenomena observed on the grounds of the theory discussed in Chapter 2. In Chapter 4, the experimental characterization of ELMs is discussed; a general classification valid for many tokamak experiments is given. Also, theoretical ideas about the ELM mechanisms are discussed. In Appendix A, the tokamak experiment ASDEX Upgrade is described. Appendix B reviews transport in a torus. The ideal ballooning stability analysis which is important for the understanding of ELMs is discussed in Appendix C and in Appendix D, a glossary lists words and definitions which may not be familiar to the reader.

Chapter 2

The H-Mode

Since the H-mode was discovered in the ASDEX tokamak [Wagner et al., 1982], it has been found in many other experiments operating in a divertor configuration. However, it was also found in limiter discharges in the TFTR tokamak. Thus, divertor operation is helpful to obtain the H-mode, but it does not seem to be a necessary requirement. In addition, H-mode behaviour was also seen in the WVII-AS stellarator [Erckmann et al., 1993] and the HIEI mirror machine [Sakai et al., 1993]. Thus, it is a very general feature of magnetically confined fusion plasmas.

There are several regimes of improved confinement, many of them achieved only in transient states without external particle control [Mertens et al., 1990]. In contrast, the H-mode offers a possibility of steady state operation with good particle control. We will now characterize the main physics aspects of the H-mode and give a review of H-mode theories. The discussion follows the review given in [Zohm et al., 1994c].

Recently, a regime in which confinement is improved even with respect to normal H-mode operation has been found (so-called VH-mode [Jackson et al., 1991]). This regime seems to have many features in common with the H-mode; however, a discussion is beyond the scope of this work.

2.1 Experimental Characterization

Generally, it is found that the transition from L- to H-mode confinement occurs when a certain heating power is exceeded during a discharge. An example from the ASDEX Upgrade tokamak is shown in Fig. 2.1. The transition is seen in the increase of density and stored energy as well as in the reduction of the flux of particles out of the plasma. This reduction of flux is most prominently seen on the divertor D_α-emission, i.e. the intensity of the Balmer-α line of Deuterium in the divertor. This quantity is roughly proportional to the amount of recycling particles in the divertor, and therefore a good indicator of the particle flux from the plasma.

In Fig. 2.1, two discharges are shown. On the left side, energy and density increase until the discharge drops back to the L-mode. On the right side, a repetitive edge instability

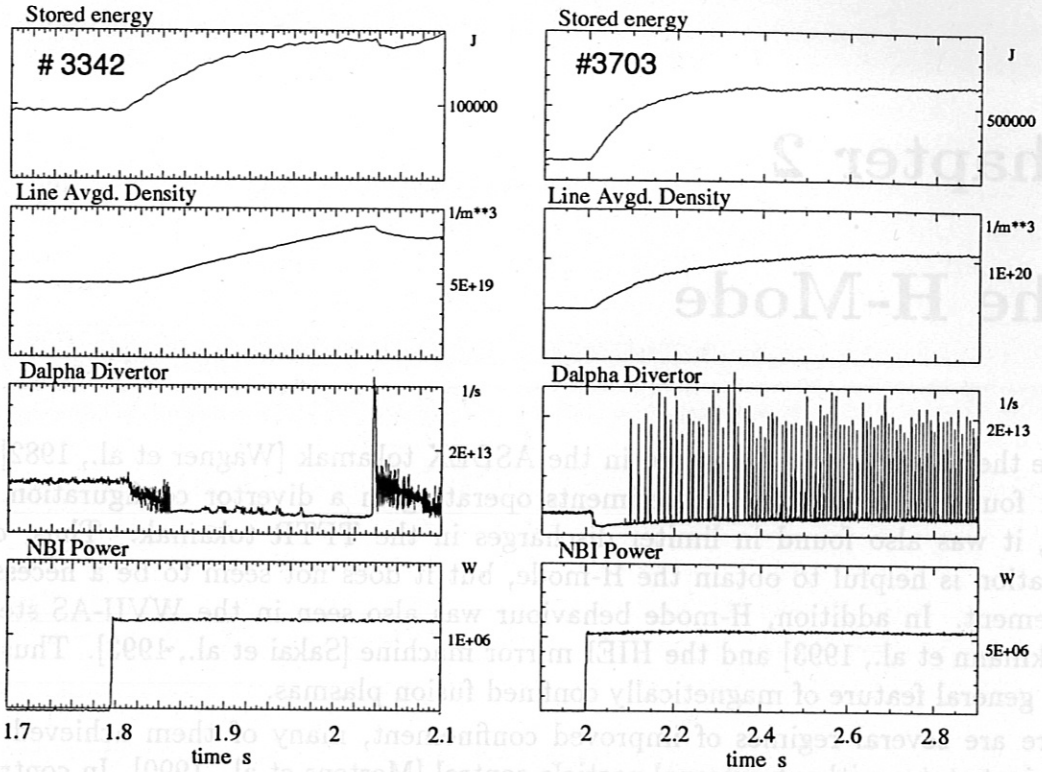

Figure 2.1: *Typical time traces for H-mode discharges; the L-H transition is seen in the increase in stored energy and density as well as in the reduction of the particle flux out of the plasma (marked by the D_α-trace). On the right side, the occurrence of ELMs leads to a stationary state.*

develops (ELM = Edge Localized Mode) that expels particles and energy on a fast timescale of ≤ 1 ms (leading to short bursts in the D_α-emission). It can be seen that the ELMing discharge becomes stationary. A detailed description of ELMs and the ELMy H-mode is given in chapter 4.

2.1.1 The L-H Transition and the Power Threshold

As shown in the example above, the L-H transition is characterized by a threshold in the heating power P_{thr}^{LH}. As future experiments plan to operate in the H-mode, it is desirable to have a prediction of the heating power needed to transit into the H-mode. As no quantitative theory exists to describe the L-H transition, a statistical analysis is done to determine the dependence of P_{thr}^{LH} on plasma parameters and machine size and geometry. In many tokamaks, it has been found that P_{thr}^{LH} is roughly proportional to the product of line averaged electron density $\bar{n}_e$ and toroidal magnetic field B_t. In the Section 2.2, it will be shown that knowledge of B_t, the edge density $n(a)$ and temperature $T(a)$ may suffice to

determine the L-H transition. As these parameters are not easily accessible in the experiment, one may assume that $n(a)$ is proportional to $\bar{n}_e$ and, at fixed $\bar{n}_e$, $T(a)$ is determined by the energy flux through the plasma edge. Therefore, an attempt to scale between tokamaks of different size was done by normalizing the heating power P with the plasma surface area S [H-mode Database Working Group, presented by O. Kardaun, 1992]. A well-documented scaling for P/S was established on the ASDEX Upgrade tokamak [Ryter et al., 1994]:

$$P_{thr}^{LH}/S = (0.038 \pm 0.002)\bar{n}_e B_t \ [\mathrm{MW, m^{-2}}, 10^{20}\mathrm{m^{-3}}, \mathrm{T}] \tag{2.1}$$

However, P_{thr}^{LH} depends sensitively on many experimental parameters (e.g. wall conditioning) so that (2.1) must be regarded as today's lower bound on P_{thr}^{LH} in tokamaks. Also, stellarators seem to follow this scaling law with a prefactor of 0.032 for WVII-AS [Wagner, 1994].

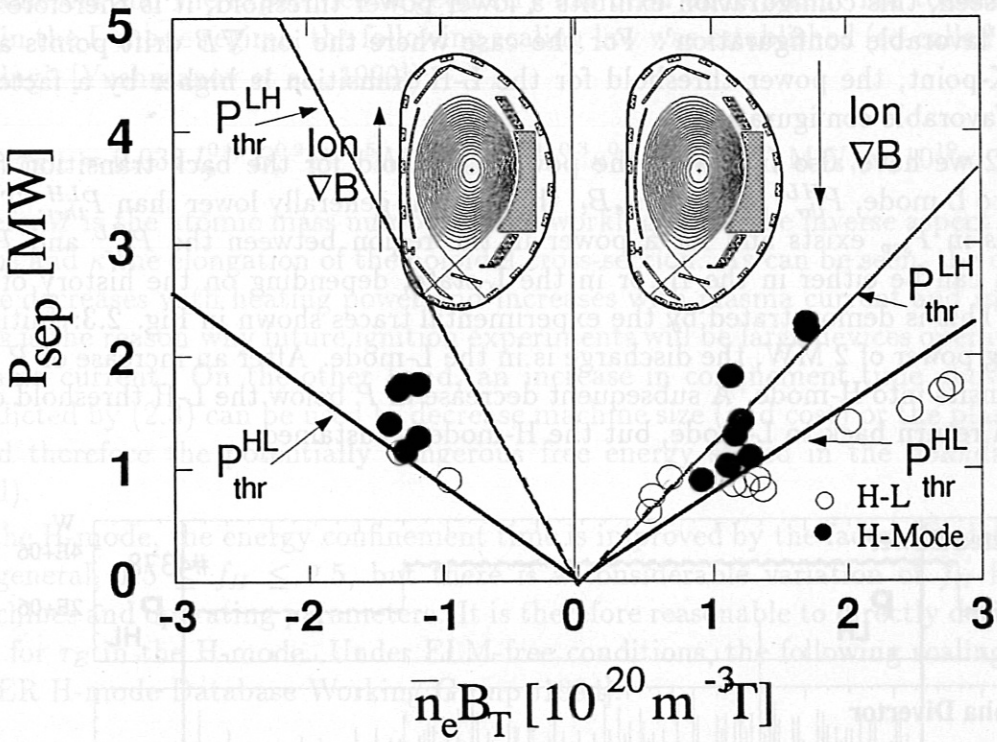

Figure 2.2: *H-mode operational diagram for ASDEX Upgrade. The power threshold for the L-H and the H-L transition is shown for both values of the ion ∇B drift. A hysteresis in P_{sep} exists.*

Following the idea that the energy flux through the plasma edge (i.e. across the separatrix for divertor configurations) is the parameter governing the L-H transition, it is reasonable to correct P for changes in the energy content (i.e. heating power deposited in the plasma

that does not lead to an energy flux across the separatrix) and for the radiated power inside the separatrix $P_{rad}(core)$. The latter term is important in situations where the radiated power is varied experimentally, e.g. by injection of impurities. Thus, the H-mode operation diagram of a tokamak can be expressed in terms of P_{sep} versus $\bar{n}_e B_t$ where the energy flux across the separatrix is defined by

$$P_{sep} = P - dW/dt - P_{rad}(core) \tag{2.2}$$

Fig. 2.2 shows the operational diagram for ASDEX Upgrade. All experimental data were obtained in the lower single-null configuration, as indicated by the reconstructed flux surfaces in Fig. 2.2. On the $\bar{n}_e B_t$-axis, we have separated the points for the two possible orientations of the toroidal magnetic field with respect to the X-point. Positive values correspond to the configuration where B_t, when viewed from above, runs counter-clockwise. In this case, the vertical drift of the ions due to curvature and gradient of the magnetic field in the torus, the so-called ∇B drift, is directed towards the X-point. As can be seen, this configuration exhibits a lower power threshold, it is therefore also called the 'favorable configuration'. For the case where the ion ∇B drift points away from the X-point, the power threshold for the L-H transition is higher by a factor of ≈ 1.8 ('unfavorable configuration').

In Fig. 2.2 we have also indicated the power threshold for the back transition from H-mode into L-mode, P_{thr}^{HL}. At fixed $\bar{n}_e B_t$, this value is generally lower than P_{thr}^{LH}. Thus, a *hysteresis* in P_{sep} exists and for a power in the region between the P_{thr}^{HL} and P_{thr}^{LH}, the plasma can be either in the H- or in the L-state, depending on the history of the discharge. This is demonstrated by the experimental traces shown in Fig. 2.3: Initially, at a heating power of 2 MW, the discharge is in the L-mode. After an increase of P to 4 MW, it transits into H-mode. A subsequent decrease in P below the L-H threshold does not cause a return back to L-mode, but the H-mode is sustained.

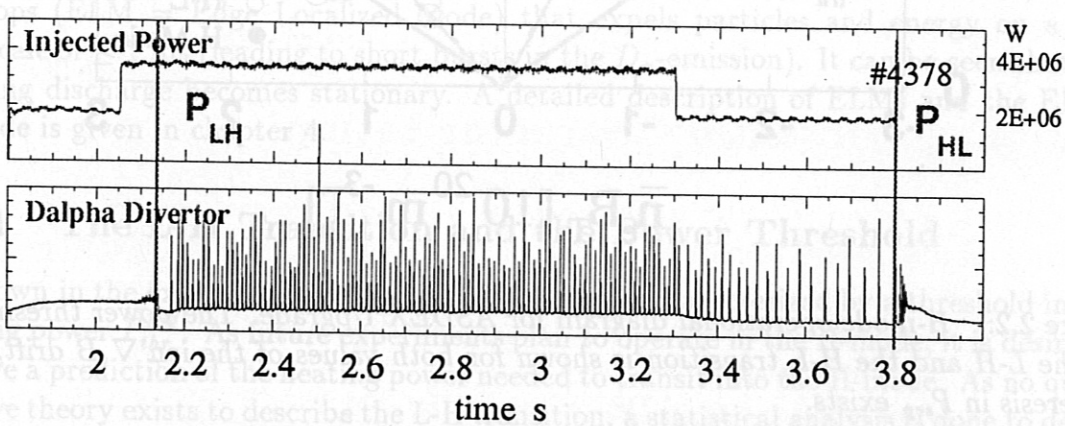

Figure 2.3: *Hysteresis in the power threshold: At 2 MW, the discharge can be either in the L- or H-mode (ASDEX Upgrade shot 4378, 800 kA, +1.8 T).*

Due to the hysteresis, a wider H-mode operational window exists than indicated by P_{thr}^{LH}.

In particular, the density increase occuring at the L-H transition does not necessarily lead to an H-L transition. Also, in contrast to the behaviour of P_{thr}^{LH}, the power threshold for the H-L transition does not significantly change when the ion ∇B drift is reversed. We will come back to these points in chapter 3.

2.1.2 Confinement in the H-Mode

As pointed out above, the heat and particle transport coefficients in fusion plasmas are governed by anomalous transport, i.e. turbulent fluctuations that lead to an energy loss much higher than that estimated by theories based on binary collisions. At present, no quantitative description of anomalous transport exists so that the global energy confinement time τ_E of a given device cannot be estimated from first principles. On the other hand, this number plays a crucial role for ignition as $n\tau_E$ has to reach the value discussed in the previous chapter in order for the plasma to ignite. Similar to the scaling laws derived for the power threshold, statistical analysis of the dependence of τ_E on plasma parameters and the experimental geometry has been undertaken. For tokamaks operating in the L-mode regime, the following scaling law was established (so-called 'ITER89-P scaling', [Yushmanov et al., 1990]):

$$\tau_{E,L} = 0.038\, I_p^{0.85} B_t^{0.2} P^{-0.5} M^{0.5} R^{1.5} \bar{n}_e^{0.1} \epsilon^{0.3} \kappa^{0.5} \ [\mathrm{s, MA, T, MW, m}, 10^{19}\mathrm{m}^{-3}] \qquad (2.3)$$

where M is the atomic mass number of the working gas, ϵ the inverse aspect ratio of the torus and κ the elongation of the poloidal cross-section. As can be seen, the confinement time decreases with heating power and increases with plasma current and machine size. This is the reason why future ignition experiments will be large devices operating at high plasma current. On the other hand, an increase in confinement time above the value predicted by (2.3) can be used to decrease machine size (and cost) or the plasma current (and therefore the potentially dangerous free energy stored in the poloidal magnetic field).

In the H-mode, the energy confinement time is improved by the factor f_H defined above. In general, $1.5 \leq f_H \leq 2.5$, but there is a considerable variation of f_H for different machines and operating parameters. It is therefore reasonable to directly derive a scaling law for τ_E in the H-mode. Under ELM-free conditions, the following scaling was found [ITER H-mode Database Working Group, 1994]:

$$\tau_{E,H} = 0.036\, I_p^{1.06} B_t^{0.32} P^{-0.67} M^{0.41} R^{1.79} \bar{n}_e^{0.17} \epsilon^{-0.11} \kappa^{0.66} \ [\mathrm{s, MA, T, MW, m}, 10^{19}\mathrm{m}^{-3}] \qquad (2.4)$$

As can be seen, the parameter dependence is not too different from that of the L-mode scaling, eq. (2.3). However, the scaling for f_H obtained by dividing (2.4) by (2.3) shows that f_H is not a constant and, when scaled to a big device like ITER, yields a value of $f_H \approx 2.8$ which is higher than that observed in today's experiments. This may be attributed to the fact that (2.4) is a scaling law for the thermal energy content whereas

(2.3) describes the total energy content (i.e. also the fast particle contribution due to the particular heating method). Therefore, a reasonable scaling for f_H can only be given after a scaling law for the thermal energy content in the L-mode has been established. This is a subject of ongoing work. Also, (2.4) applies only to ELM-free conditions. As shown above, stationary H-mode discharges are only achieved in the presence of ELMs. The reduction of τ_E due to the effect of ELMs will be discussed in chapter 4.

Similar to the global energy confinement time, it is straightforward to define a particle confinement time

$$\tau_P = \frac{N}{\Phi_{in} - dN/dt} \tag{2.5}$$

where N is the total particle content and Φ_{in} is the number of particles per second supplied to the plasma. Results from ASDEX showed $\tau_p \approx 3\tau_E$ in the ELM free H-mode and a decrease in this ratio during ELMy H-mode. We will come back to this point in Chapter 4, where the ELMy H-mode is discussed in detail.

However, it is difficult to determine this number experimentally. This is due to the recycling: particles leaving the plasma have a certain probability to re-enter. Thus, the particle source does not only consist of the gas supplied by external control (i.e. gas valve or pellet injection), but also by the inventory of the inner wall of the vacuum chamber. It is therefore reasonable to define a quantity τ_P^* which takes into account the flux of returning particles Φ_{ret}

$$\tau_P^* = \frac{N}{\Phi_{in} - \Phi_{ret} - dN/dt} \tag{2.6}$$

This number is of particular importance when the removal of the helium ash from a burning plasma is considered: the dilution and additional radiative losses by the helium lead to a more stringent criterion for sustained burn. As pointed out in [Reiter et al., 1990], this leads to the condition

$$\frac{\tau_{P,\alpha}^*}{\tau_E} \leq 14 \tag{2.7}$$

for the confinement time of the α-particles. First measurements of this quantity on the DIII-D tokamak seem to indicate that the necessary value can be reached in the ELMy H-mode [Hillis et al., 1994].

In addition, it was found in ASDEX that the confinement of angular momentum increases in the H-mode: Generally, the momentum confinement time τ_M, i.e. the value of angular momentum stored in the plasma at a given torque, e.g. due to neutral beam heating, increases together with τ_E in regimes of improved confinement [Kallenbach et al., 1991]. It was found that the radial distribution of angular momentum, i.e. the profile of the toroidal rotation induced by neutral beams is broader in the H-mode than in the L-mode. Thus, similar to the transport of energy and particles, an anomalous transport mechanism seems to determine the plasma viscosity.

More insight into the transport properties of the H-mode can be gained if one moves from the global confinement analysis to local analysis, i.e. the description of radial profiles of density and temperature, $n(r)$ and $T(r)$. This analysis has been done in great detail in various tokamaks. Fig. 2.4 shows an example from the DIII-D tokamak [Groebner, 1993].

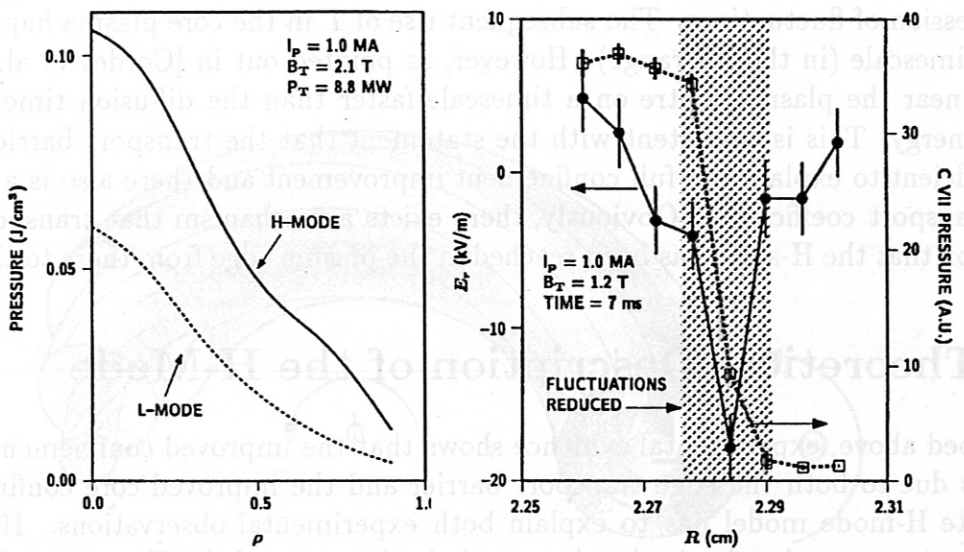

Figure 2.4: *Typical pressure profiles in the L- and the H-mode. In addition, a typical profile of the radial electric field in the edge is shown for the H-mode case.*

The change in the pressure profile cannot be described by a constant factor; in addition to the general increase, the shape of the profile changes. The most pronounced change occurs in the edge. It can be described by the appearance of an edge transport barrier of a typical width of 1-3 cm inside the separatrix [Wagner et al., 1984]. In order to model the profiles, the particle diffusivity D and the heat conductivity χ have to be reduced by a factor of 5-10 with respect to their L-mode values within the transport barrier. In addition, the electron heat conductivity χ_e has to be reduced by a factor of about in the core plasma to match the experimentally measured profiles.

Together with the improvement of confinement, it is observed that the levels of fluctuations in density, magnetic field and electrostatic potential in the edge are reduced. These results imply that in the edge transport barrier, at least some of the fluctuations responsible for anomalous transport are suppressed. On the DIII-D tokamak it was found that, together with the appearance of the transport barrier, a narrow layer of highly sheared poloidal rotation exists. As will be described in detail in the next section, this corresponds to a zone where the radial component of the electric field, E_r, exhibits a strong radial variation. Fig. 2.4 shows a typical E_r-profile together with a pressure profile of an impurity ion (C^{6+}). It can be seen that the zone of strong radial variation of E_r corresponds to the zone where a high pressure gradient is sustained. In addition, the zone in which the density fluctuations are reduced also coincides with this region (dotted

region in Fig. 2.4). The location of the separatrix is estimated to be within the dotted region, too.

The timescale of the initial appearance of the edge transport barrier is fast: Fluctuations are reduced on a timescale of ≤ 100 μs. With spectroscopic techniques, it is at the moment not possible to decide if the change in E_r happens comparably fast or even precedes the suppression of fluctuations. The subsequent rise of T in the core plasma happens on a slower timescale (in the ms range). However, as pointed out in [Cordey et al., 1994], it is seen near the plasma centre on a timescale faster than the diffusion time of particles or energy. This is consistent with the statement that the transport barrier alone is not sufficient to explain the full confinement improvement and there also is a change in core transport coefficients. Obviously, there exists a mechanism that transports the information that the H-state has been reached in the plasma edge from there to the core.

2.2 Theoretical Description of the H-Mode

As described above, experimental evidence shows that the improved confinement in the H-mode is due to both the edge transport barrier and the improved core confinement. A complete H-mode model has to explain both experimental observations. However, as the edge transport barrier is the characteristic signature of the H-mode and is also best documented, today's H-mode theories mainly describe the physics of this region. In addition, if one is mainly interested in the power threshold, the subsequent improvement of core confinement is not the key physics mechanism to be understood. In the following, we will therefore consider only the edge transport barrier. Tentative explanations of improved core confinement by a decoupling of radially overlapping modes are e.g. discussed in [Cordey et al., 1994].

Models for the build-up of the edge transport barrier involve a combination of two physical processes:

- The fast ($\approx 100\mu$s) build-up of the narrow layer with high sheared poloidal rotation.
- The decrease of fluctuations and therefore reduction of anomalous transport in this region

We will discuss these two processes separately and then present their combination as a model for the H-mode edge transport barrier. The discussion of the poloidal rotation requires knowledge of transport theory in a torus; for the reader not familiar to the subject, this so-called neoclassical theory is reviewed in Appendix B.

2.2.1 Sheared Poloidal Rotation and Radial Electric Field

It was shown above that in the experiments, a sheared poloidal rotation of impurity ions is found. We will now show that this is equivalent to a strong radial variation of the

electric field E_r. We start from the steady state ($d/dt = 0$) MHD force balance equation for an ion species i

$$\nabla p_i = Zen_i(\vec{E} + \vec{v}_i \times \vec{B}) \tag{2.8}$$

where p_i is the ion pressure.

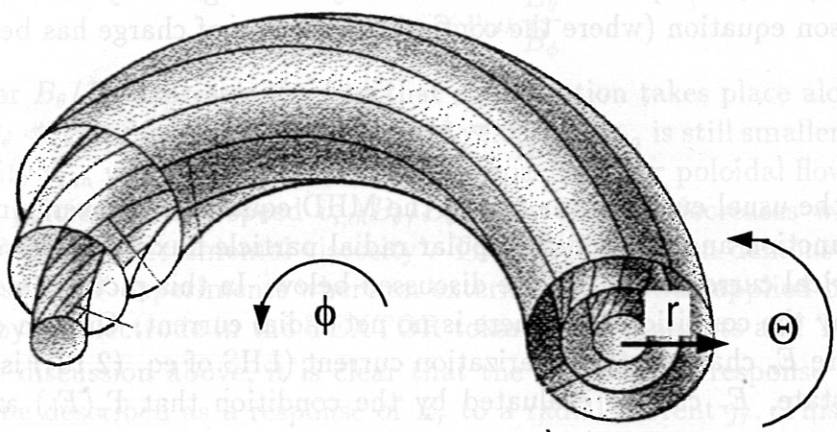

Figure 2.5: *Torus coordinates used for the evaluation of the flow velocity and electric field.*

This is evaluated in a toroidal co-ordinate system as shown in Fig. 2.5, where r is the direction of the plasma minor radius, θ the poloidal angle and ϕ the toroidal angle. Note that in other parts of the text, where no co-ordinates are specified, the toroidal field, $\vec{B}_\phi = (\vec{B} \cdot \vec{e}_\phi)\vec{e}_\phi$ is denoted by B_t. An equation for $\vec{v}_\perp$, the velocity perpendicular to $\vec{B}$, is obtained by the vector product of (2.8) with $\vec{B}$:

$$\vec{v}_{i\perp} = \frac{1}{Zen_iB^2}\nabla p_i \times \vec{B} - \frac{\vec{E} \times \vec{B}}{B^2} \tag{2.9}$$

Its contribution to the poloidal flow velocity is found by projecting $\vec{v}_{i\perp}$ onto $\vec{B}_\theta$:

$$v_{i\perp\theta} = \vec{v}_{i\perp} \cdot \frac{\vec{B}_\theta}{B_\theta} = \frac{\nabla_r p_i}{Zen_i}\frac{B_\phi}{B^2} - E_r\frac{B_\phi}{B^2} \approx \frac{\nabla_r p_i}{Zen_iB} - \frac{E_r}{B} \tag{2.10}$$

where we have used $B_\phi \gg B_\theta$. The contribution of parallel flow to the poloidal flow is given by

$$v_{i\|\theta} = v_{i\|\phi}\frac{B_\theta}{B_\phi} \approx v_{i\|\phi}\frac{B_\theta}{B} \tag{2.11}$$

We obtain the following expression for the poloidal flow velocity

$$v_{i\theta} = v_{i\|\phi}\frac{B_\theta}{B} + \frac{\nabla_r p_i}{Zen_iB} - \frac{E_r}{B} \tag{2.12}$$

Thus, a measured change in v_θ without dramatic changes in v_ϕ and ∇p is directly related to a change in E_r. This allows us to discuss H-mode physics in two different pictures:

- Change of E_r: The temporal evolution of the system is given by the r-component of the Poisson equation (where the continuity equation of charge has been used):

$$\epsilon\epsilon_0\frac{dE_r}{dt} = j_r + e(\Gamma_i - \Gamma_e) \tag{2.13}$$

  where j is the usual current obtained in the MHD equations by averaging the distribution function and the non-ambipolar radial particle fluxes Γ represent higher order electrical currents and will be discussed below. In this picture, steady state is defined by the condition that there is no net radial current. Only in dynamical phases where E_r changes, the polarization current (LHS of eq. (2.13)) is non-zero. In steady state, E_r can be evaluated by the condition that $\Gamma_e(E_r)$ and $\Gamma_i(E_r)$ cancel.

- Change of v_θ: The temporal evolution of the system is given by the θ component of the force balance equation

$$n_i m_i\frac{dv_{i\theta}}{dt} = j_r B_\phi + \sum F_\theta \tag{2.14}$$

  where the forces F_θ are due to the torque that results from the non-ambipolar fluxes Γ across the toroidal field. In this picture, steady state is determined by the condition that the sum of all torques cancels. The poloidal velocity is determined by this condition via the different parameter dependencies $F_\theta(v_\theta)$

It can be seen that the two approaches are equivalent: eq. (2.14) results when (2.13) is crossed with B_ϕ. Depending on the exact approach used, there may be further terms that appear in the equations determining the temporal evolution (e.g. shear viscosity in the poloidal momentum balance).

In a torus, the calculation of transport coefficients and also the viscosity of the plasma differs appreciably from the results obtained for a straight cylinder. This is the subject of neoclassical transport theory. A short summary of of the basic effects occuring in neoclassical theory is given in the appendix B. Neoclassical theory predicts a strong damping of poloidal rotation due to the so-called magnetic pumping: a fluid element that moves to the inner (high field) side is compressed due to the compression of magnetic field lines. On the way back to the low field side, the fluid element again expands. Due to the effect of collisions, this process is generally non-adiabatic, i.e. there is dissipation

of energy and thus a damping force. A detailed discussion of the effect can be found in [Shaing and Crume, 1989]. One effect of collisions is the equilibration of the distribution function along field lines. Thus, if the fluid element completes one poloidal turn in a time less than the equivalent equilibration time along field lines, the damping of poloidal flow decreases with a further increase in v_θ. As the equilibration time along the field lines happens on the timescale of the sound speed, it is linked to the ion thermal velocity, $v_{i,th} = \sqrt{2kT_i/m_i}$. Thus, the viscous force due to magnetic pumping has a maximum for

$$v_{i\theta} \approx v_{i,th}\frac{B_\theta}{B_\phi} \tag{2.15}$$

The factor B_θ/B_ϕ expresses the fact that equilibration takes place along the field lines. Due to $B_\theta \ll B_\phi$, this means that the fluid velocity v_{theta} is still smaller than the thermal ion velocity $v_{i,th}$ when condition (2.15) is approached. For poloidal flow velocities higher than the poloidal sound speed $v_{i,th}B_\theta/B_\phi$, the viscosity decreases with $v_{i\theta}$; this is an effective 'negative incremental viscosity'. The effect has been demonstrated experimentally by 'spin-up' experiments where an external torque was applied by a radial current induced by an electrode in the TEXTOR tokamak [Weynandts and Taylor, 1990].

From the discussion above, it is clear that the neoclassical response of $v_{i\theta}$ to a torque can also be described as a response of E_r to a radial current j_r. This has been treated in detail by Stringer [Stringer, 1993]. We will summarize the results of his discussion.

Without additional non-ambipolar loss mechanism, the neoclassical value of E_r is determined by the radial flow of ions out of the plasma (in neoclassical theory, this is higher than the radial flow of electrons by $\sqrt{m_i/m_e}$ in the case of vanishing radial electric field). E_r adjusts to a value for which the net flow out of the plasma is zero (electrons are accelerated and ions are decelerated). This so-called *ambipolar* radial electric field is given by

$$E_a = \frac{T_i}{e}\left(\frac{n'}{n} + \gamma_i\frac{T_i'}{T_i}\right) + B_\theta v_{i\|} \tag{2.16}$$

It should be noted that this is the ambipolar field resulting from neoclassical theory without other non-ambipolar losses. In the following, we will use the name E_a for this expression, although in the presence of other radial currents, the value of the ambipolar field, i.e. that required to maintain net zero-current, may differ from E_a.

This result can be extended to an expression in the presence of an arbitrary radial electric field. The expression for the radial current is then given by

$$j_r = \frac{\sqrt{\pi}nT_i\epsilon^2}{Br}\frac{1}{v_{i,th}B_\theta}(E_r - E_a)e^{-(\frac{E_r}{v_{i,th}B_\theta})^2} \tag{2.17}$$

The radial current first increases with electric field, then decreases when E_r becomes comparable to the $v_{i,th}B_\theta$. This is the equivalent to the negative incremental viscosity mentioned above. In the picture of radial current and electric field, this is a 'negative incremental resistivity'.

The expression above is valid in the plateau regime [Galeev and Sagdeev, 1968] when the mean free path of a particle is comparable to the connection length. In [Stringer, 1993], the smooth transition from the plateau to the collision dominated regime is discussed. If the mean free path becomes much shorter than the connection length, the analysis gives

$$j_r = nT_i\epsilon^2\nu_{ii}\frac{E_r - E_a}{E_r^2 + (r\nu_{ii}B)^2} \tag{2.18}$$

where ν_{ii} is the ion-ion collision frequency defined in Appendix B (Eqn. B.4). Again, the function has a maximum around $E_r \approx v_{i,th}B_\theta$, although the exact value is higher than in the plateau regime.

For any non-ambipolar loss-mechanism, there will be a neoclassical current to maintain the net-zero current condition. This condition then determines the radial electric field. Different authors propose different loss-mechanisms as e.g. non-ambipolar electron loss due to stochasticity or anomalous transport [Itoh and Itoh, 1989], Reynold's stress [Diamond and Kim, 1991] or ion orbit loss [Shaing and Crume, 1989]. The latter is due to the loss of banana trapped ions which intersect a limiting structure of the plasma. Due to the wider banana width of the ions ($\propto \rho_i/\rho_e \propto \sqrt{m_i/m_e}$, see Eqn. B.8), this loss mechanism provides a source for an ion current from the plasma edge with a width of the order of the poloidal gyroradius.

The example of ion orbit loss can be used to illustrate how a multivalued dependence of E_r on the plasma parameters may occur. Fig. 2.6 shows the dependence of the ion orbit loss current j_L and the neoclassical return current j_{NC} on E_r.

As pointed out above, the steady state solution is given when no net current flows out of the plasma, i.e. $j_L = j_{NC}$. The solution to this equation is the intersection point of the two curves. It can be seen that, depending on the collisionality, one or three solutions may exist. At high collisionality, only a solution with low E_r (i.e. $E_r \ll v_{i,th}B_\theta$) exists. As the collisionality is decreased, three solutions occur. It can be shown that the middle point is unstable, i.e. it is not a solution for E_r. Thus, there are two possible solutions, one with high E_r and one with low E_r. At still lower collisionality only one solution with high E_r exists. Thus, a decrease in collisonality (i.e. heating the plasma) will lead to an abrupt transition from low E_r to high E_r. We will return to the dynamic behaviour of this system in the next chapter.

The mechanism of ion orbit loss may thus explain the spontaneous spin-up of the plasma at the L-H threshold. As e.g. discussed in [Itoh et al., 1991], the jump in E_r may happen on a fast timescale: in the picture of E_r and j_r, it is the time it takes to charge up the plasma edge. This 'capacitive' timescale is of the order of $\leq 100\mu$s, consistent with the experimental evidence. Note that the radial variation of the loss will also lead to a radial variation of E_r, as is observed in the experiment. However, the actual extension of the zone where E_r substantailly varies may be determined by other factors as e.g. shear viscosity.

In the picture of torque and rotation, the ion orbit loss is a radial current providing a torque to the plasma. This torque is damped by the above mentioned magnetic pumping.

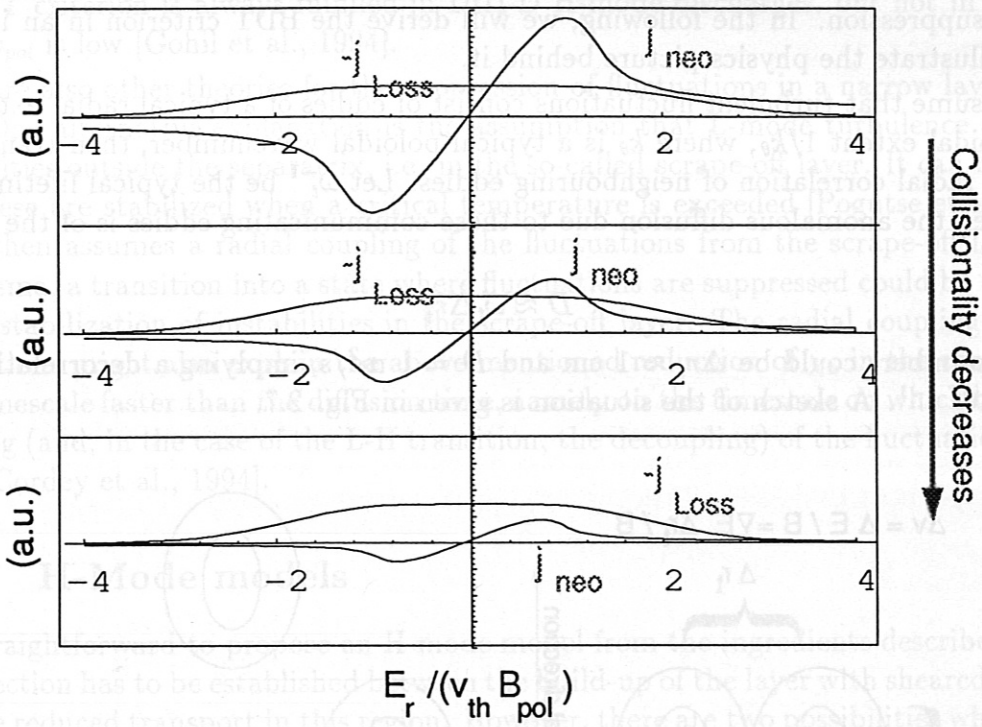

Figure 2.6: *Dependence of ion orbit loss current and neoclassical return current on the radial electric field. The intersection points provide possible current free solutions. As collisionality is decreased, a multivalued solution for E_r occurs.*

As the torque is increased and v_θ exceeds the poloidal ion sound speed, the viscosity decreases and a high value of v_θ is established. Although no net charge transport takes place, a transfer of energy and momentum happens because the ion orbit loss works on the highly energetic tail of the distribution function whereas the magnetic pumping mainly comes from low energy particles.

Another possibility to drive poloidal rotation is the ion pressure gradient itself. In the DIII-D tokamak, it was shown that in a fully developed H-mode, the measured poloidal rotation can be explained by ∇p_i if the orbit squeezing effect, i.e. the change of the particle orbits due to the presence of the strongly varying radial electric field, is taken into account [Hinton et al., 1994]. Thus, once the H-mode is developed, the observed poloidal rotation may mostly be due to the steep pressure gradients.

2.2.2 Suppression of Fluctuations

As mentioned above, anomalous transport is thought to be due to turbulent fluctuations developing in the plasma. Biglari et al. have given an explanation how sheared rotation can decorrelate fluctuations and thereby reduce transport [Biglari et al., 1990]. Their

analysis gives the so-called Biglari-Diamond-Terry (BDT) criterion for an effective turbulence suppression. In the following, we will derive the BDT criterion in an intuitive way to illustrate the physics picture behind it.

If we asssume that turbulent fluctuations consist of eddies of a typical radial extent Δr_t and poloidal extent $1/k_\theta$, where k_θ is a typical poloidal wavenumber, then transport is due to a radial correlation of neighbouring eddies. Let ω_t^{-1} be the typical lifetime of an eddy, then the anomalous diffusion due to these communicating eddies is of the order

$$D \approx \omega_t \Delta r_t^2 \tag{2.19}$$

Typical numbers could be $\Delta r_t \approx 1$ cm and $D = 1$ m^2/s, implying a decorrelation rate of $\omega_t = 10^4$ s^{-1}. A sketch of the situation is given in Fig. 2.7.

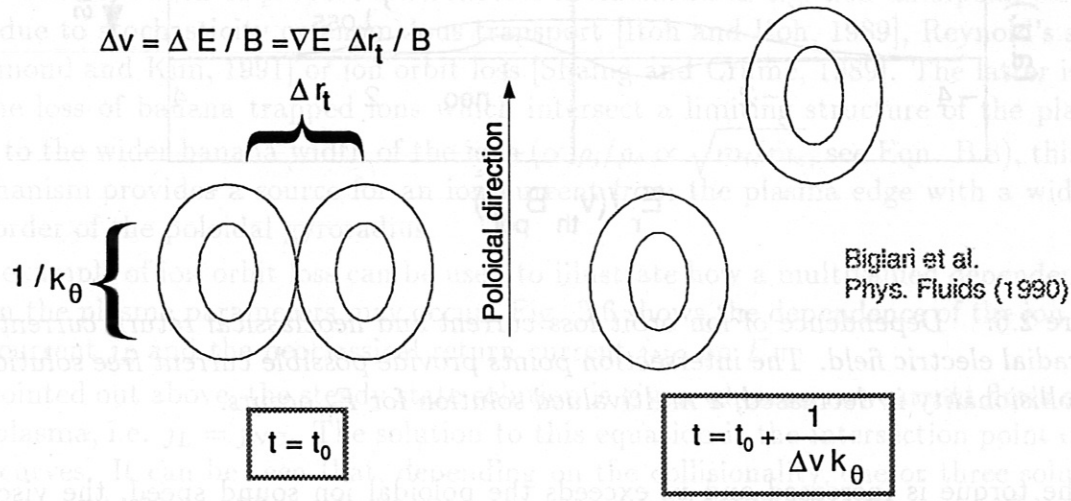

Figure 2.7: *Model for the the decorrelation of turbulent eddies by sheared poloidal rotation.*

If we now introduce the sheared poloidal rotation, the difference in v_{pol} between neighbouring eddies is $\Delta v_{pol} = \Delta E_r/B$, or, in linearized form $\Delta v_{pol} = (dE_r/dr)(\Delta r_t/B)$. The time it takes to separate two neighbouring eddies by their poloidal extent is $1/(\Delta v_{pol} k_\theta)$. If this time is shorter than the typical eddy lifetime, the radial correlation between neighbouring eddies is effectively suppressed by sheared rotation. This leads to the BDT criterion for the suppression of transport due to turbulent fluctuations

$$|\frac{dE_r/dr}{B}| > \frac{\omega_t}{\Delta r_t k_\theta} \tag{2.20}$$

A more rigorous derivation can be found in [Biglari et al., 1990].

Using the numbers from above, we find that the gradient in v_{pol} has to exceed 10^5 s^{-1}. As was shown in the section above, this is fulfilled in DIII-D, where the v_{pol} varies by

more than 10^4 m/s on a radial extent of only few cm. A detailed analysis shows that the BDT criterion is always fulfilled in DIII-D H-mode discharges, but not in L-mode, where v_{pol} is low [Gohil et al., 1994].

There are also other theories for the suppression of fluctuations in a narrow layer at the edge. One alternative explanation is the assumption that L-mode turbulence is due to instabilities outside the separatrix, i.e. in the so-called scrape-off layer. It can be shown that these are stabilized when a critical temperature is exceeded [Pogutse et al., 1994]. If one then assumes a radial coupling of the fluctuations from the scrape-off layer into the plasma, a transition into a state where fluctuations are suppressed could be triggered by the stabilization of instabilities in the scrape-off layer. The radial coupling between fluctuations might also explain the above mentioned reduction of χ_e in the core plasma on a timescale faster than the diffusion time, namely on the timescale on which the radial coupling (and, in the case of the L-H transition, the decoupling) of the fluctuations takes place [Cordey et al., 1994].

2.2.3 H-Mode models

It is straightforward to propose an H-mode model from the ingredients described above: a connection has to be established between the build-up of the layer with sheared rotation and the reduced transport in this region. However, there are two possibilities which differ in the causality of the events involved:

One possibility is that an initial spin-up triggers the suppression of fluctuations: increased heating of the plasma leads to an increase in poloidal rotation as discussed in section 2.2.1. At a critical heating power, the plasma switches from the state with low poloidal rotation to the one with a high value. If this high value is sufficient to suppress turbulence, the edge transport barrier is formed and confinement improves. Note that, as mentioned above, this does not include a mechanism to explain improved core confinement. In this theory, the change in E_r should precede the suppression of fluctuations: it was mentioned above that the evolution of E_r from the L- to the H-state happens on a 'capacitive' timescale of $\leq 100\mu$s. If the reduction of fluctuations is due to E_r', it should set in once the BDT-criterion (2.20) is fulfilled. This happens during the change of E_r: as was shown in DIII-D, in L-mode, the BDT-criterion is not fulfilled, but in H-mode it is. Nevertheless, it cannot be resolved experimentally when precisely this happens. Thus, we can only conclude that the reduction of fluctuations should lag behind the initial change of E_r by a time interval $\leq 100\mu$s.

An ongoing discussion exists about the trigger mechanism for the spin-up, i.e. the source of non-ambipolar current that drives the neoclassical return current [Hugill, 1994]. As mentioned above, ion-orbit loss is a good candidate, but a quantitative measurement or calculation of the loss current has not yet been accomplished. This will remain a subject for further work. However, once the sheared rotation is established, ∇p_i may be the main cause for the poloidal rotation, i.e. only the initial spin-up has to be explained by the ion orbit loss effect.

A different approach uses an alternative scenario: the stabilization of instabilities in the scrape-off layer is assumed to be the initial event. This will lead to the build-up of a steep gradient in p_i and therefore drive poloidal rotation via the orbit squeezing effect mentioned above. In this approach, E_r is an effect and not the cause of the H-mode transition. Here, the change of E_r should occur together with the build-up of the edge pressure gradient. In the next chapter, it will be shown that this timescale is of the order of several 100 μs. Contrary to the scenario described above, there should *not* be a change in E_r before the fluctuations are reduced.

Although these alternative theories are very different in their interpretation of cause and effect, a fully quantitative check with the experiment has not yet been accomplished. This is mainly due to the experimental difficulties in measuring the fast jump of E_r but also the theoretical background for describing the anomalous loss processes that have to be suppressed at the L-H transition is not yet sufficient. It remains a further challenge to the experiment to decide which mechanism is dominant.

Another critical point is the explanation of the parameter dependence of the power threshold of the L-H transition (see Eqn. (2.1)). It can be shown [de Blank and Zohm, 1994] that the models based on the spin-up induced by ion orbit loss yield a nearly linear dependence of P_{thr}^{LH} on $n(a)$ and therefore, under the assumption of similar profile shapes $n(r)$ in the L-mode, are in agreement with the experimentally observed $\bar{n}_e$ scaling. The experimental evidence for the scaling $P_{thr}^{LH} \sim B_t$ has not yet been adequately described. However, the obvious contradiction that ion orbit loss should depend on the banana width and therefore scale with B_θ rather than with B_t has been discussed by Shaing [Shaing, 1992] who finds that the orbit squeezing effect causes the orbit loss width to be independent of B_θ.Another experimental observation to be explained is the difference of P_{thr}^{LH} when the ion ∇B drift is reversed. A calculation of the drift surfaces from which loss occurs was given in [Hinton and Chu, 1985]. From this it follows that the lost ions have to travel different distances in order to reach the target plates. This effect might reduce the ion orbit loss current for the unfavorable direction due to the enhanced scattering probability and could therefore be responsible for the higher threshold [De Blank, 1995]. However, a complete description of the scaling of P_{thr}^{LH} has not yet been given.

Chapter 3

Dynamic Behaviour of the L-H Transition

We now turn to a time-dependent description of the L-H transition. First, we will describe the experimental characteristics; then, we interpret them using a time-dependent model based on the theoretical ideas discussed in chapter 2. The discussion follows the analysis published in [Zohm et al., 1994a] and [Zohm et al., 1995b].

3.1 The Dithering Cycle

As described in the previous chapter, the L-H transition occurs when the heating power P exceeds a given threshold P_{thr}^{LH}. In various tokamaks, during a gradual increase of the heating power, a sequence of L-H-L transitions is observed for $P \approx P_{thr}^{LH}$ prior to the final transition into the H-mode. The sequence of transitions is known as 'dithering H-mode'. In the following, we will experimentally characterize this phase on the ASDEX Upgrade tokamak. A detailed description of ASDEX Upgrade is given in Appendix A.

The number of dithering cycles that occur before the final L-H transition depends on the rate at which the heating power P is increased past P_{thr}^{LH}. Fig. 3.1 shows two examples from ASDEX Upgrade, in which the dithering cycles can be seen as a modulation of the D_α signal in the divertor. Both discharges are in the lower single-null configuration with the ion ∇B drift towards the X-point (i.e. 'favorable drift direction') and Deuterium as the working gas. In the first case ($B_t = -2$ T, $I_p = 1.2$ MA, $\bar{n}_e = 5 \times 10^{19}$ m^{-3}, $P_{thr}^{LH} \approx 2$ MW), NBI heating of 5 MW is applied in a step function (upper traces of Fig. 3.1). The absorption of power in the plasma is governed by the slowing down time of the fast ions which is typically of the order of 10-20 ms. The heat flux from the core plasma through the edge increases on the (longer) timescale of the global energy confinement time τ_E. In order to compare different cases, we therefore characterize them by the normalized rise of power in excess to the threshold divided by the rise time or, if longer, by τ_E, i.e.

$$\gamma_P = \frac{1}{P_{thr}^{LH}} \frac{d}{dt}(P - P_{thr}^{LH}) \approx \frac{1}{\tau_E P_{thr}^{LH}}(P - P_{thr}^{LH}) \tag{3.1}$$

For this case, $\tau_E \approx 120$ ms and we have $\gamma_P \approx (50 \text{ ms})^{-1}$. With this fast ramp rate, few cycles appear. The opposite case is the ICRH heated discharge ($B_t = -2$ T, $I_p = 0.6$ MA, $\bar{n}_e = 3 \times 10^{19}$ m^{-3}, $P_{thr}^{LH} \approx 1.2$ MW, D(H) minority heating) shown in Fig. 3.1. Here $\gamma_P \approx (1 \text{ s})^{-1}$ and dithering cycles are seen for 100 ms (lower traces of Fig. 3.1).

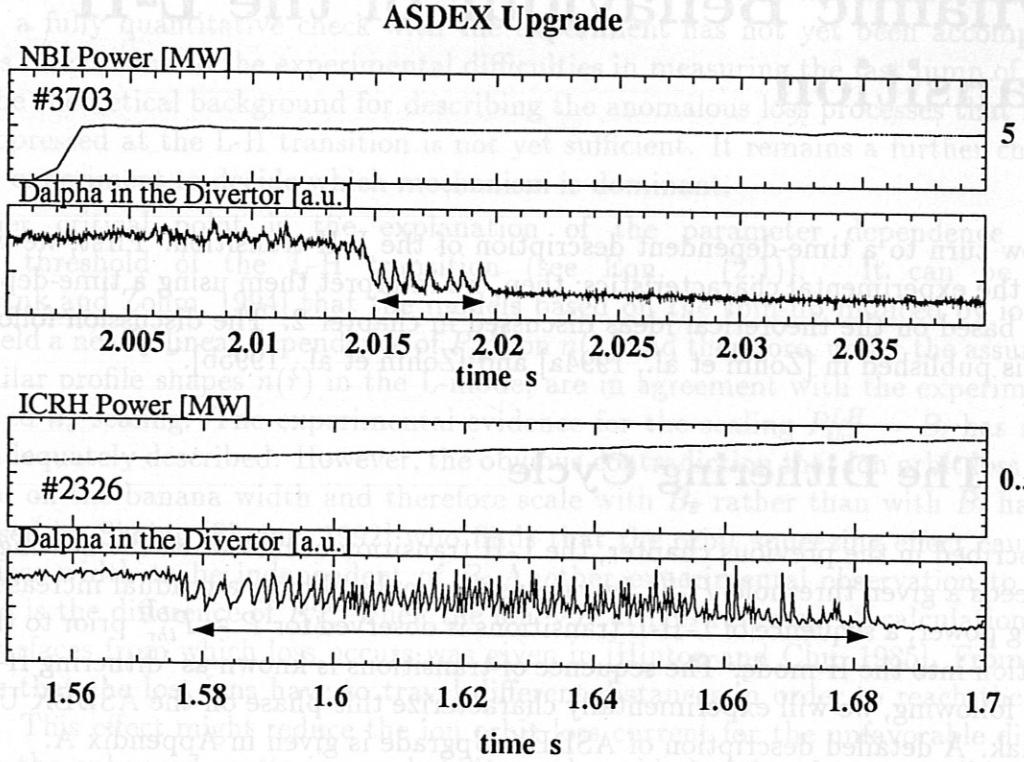

Figure 3.1: *L-H transitions with different rise rates of the heating power: $\gamma_P \approx (50 \text{ ms})^{-1}$ and $\gamma_P \approx (1 \text{ s})^{-1}$. The dithering phases are indicated by the arrows. Note the different time scales of the figures!*

In the limit of $\gamma_P \to 0$, which eventually occurs in ohmic H-mode discharges [Ryter et al., 1993], a series of dithering cycles of very regular frequency ($\approx 1 - 2$ kHz in ASDEX Upgrade at I_p=0.8 MA, B_t=-1.35 T) appears for the whole H-phase of 2-3 s (i.e. $\approx$ 6000 cycles!). Long dithering phases (up to 100 ms) at heating power close to P_{thr}^{LH} have also occurred using NBI, but the stationary dithering H-mode was only seen during OH-heating. The dithering cycles are sometimes also referred to as 'grassy ELMs', but, as has been shown on ASDEX [Zohm et al., 1992], do not show the typical MHD signatures of type III ELMs (which also appear close to P_{thr}^{LH}). In the dithering phase, confinement only marginally improves ($\approx$ 10% above L-mode); this also is a re-

markable difference to ELMy discharges which typically show an improvement of 1.5-1.8 with respect to L-mode. Type III ELMs are described in detail in the next chapter.

We have shown that the number of dithering cycles to appear depends on the ramp rate of the heating power in excess of P_{thr}^{LH}. The frequency of the cycles, however, shows only a weak variation with plasma parameters or heating power and is roughly constant at 1-2 kHz. Only for discharges with long dithering phases and a slow evolution towards the final H-mode transition, one can observe the frequency to vary by a factor of ≈ 2. This can be seen in the D_α trace of discharge 2326 in Fig. 3.1. Note that during the temporal evolution, also the shape of the D_α signal varies. We will later give an interpretation of this phenomenon.

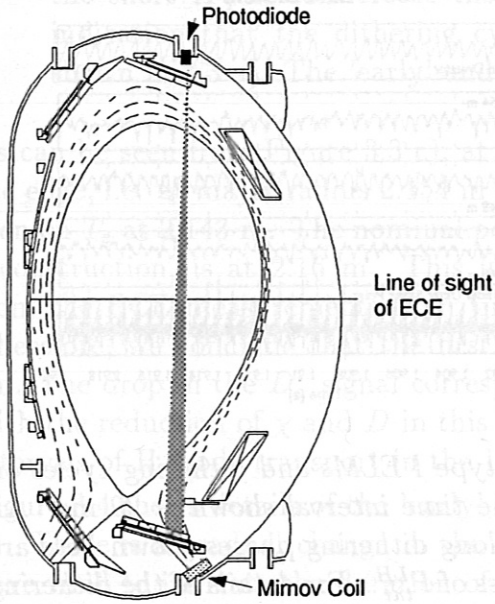

Figure 3.2: *Poloidal cross-section of the ASDEX Upgrade tokamak with the locations of the diagnostics mentioned in the text. The separatrix indicated in the figure is typical for the ASDEX Upgrade standard single-null configuration.*

To take a closer look at the dithering cycles, we follow the temporal evolution of the edge electron temperature by a fast (sample rate 50 kHz) Electron Cyclotron Emission (ECE) imicrowave spectroscopy system. Other diagnostics used are photodiodes observing D_α emission in the divertor region (sample rate 50 kHz) and a Mirnov coil measuring the fluctuating magnetic field under the separatrix strike point on the outer target plate (digitized at 500 kHz). The results presented here were obtained in the ASDEX Upgrade standard configuration (lower single null, $R_0 = 1.65$ m, $a = 0.5$ m, $\kappa = 1.7$) at a plasma current of $I_p = 0.8$ MA and different toroidal fields (see below). Figure 3.2 shows the plasma configuration and the locations of the diagnostics mentioned above.

We will now focus on the effect of dithering cycles on T_e. For this purpose, it is necessary to have a clear distinction between the dithering cycles and other burst-like phenomena. Figure 3.3 shows the differences between L-mode fluctuations, type I ELMs and dithering cycles. Type I ELMs are described in detail in the next chapter.

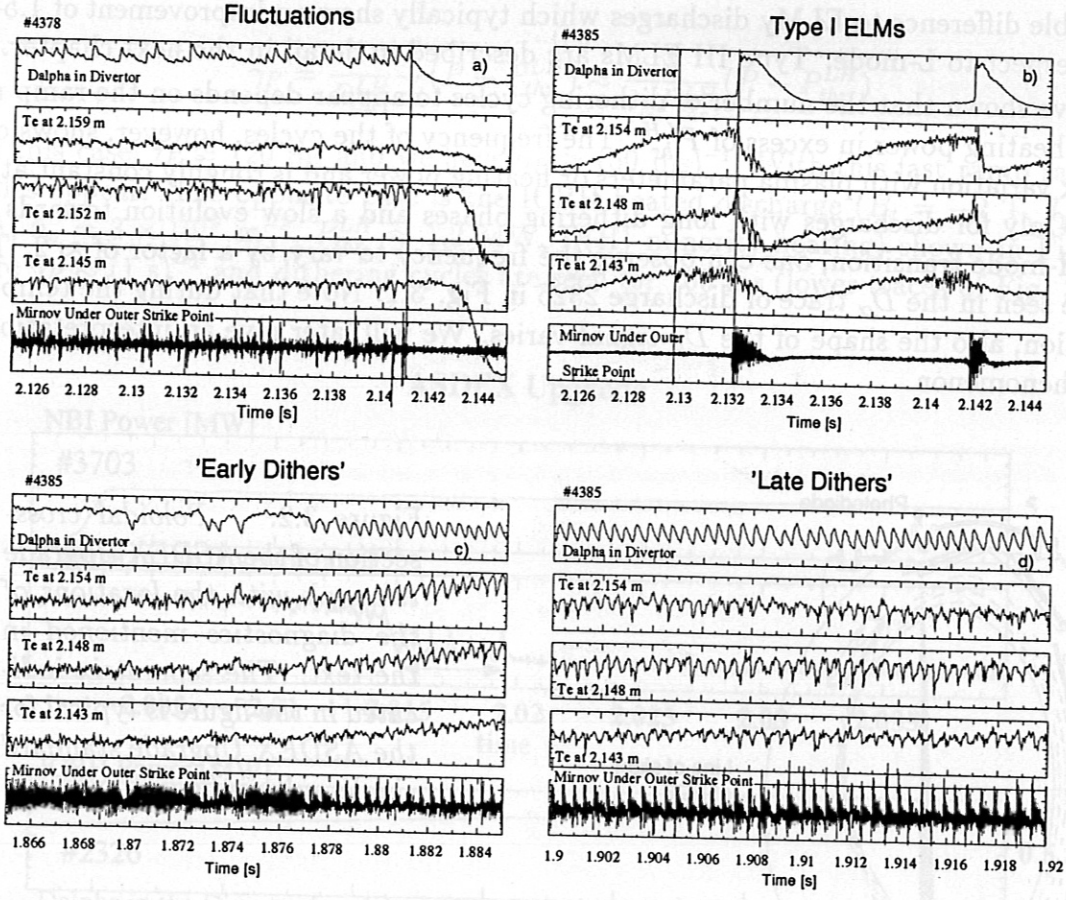

Figure 3.3: *The effect of L-mode fluctuations, type I ELMs and dithering cycles on D_α, T_e and $\dot{B}_\theta$ under the outer strike point. The time interval shown is 20 ms. All signals are [a.u.], T_e has a suppressed zero. The long dithering phases shown here are obtained by a slow ramp of heating power in excess of P_{thr}^{LH}. For details of the dithering phases, see next figure. The general behaviour of the discharges can be seen in Figure 4 and 5, where # 4378 is shown; # 4385 is similar to # 4387 shown in Figure 4 and 5.*

We can distinguish the following events:

- L-mode fluctuations (Figure 3.3 a)): at high heating power in the L-mode, fluctuations may appear as bursts on the D_α signal. They do not show a regular frequency. They are correlated with sharp negative going spikes on the T_e signal from the edge, and small turbulent bursts of magnetic fluctuations. At the L-H transition (vertical line in Figure 3.3 a)), the fluctuations are suppressed. Note that at the end of the time interval shown here, the ECE signal is cut-off due to the increase in density in the H-mode. In a fluctuating phase as shown here, τ_E is at L-mode level.
- Type I ELMs (Figure 3.3 b)): type I ELMs appear as distinct events on the D_α signal with an amplitude much higher than that of dithers or fluctuations. T_e

drops by a considerable amount during the ELM and then builds up again. No magnetic precursor oscillation is observed, but the broadband fluctuation level of T_e increases prior to the type I ELM (in the phase indicated by the vertical lines in Figure 3.3 b)). The turbulent MHD activity during a type I ELM has a higher amplitude than during the other events.

- Dithering cycles (Figure 3.3 c) + d)): dithering cycles appear as a regular oscillation on the D_α emission and also on T_e at the edge. The period of high D_α level is associated with a high turbulent fluctuation level of B_θ corresponding to L-mode values. This leads us to the statement that dithering cycles are mainly a series of H-L-H transitions and not MHD events per se. Normally, there is a gradual increase of T_e and consequently τ_E during a longer series of dithering cycles indicating that the short H-phases increase the energy content of the plasma. This is another indication that the dithering cycles are different from the L-mode fluctuations shown in 3.3 a). The 'early' and 'late' phases are described in detail below.

As can be seen from Figure 3.3 c), at the L-H transition, D_α drops and T_e increases at the edge, i.e. at major radius 2.154 m and 2.148 m. For the first cycles, no correlation is seen on T_e at 2.143 m. The nominal position of the separatrix, derived from equilibrium reconstruction, is at 2.16 m. This is consistent with the separatrix position derived from the ECE measurements from time traces during ELMs themselves within 1 cm. Therefore, we conclude that the first cycles affect only a narrow region of $\Delta R \approx 1.5$ cm. The drop in the D_α signal corresponds to an increase in T_e at the edge, consistent with the reduction of χ and D in this region. Thus, the dithering cycles appear as brief intervals of H-mode transport in the L-mode profile.

Figure 3.4 shows details of the 'early' and 'late' phase indicated in Figure 3.3 c) and 3.3 d). There is a gradual change in the character of the cycles in time: in Figure 3.4, we have tried to indicate the duration of the L- and H-phases for the early and late phase as e.g. determined from the level of magnetic fluctuations. It can be seen that in the late phase, the system stays in the H-mode for a longer time than in the early phase. Thus, the early dithers appear as short H-phases on an L-mode profile whereas the late dithers are short L-phases on an H-mode profile. Also, in the late phase, the dithering cycles affect T_e at 2.143 m, indicating that the region of reduced transport may increase with time. This increase, however, is within our uncertainty of the separatrix position.

The frequency of the cycles is $\nu \approx 2$ kHz. Assuming that the change in the profiles is purely diffusive, we can estimate χ from the measurements: $\chi \approx \nu(\Delta R)^2$. Using $\Delta R = 1.5$ cm, a value of $\chi \approx 0.45$ m^2/s results. This is lower than typical L-mode values of χ in the edge of a tokamak of the size of ASDEX Upgrade at comparable additional heating power (e.g. $\chi_e \approx 5$ m^2/s in ASDEX at 3 MW [The ASDEX Team, 1989]). Thus, the timescale of the change of profiles is mainly given by the reduced H-mode coefficient (which gives the longer timescale). This can, in fact, be seen in Figure 3.3 c) and d), where the build-up of T_e in the H phase is slower than the decrease in the L-phase, leading to the asymmetric shape of the T_e signal. Note that the terms L- and H-mode are used

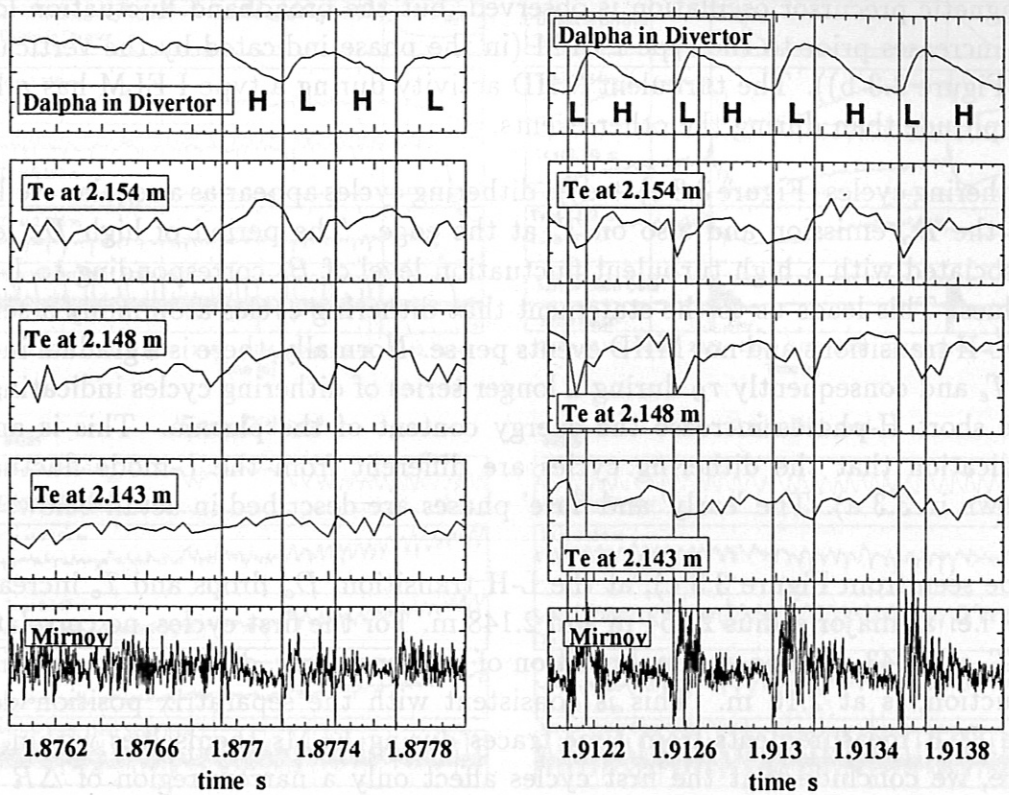

Figure 3.4: *'Early' (left) and 'Late' (right) dithers from Figure 3.3 c) and 3.3 d) with expanded time axis (time interval shown is 2 ms). In the late phase, the system stays in H-mode for a longer time than in the early phase.*

here to describe the change of edge transport coefficients and not a global improvement of confinement as is observed in a fully developed H-mode.

From this we conclude that during the dithering cycles, the edge transport barrier typical for the H-mode is established and destroyed for periods of $\approx 500\mu s$. Note that the actual timescale of the change in χ may be much shorter, as the $500\mu s$ timescale only determines the build-up and decrease of T_e in a narrow edge region of 1-2 cm. This will be discussed from a theoretical point of view in the next section.

As stated above, the number of dithering cycles occuring during the transition decreases with the normalized ramp rate γ_P of the power defined by Eqn. (3.1). This number can be varied by either changing the power increase or by varying P_{thr}^{LH}. The effect of a change in γ_P at fixed P_{thr}^{LH} (decrease of the number of dithers with increasing γ_P) has been described above. In the following, we examine the occurrence of dithering cycles at different values of P_{thr}^{LH}.

In ASDEX Upgrade, we have used three methods of varying P_{thr}^{LH} by a wide extent:

- Reversal of B_t: as in other tokamaks, the direction of the ion ∇B drift has a

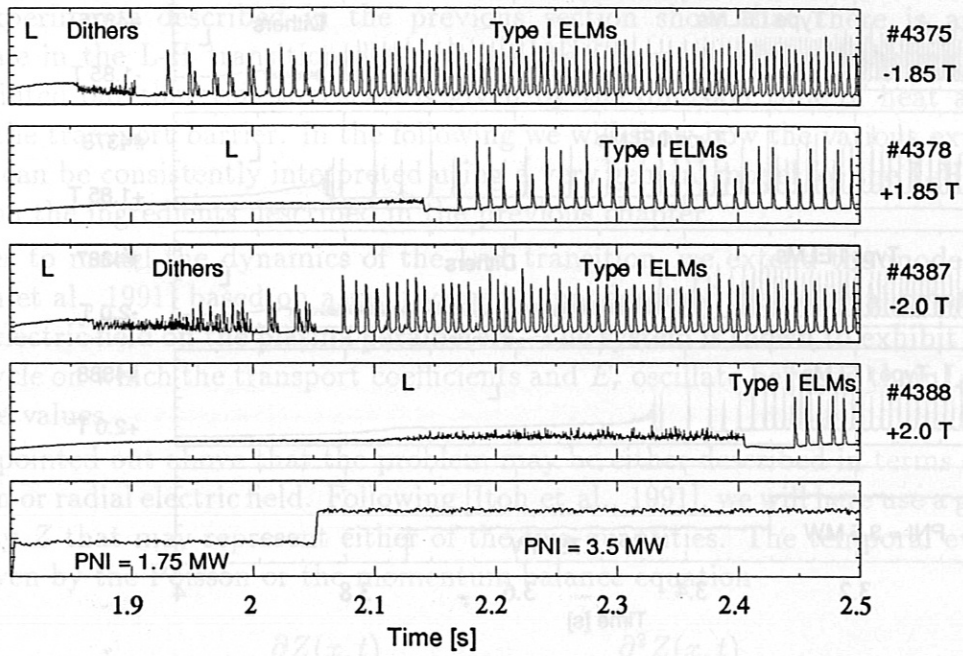

Figure 3.5: *Example for the variation in the occurrence of dithering cycles with varying P_{thr}^{LH} as seen in the D_α emission in the divertor.*

strong influence on P_{thr}^{LH} in case of a single-null X-point configuration: with the drift towards the X-point ('favorable direction') P_{thr}^{LH} is lower than for the other ('unfavorable') direction by a factor of ≈ 1.8 (see also Fig. 2.2). As shown in Figure 3.5, this introduces a new feature: with the unfavorable direction, dithering cycles do not occur. The L-H transition appears as a sharp event on the D_α trace. The high fluctuation level in the preceding L-phase can be distinguished from dithering cycles by the criteria mentioned above.

- Change of $|B_t|$: in various tokamaks, it was found that $P_{thr}^{LH} \propto B_t \bar{n}_e$ [H-mode Database Working Group, presented by O. Kardaun, 1992]. This is also true for ASDEX Upgrade (see Fig. 2.2). Therefore, variation of density and toroidal field allows to adjust P_{thr}^{LH}. In ASDEX Upgrade, we have varied B_t by a factor of 2 (1.35 T - 2.7 T) and found no qualitative changes in the occurrence of the cycles: for the favorable drift direction, the decrease of the number of cycles with an increase of γ_P holds for all values of P_{thr}^{LH} accessible in ASDEX Upgrade.
- Change of the working gas: with H-NBI into an H plasma, the threshold is nearly twice that of a D plasma heated by D beams. Values for He are somewhere in-between these two. Despite of this variation, there is no qualitative difference to the behaviour described above: cycles occur in cases with the favorable drift direction, but not with the unfavorable one and, again, their number depends on γ_P.

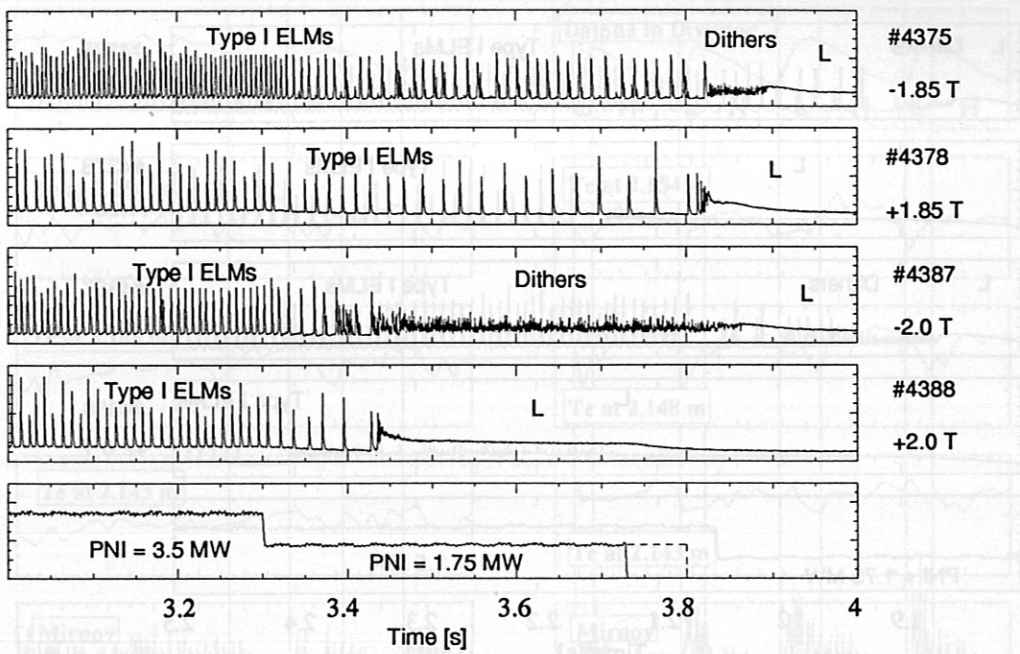

Figure 3.6: *Occurrence of dithering cyles at the H-L transition in the divertor D_α emission. NI power shown is for #4388, the dashed line indicates the timing of the other discharges.*

The effect of the change in P_{thr}^{LH} by changing $|B_t|$ and the reversal of the ion ∇B drift direction by changing sign(B_t) is documented in Figure 3.5 for cases with ± 1.85 T and ± 2 T. The other plasma parameters ($I_p = 0.8\text{MA}, \bar{n}_e = 0.5 \times 10^{20}\text{m}^{-3}$) and NBI timing and power are the same for all 4 discharges. A negative sign of B_t corresponds to the favorable direction, a positive sign to the unfavorable. For the pair with negative B_t, one can see the effect of γ_P, i.e. at the higher B_t, P_{thr}^{LH} is higher and γ_P smaller, resulting in more dithers to occur.

Dithering cycles have also been observed at the H-L back transition, i.e. in cases with $\gamma_P < 0$. The behaviour observed at the L-H transition can be compared with the occurrence of dithering cycles at the H-L transition. Due to the hysteresis, P_{thr}^{HL} is lower than P_{thr}^{LH}. In addition, the plasma drops out of an H-mode state, i.e. τ_E in Eqn. (3.1) is higher by a factor of ≈ 1.8 and therefore γ_P is lower. Figure 3.6 shows the H-L transition for the cases shown in Figure 3.5. It can be seen that in discharges with the favorable direction, the dithering phase is longer at the H-L transition than at the L-H transition in the same discharge. This can be explained by the decrease in γ_P. Nevertheless, even with the lower γ_P, no cycles are observed with unfavorable drift direction.

Therefore, the absence of dithering cycles with the unfavorable drift direction cannot be explained by a difference of γ_P. This is further confirmed by the observation that even for cases with the same threshold power, i.e. B_t = -2.7 T and B_t = +1.35 T at the same density, dithering cycles are observed only for the favorable direction.

3.2 Modelling the Dithering Cycle

The experiments described in the previous section show that there is an intrinsic timescale in the L-H transition determining the frequency of the dithering cycles. It was pointed out that this timescale is given by the diffusion time of heat and energy across the transport barrier. In the following we will show how the various experimental results can be consistently interpreted using a very general model for the L-H transition based on the ingredients described in the previous chapter.

In order to model the dynamics of the L-H transition, we extend the model proposed in [Itoh et al., 1991] based on a multivalued dependence of the poloidal rotation or the radial electric field on the plasma parameters. The system is shown to exhibit a so-called limit cycle on which the transport coefficients and E_r oscillate between their L-mode and H-mode values.

It was pointed out above that the problem may be either described in terms of poloidal rotation or radial electric field. Following [Itoh et al., 1991], we will here use a generalized quantity Z that may represent either of the two quantities. The temporal evolution of Z is given by the Poisson or the momentum balance equation

$$\frac{\partial Z(x,t)}{\partial t} = -N(Z,g) + \mu \frac{\partial^2 Z(x,t)}{\partial x^2} \tag{3.2}$$

where μ is the shear viscosity and $N(Z,g)$ is a source term that represents the current or torque due to the various non-ambipolar loss mechanisms. As described in the previous chapter, the balance of these losses determines the stationary value of Z. As has been discussed in the previous chapter, the timescale of Eqn. 3.2 is the capacitive timescale on which the plasma is charged up ($\leq 100\mu$s). This is always much faster than the transport timescale on which the edge gradients of T and n change. Thus, in the modelling described in this section, we always assume that the temporal derivative in Eqn. 3.2 can be neglected, i.e. the profile of Z adjusts to changes in N instantaneous and manages to keep the net radial current out of the plasma to zero. The coefficient μ is the shear viscosity that opposes a difference in rotation between flux surfaces. Due to this term, Z cannot arbitrarily vary between neighbouring flux surfaces. For $\mu = 1$ m^2/s (which is of the order of experimental values [Kallenbach et al., 1990]), the steady state profile $Z(x)$ is always a straight line although during the limit cycle, it may change appreciably.

Following [Itoh et al., 1991], we chose a simple nonlinear form for $N(Z,g)$ so that $Z(N)$ is multivalued:

$$N(Z,g) = g - g_1 + (\beta Z^3 - \alpha Z) \tag{3.3}$$

where the so-called gradient parameter g is given by [Itoh and Itoh, 1988]

$$g = const. \frac{1}{\rho_{p,i} \nu_i^*} \left(\frac{n'}{n} + \gamma \frac{T'}{T} \right) = g_0 \frac{T}{n} \left(\frac{n'}{n} + \gamma \frac{T'}{T} \right) \tag{3.4}$$

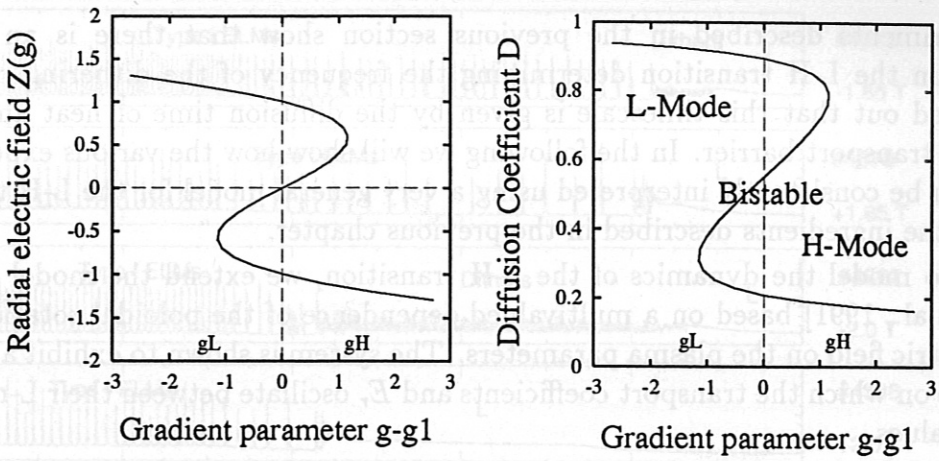

Figure 3.7: *Model curve $Z(g)$ and $D(g)$.*

The prime denotes the derivative with respect to x; g_0, g_1 and the Z-dependent term are chosen to analytically approximate the multivalued solution of poloidal rotation versus force or electric field against radial current in the presence of a nonambipolar radial flux. It can be thought to represent the graphic solution for Z obtained in the previous chapter (Fig. 2.6) for the ion orbit loss mechanism. In Fig. 2.6, the collisionality was varied as a parameter; following [Itoh et al., 1991], we have now expressed Z in terms of g in Eqn. (3.3) for a given radial current or poloidal rotation. A detailed discussion of the exact form of $N(z, g)$ in eq. (3.2) in the presence of various loss mechanisms was given in [de Blank and Zohm, 1994]. However, it will be shown that the simple modelling Eqn. (3.3) of the nonlinear dependence $N(Z)$ correctly describes the basic experimental observations.

As can be seen in Fig. 3.7 $Z(g)$ is single-valued for $g < g_L$ and $g > g_H$ whereas inbetween, three solutions of the cubic equation exist. Fig 3.7 shows a typical curve $Z(g)$.

In addition to the equation for Z, we have to solve the time dependent transport equations for particles and energy. The particle transport equation is derived from mass conservation

$$\frac{\partial n}{\partial t} = -\nabla \vec{\Gamma} + S \tag{3.5}$$

where n is the particle density, $\vec{\Gamma}$ the particle flux and S a source term representing local sources (e.g. ionization). Energy conservation reads

$$\frac{\partial}{\partial t}(\frac{3}{2}nT) = -\nabla \vec{q} + Q \tag{3.6}$$

where T is the temperature, $\vec{q}$ is the heat flux and Q represents a local energy source

(e.g. ICRH heating). We make the following ansatz for the fluxes

$$\vec{\Gamma} = -D\nabla n \tag{3.7}$$

$$\vec{q} = -n\chi\nabla T + \frac{3}{2}T\vec{\Gamma} \tag{3.8}$$

where D is the particle diffusivity, χ the heat conductivity and we have not considered explicit drift velocities. Under the assumption $S = Q = 0$, i.e. no sources in the volume considered, the variation of density and temperature is then (in one dimensional slab geometry) given by

$$\frac{\partial n}{\partial t} = \frac{\partial}{\partial x}\Big(D(Z)\frac{\partial n}{\partial x}\Big) \tag{3.9}$$

$$\frac{\partial T}{\partial t} = \frac{\partial}{\partial x}\Big(\frac{2}{3}\chi(Z)\frac{\partial T}{\partial x}\Big) + \frac{1}{n}\Big(\frac{2}{3}\chi + D\Big)\frac{\partial n}{\partial x}\frac{\partial T}{\partial x} \tag{3.10}$$

The transport properties of the H-mode are modelled by

$$D(Z) = \frac{1}{2}(D_{max} + D_{min}) + \frac{1}{2}(D_{max} - D_{min})\tanh Z \tag{3.11}$$

A similar equation is used for $\chi(Z)$. Here D_{max}, χ_{max} correspond to L-mode conditions and D_{min}, χ_{min} to the H-mode. A typical set we use is $D_{max} = 1$ m^2/s, $D_{min} = 0.1$ m^2/s and $\chi = 3D$. A model curve $D(g)$ is shown in Fig. 3.7.

Similar to [Itoh et al., 1991], we find that a transport barrier, i.e. a zone of radial extent Δ in which transport is reduced, develops in the H-mode. The width Δ is governed by μ and the parametrization of $N(Z)$, i.e. α and β in Eqn. (3.3). The difference to [Itoh et al., 1991] is that we include the temporal and spatial variation of the temperature. As will be shown below, this is a necessary ingredient to describe the experimental behaviour, i.e. the effect of the rise in heating power. We solve Eqns. (3.9), (3.10) and (3.2) simultaneously on a spatial domain extending over $\approx$ 2-3 poloidal ion gyroradii, i.e. from $x = 0$ at 2 cm inside the separatrix up to the separatrix. As has been shown [Itoh et al., 1991], the radial extension of the domain does not influence the width of the transport barrier. The boundary conditions are $\Gamma_{in} = const.$ and $q_{in} = const.$ at the left boundary (representing the fluxes from the plasma core into the domain) and $1/(\lambda_n) = n'/n = const.$ and $1/(\lambda_T) = T'/T = const.$ at the separatrix. The boundary conditions for eq. (3.2) are $N(Z, g) = 0$ at both boundaries.

From the equations above, we can understand the dithering cycle as follows: in the L-mode, $g_1 > g$, so $g - g_1 < 0$ so that $Z > 0$ and $D \approx D_{max}$ (i.e. L-mode conditions). If, as done in the experiment by heating, we increase q_{in}, the temperature gradient rises and for $g > g_H$, we transit into H-mode ($Z < 0$, $D \approx D_{min}$). The reduction in transport coefficients leads to an increase in both density and temperature gradients. From eq. (3.4) it can be seen that the response of g to a change in n and T is different: with our

boundary conditions, $n_{sep} = \lambda_n n'_{sep}$ and $T_{sep} = \lambda_T T'_{sep}$, so $g_{sep} \propto T/n$ holds. A rise in T drives the system further into the H-mode whereas the rise in n drives it back towards the L-mode. The initial change in n can be estimated using

$$\frac{\partial n}{\partial t} = \frac{\partial D}{\partial x}\frac{\partial n}{\partial x} + D\frac{\partial^2 n}{\partial x^2} \tag{3.12}$$

At the L-H transition, the main change in n comes from the first term on the RHS. Using the boundary condition, we arrive at

$$\frac{1}{n_{sep}}\frac{\partial n_{sep}}{\partial t} \approx \frac{\partial D}{\partial x}\frac{1}{\lambda_n} \tag{3.13}$$

A similar equation can be derived for T_{sep}. The necessary condition for dithers to appear is $dg_{sep}/dt < 0$ after the transition. Replacing $\partial D/\partial x$ by $(D_{max} - D_{min})/\Delta$ and $\partial\chi/\partial x$ by $(\chi_{max} - \chi_{min})/\Delta$, where Δ is the typical width of the transport barrier, we arrive at the necessary condition for the dithering cycle

$$\frac{1}{\lambda_n}(D_{max} - D_{min}) > \frac{2}{3}\frac{1}{\lambda_T}(\chi_{max} - \chi_{min}) \tag{3.14}$$

(note that this is not a sufficient condition as g may decrease, but, depending on the choice of g_0 and g_1, never reach the value g_L where it transits to L-mode again). For small ramp rates of the heating power, dithers may be expected using experimental values [The ASDEX Team, 1989] of $\lambda_n \approx 1$ cm, $\lambda_T \approx 3$ cm, χ and D as mentioned above. If g decreases below g_L, the system will go back to L-mode, then decrease the density gradient and go into the H-mode again. This happens until the heating (increase in q_{in}) finally overcomes the decrease in g due to the steepening of the density gradient and the system stays in H-mode.

In order to correctly describe the dynamics of the cycle, we have to consider another timescale: once the barrier is established, the first term of the RHS of Eqn. (3.12) vanishes and normal diffusion (second term on the RHS) becomes dominant. The rise in n is now governed by

$$n(t) = n_L + (n_H - n_L)(1 - e^{-\frac{t}{\tau_n}}) \tag{3.15}$$

where $\tau_n \approx \Delta^2/D_{min}$ is the diffusion time in the barrier and the values n_L, n_H are the steady state edge values in H-mode or L-mode: in steady state, $\Gamma_{in} = \Gamma_{out}$ and

$$n_{sep} = \Gamma_{in}\lambda_n/D_{sep} \tag{3.16}$$

It is this timescale that governs the evolution of g after the initial jump introduced by the change in D. Similar equations hold for the response of T to the jump in χ.

The timescale of the dithering cycle is thus given by the time it takes to change the gradients in the transport barrier region. In our simulations, this is typically a width of ≤ 1 cm at a diffusion coefficient in between 0.1 and 1 m^2/s. From this, a typical

timescale of 1-10 kHz results. It should be noted that the experimental results presented in the previous section confirm the existence of this timescale.

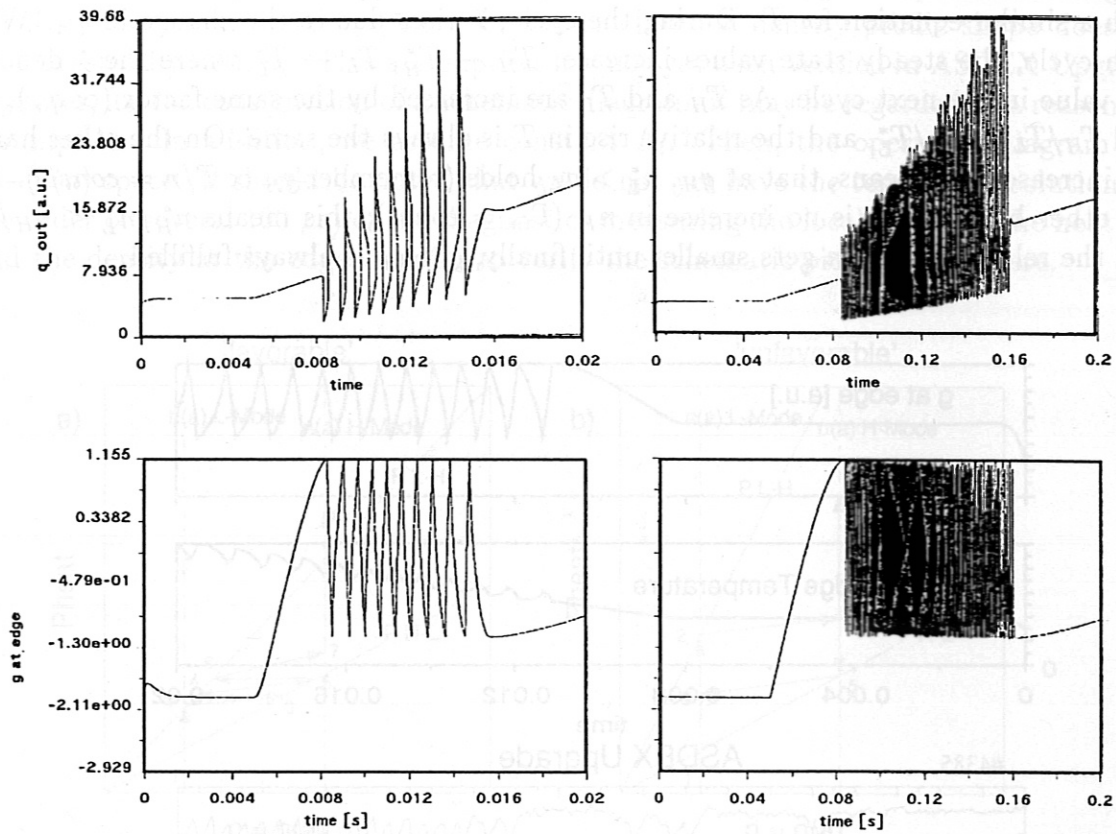

Figure 3.8: *Temporal evolution of q_{out}, the heat flux at the separatrix, and g, the gradient parameter, in response to different ramp rates of q_{in}. Left: ramp from L- to H-mode in 10 ms, right: ramp from L- to H-mode in 100 ms. Note the different time axis.*

We now consider the effect of the heating power: the ramp in q_{in} leads to a continuous rise in T and drives g into the region $g > g_H$ i.e. into stationary H-mode. If the temperature rise rate is small compared to the frequency of the dithering cycles, many dithers are observed, whereas for a fast rise, only few dithers appear. This explains why the number of cycles depends on the power ramp rate as shown in Fig. 3.1. Fig. 3.8 shows the temporal evolution of the gradient parameter and the heat flux out of the plasma obtained from modelling for two different ramp rates.

With a slow rise in heating power we are also able to reproduce the experimental observation of the shape of the D_α trace. An example from the modelling is shown in Fig. 3.9: at the first L-H transition, g decreases quickly from g_H to g_L, in the subsequent transitions, this timescale gets slower and slower. The reason for this is a difference of the temporal evolution of n and T due to Eqn. (3.15). For $t/\tau_n \ll 1$, the rate of change

of n is given by

$$\dot{n}/n_L \approx (n_H/n_L - 1)/\tau_n \tag{3.17}$$

with a similar equation for T. During the cycle, T rises due to the change in q_{in}. With each cycle, the steady state values increase: $T_H \rightarrow T_H^*$, $T_L \rightarrow T_L^*$ where the * denotes the value in the next cycle. As T_H and T_L are increased by the same factor ($\propto q_{in}$), we find $T_H/T_L = T_H^*/T_L^*$, and the relative rise in T is always the same. On the other hand, the increase in T means, that at g_H, $n_L^* > n_L$ holds (remember $g_H \propto T/n = const.$). On the other hand, there is no increase in n_H ($\Gamma_{in} = const$); this means $n_H^*/n_L^* < n_H/n_L$ and the relative rise of n gets smaller until finally, $g > g_L$ is always fulfilled.

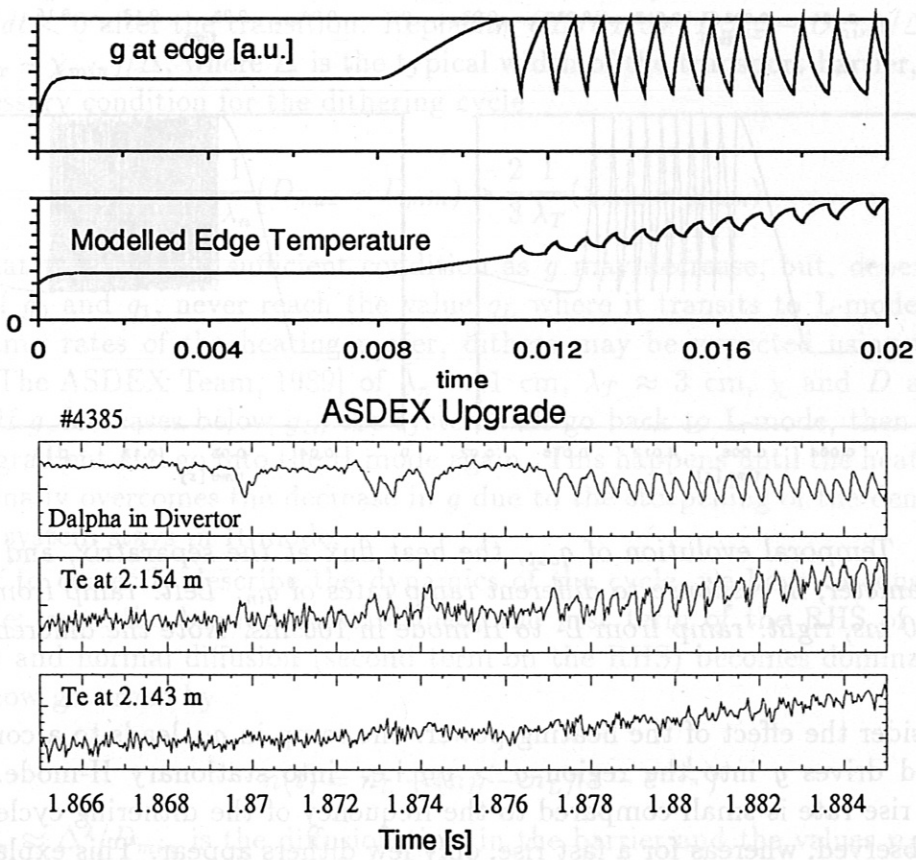

Figure 3.9: *Results from numerical simulations: temporal evolution of the gradient parameter g and the edge electron temperature $T_e(a)$. Also shown are the measured time traces of D_α and $T_e(a)$. There is good agreement between the modelled and measured $T_e(a)$ traces.*

The change in the rise rate of n leads to the observed change in the signal shapes allowing for longer and longer H-mode phases. Fig. 3.9 also shows the experimental time traces from Fig. 3.3. As can be seen, there is good agreement in the temporal behaviour of

$T_e(a)$, even in details of the signal shape.
We use the model described above to draw a schematic picture of the cycles in terms of the operation diagram P_{sep} versus $\bar{n}_e B_t$: due to the T/n dependence of g_{edge}, the thresholds approach the straight lines $P_{thr}^{LH} \propto \bar{n}_e$ found in the ASDEX Upgrade operational diagram 2.2 if we assume $n(a) \propto \bar{n}_e$, i.e. the typical L-mode density profile shape does not vary drastically with $\bar{n}_e$. This assumption has not yet been verified in ASDEX Upgrade. However, for the construction of a schematic diagram, it may be regarded as a reasonable assumption. In addition, we assume constant B_t. Then, the operation diagram is a $P - n(a)$ space. It should be noted that we do not yet have the temporal resolution (on the order or several 100 μs) of the diagnostics measuring the local values of the heat flux and the density at the edge in order to verify the schematic picture given here.

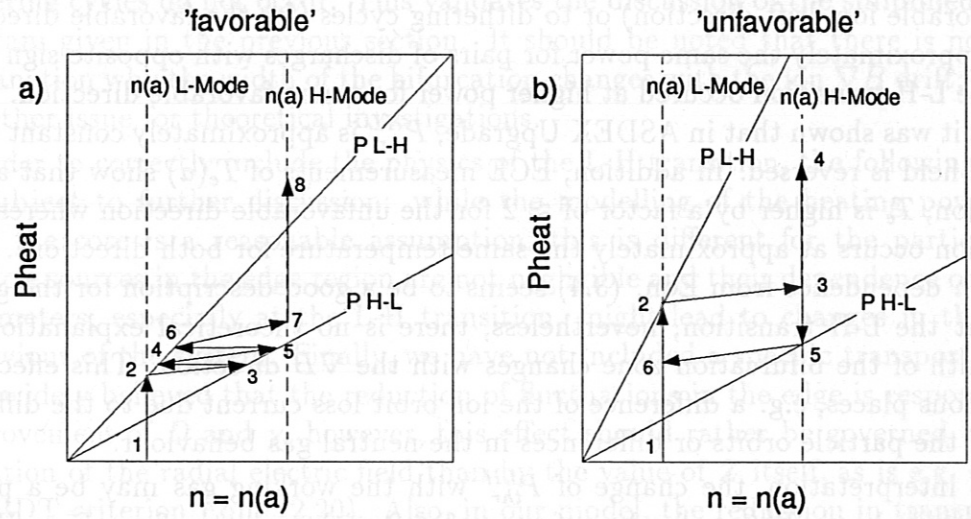

Figure 3.10: *Schematic operation diagram: path a) corresponds to a dithering transition, path b) to one without dithers. In b), P_{thr}^{LH} has been increased by a factor of 1.8 with respect to a), whereas P_{thr}^{HL} was not varied.*

Figure 3.10 a) shows a path of the temporal evolution for a dithering discharge: the vertical lines in the diagram are given by the edge densities in stationary L-mode and H-mode, corresponding to maximal and minimal values of the diffusivities, respectively. The boundaries for the L-H and the H-L transition are shown as obtained from ASDEX Upgrade data for the favorable drift direction, i.e. $P_{thr}^{LH} \approx 1.8 P_{thr}^{HL}$. We approach the threshold at n_L ($1 \rightarrow 2$). At the threshold, the system transits to H-mode and $n(a)$ rises. At low γ_P, the path reaches the H-L threshold ($2 \rightarrow 3$) and the back transition with a subsequent decrease of $n(a)$ occurs. Due to the increase in heat flux, the return point at the L-H boundary (4) is shifted in P. This goes on until the path reaches the n_H line before it reaches the H-L boundary (7). Then, the path follows the n_H line to its final point (8). Thus, dithering cycles may occur when the edge density can make the full swing between the L-H and H-L thresholds without being limited by the extremal diffusivities.

In this diagram, we can modify the path in several ways to avoid dithers. One is to increase γ_P and therefore increase the slope of path $2 \rightarrow 3$. This explains the experimental observation that the number of dithers occuring at the transition decreases with γ_P. Another way is to change the width of the hysteresis. This is shown in Figure 3.10 b), where we have kept the H-L boundary from a) and have increased the L-H boundary by a factor of 1.8 in order to match the higher value of P_{thr}^{LH} observed in experiments with the unfavorable drift direction [Ryter et al., 1994]. Now, on the path into ($1 \rightarrow 2 \rightarrow 3 \rightarrow 4$) and out of the H-mode ($4 \rightarrow 5 \rightarrow 6$), no dithers occur. An increase in the H-L boundary by the same factor would have given a picture similar to a). Thus, we find that in order to explain the absence of dithers for the unfavorable direction, we have to increase the width of the bifurcation zone in the diagram for the unfavorable direction. An experimental indication for this can be seen in Figure 3.6: the back transition to L-mode (with unfavorable ion drift direction) or to dithering cycles (for the favorable direction) occurs for approximately the same power for pairs of discharges with opposite sign of B_t although the L-H transition occured at higher power for the unfavorable direction. Also, in chapter 2 it was shown that in ASDEX Upgrade, P_{thr}^{HL} is approximately constant when the toroidal field is reversed. In addition, ECE measurements of $T_e(a)$ show that at the L-H transition, T_e is higher by a factor of ≈ 2 for the unfavorable direction whereas the H-L transition occurs at approximately the same temperature for both directions. Note that the T/n dependence from Eqn. (3.4) seems to be a good description for the global behaviour at the L-H transition, nevertheless, there is no theoretical explanation yet why the width of the bifurcation zone changes with the ∇B direction. This effect can enter in various places, e.g. a difference of the ion orbit loss current due to the different geometry of the particle orbits or differences in the neutral gas behaviour.

Within this interpretation, the change of P_{thr}^{LH} with the working gas may be a profile effect: as stated above, P_{thr}^{LH} varies by a factor of ≤ 2 with a change from D to H, but still dithers occur only with the favorable drift direction. Therefore, the relative width of the bifurcation only changes with the sign of the ∇B drift, but is the same for all working gases with the same direction of B_t. This is confirmed by the experimental observation that the P_{thr}^{LH} and P_{thr}^{HL} values for the different working gases and drift directions can be obtained by multiplying the values for deuterium by a factor that is approximately a constant for each individual gas species. The change in the absolute value of P_{thr}^{LH} may be explained by the T/n dependence of g in Eqn. (3.4): in ASDEX, at constant $\bar{n}_e$, the value of $n(a)$ in hydrogen was higher by a factor of ≈ 1.3 than in deuterium [Bessenrodt-Weberpals et al., 1993]. At constant heat flux into the edge, $T_e(a)$ is reduced by the same factor. Therefore, to obtain a constant $T(a)/n(a)$ for a given heating power, the value of $T(a)$ has to be higher in hydrogen discharges by a factor of $1.3^2 = 1.7$. Thus, the power threshold should be higher by at least this factor.

3.3 Implications for H-Mode Models

We have shown that, with a simple bifurcation model, we can reproduce the experimental signatures of the dynamics of the L-H transition. For this, we used the numbers g_0 and g_1 as free parameters. For given α and β in Eqn. (3.3), the width of the bistable region of the gradient parameter g is fixed and thus g_0 and g_1 determine the width of the bistable region in T and n. Thereby, the frequency of the dithering cycles is determined. In our modelling, we chose g_0 and g_1 in order to match the experimentally observed frequency. In this parameter regime, the timescale of the dithering cycle is determined by diffusion across the width of the transport barrier rather than by the magnitude of the jump in the transport coefficients at the transition. If, however, we increase the width of the bifurcation by a factor of ≈ 2, in order to model the change of P_{thr}^{LH} with reversed field, dithering cycles do not occur. This validates the discussion of the simplified operational diagram given in the previous section. It should be noted that there is no theoretical explanation why the width of the bifurcation changes with the ion ∇B drift; this remains a further issue for theoretical investigations.

In order to correctly include the physics of the L-H transition, the following points may be subject to further discussion: while the modelling of the heating power as a flux from the core is a reasonable assumption, this is different for the particle flux: the particle sources in the edge region are not negligible and their dependence on the plasma parameters, especially at the L-H transition, might lead to changes in the dynamical behaviour of the system. Finally, we have not included a specific transport model; it is now widely believed that the reduction of fluctuations in the edge is responsible for the improvement of D and χ, however, this effect should rather be governed by the radial variation of the radial electric field than by the value of Z itself, as is e.g. expressed in the BDT criterion Eqn. (2.20). Also, in our model, the reduction in transport appears instantaneously when the system reaches $g = g_H$. Here, physics understanding of the process might introduce a new timescale. However, if the BDT mechanism is responsible for the reduction of fluctuations, this timescale should be significantly shorter than the lifetime of an eddy ω_t. In Section 2.2.2 it was shown that $\omega_t \approx 10^{-4}$ s, so that the reduction of fluctuations should be instantaneous when viewed on the timescale of the dithering cycles (≤ 1 ms).

In summary, the fact that our simplified model reproduces many of the experimental results shows that the dependence of Z on the gradient parameter g in the form of Eqn. (3.4) may explain the bifurcation character of the H-mode. In this model, the bifurcation comes from the multivalued dependence of the poloidal rotation or radial electric field on the plasma parameters; the reduction of fluctuations itself is not multivalued with respect to Z. As shown in [de Blank and Zohm, 1994], including other physics effects in the derivation of $Z(T, n)$ leads to changes in the parametric dependence of the form

$$Z = Z(\hat{g}) \quad \text{with} \quad \hat{g} \sim \frac{T^\alpha}{n}\left(\frac{n'}{n} + \gamma\frac{T'}{T}\right) \tag{3.18}$$

where α varies between 1 (yielding the ansatz discussed above) and 5/2. It is however

clear from the discussion above that this general ansatz will always lead to the possibility of dithering cycles due to the counteracting effects of T and n.

Chapter 4

Edge Localized Modes (ELMs)

In this chapter, the so-called Edge Localized Modes (ELMs) are discussed. We extend the motivation for ELM studies given in Chapter 2 by analyzing the aspects of stationarity of H-mode discharges. It is shown that, to our present knowledge, only the ELMy H-mode can provide stationary conditions. Then, ELMs are described in detail. A phenomenological classification involving experimental observations from several tokamak experiments is given. After this, we analyze the effect of ELMs on the confinement of particles and energy. Based on this phenomenological description, we review the existing ELM models and try to establish a physics picture of the phenomenon.

4.1 The Problem of Stationarity

Fig. 4.1 shows an analysis of the instationary H-mode discharge previously shown in Fig. 2.1. In Chapter 2 we have seen that the energy flux conducted through the separatrix, $P_{sep} = P_{tot} - dW/dt - P_{rad}(core)$ determines whether the plasma is in the H- or the L-mode. Fig. 4.1 shows the temporal evolution of P_{sep}: after the onset of NBI heating at $t = 1.8$ s, P_{sep} rises. Consequently, the heating power in excess of P_{thr}^{LH} becomes positive and the L-H transition occurs (the values for P_{thr}^{LH} and P_{thr}^{HL} in Fig. 4.1 are taken from the scaling law decribing the power threshold in ASDEX Upgrade). This leads to a continuous increase in density and thus, P_{thr}^{LH} rises (remember $P_{thr}^{LH} \sim P_{thr}^{HL} \sim \bar{n}_e$). In addition, $P_{rad}(core)$ increases, leading to a reduction of P_{sep}. Thus, at $t = 1.88$ s, the heating power in excess of P_{thr}^{LH} becomes negative. However, due to the hysteresis, the plasma stays in H-mode, as $P_{sep} > P_{thr}^{HL}$ still holds, indicated by the positive value of the power in excess of P_{thr}^{HL}. Finally, at $t = 2.07$ s, the further increase in P_{rad} and $\bar{n}_e$ leads to $P_{sep} \leq P_{thr}^{HL}$ and the back-transition to L-mode occurs. Note that in the calculation of P_{sep}, the NBI power and the dW/dt correction have been smoothed with a time-constant of 8 ms to avoid numerical noise when calculating the temporal derivative; thus, the time of the L-H transition does not exactly coincide with $P_{sep} \geq P_{thr}^{LH}$.

We will now show that the reason for the increase of $\bar{n}_e$ and P_{rad} after the L-H transition is the improved confinement of particles, both the main plasma species and additional

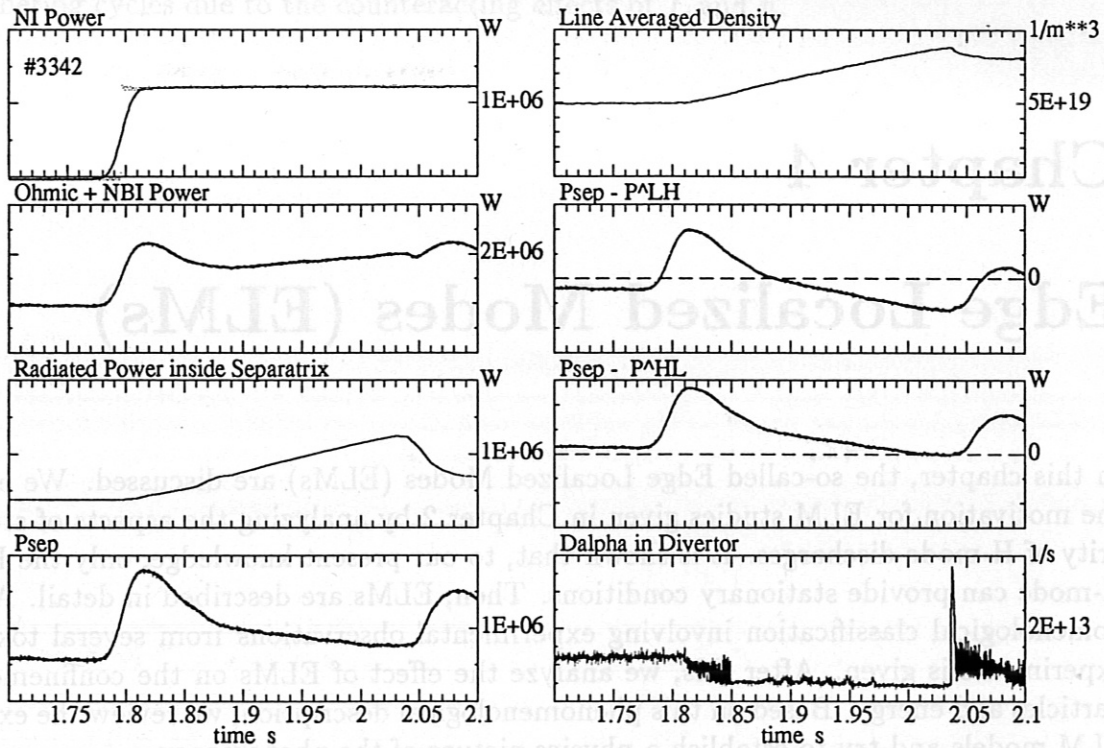

Figure 4.1: *Instationary H-mode discharge: due to the increase of radiated power, P_{sep} decreases and the plasma transits back to L-mode.*

impurities. Due to the continuous increase of $\bar{n}_e$, the radiation loss due to Bremsstrahlung increases ($P_{Brems} \sim n_e^2\sqrt{T}$, see Eqn. (1.8)). However, a quantitative analysis shows that the increase in electron density cannot explain the whole rise in P_{rad}: the density increases by a factor 1.7, leading to an increase of P_{Brems} by a factor 2.9 (the weak $\sqrt{T}$ dependence of P_{Brems} is neglected). The actual increase in P_{rad} is a factor of 4.3, indicating that additional radiation losses play a role. A spectroscopic analysis of similar discharges in ASDEX Upgrade reveals that also the impurity content, in this case especially of low-Z impurities such as C and O, increases. This leads to significant radiation losses, mainly in the plasma edge where line radiation from not yet fully ionized impurities effectively enhances the radiation level. This is confirmed by the the radiation profile shown in Fig. 4.2 (reconstructed from 72 lines of sight of a bolometer): the main contribution to the radiative loss indeed comes from the plasma edge and not, as would be expected if Bremsstrahlung was the dominant contribution, from the plasma centre.

Note that, contrary to the continuous increase in density, the energy content reaches a constant value within the time interval shown; this means that $\tau_E \ll \tau_p^*$. Thus, due to the uncontrollable evolution of the particle content, this type of H-mode, the so-called ELM-free H-mode or H*-mode, does not become stationary on the timescale of several τ_E. The particular case shown in Fig. 4.1 transits back to the L-mode.

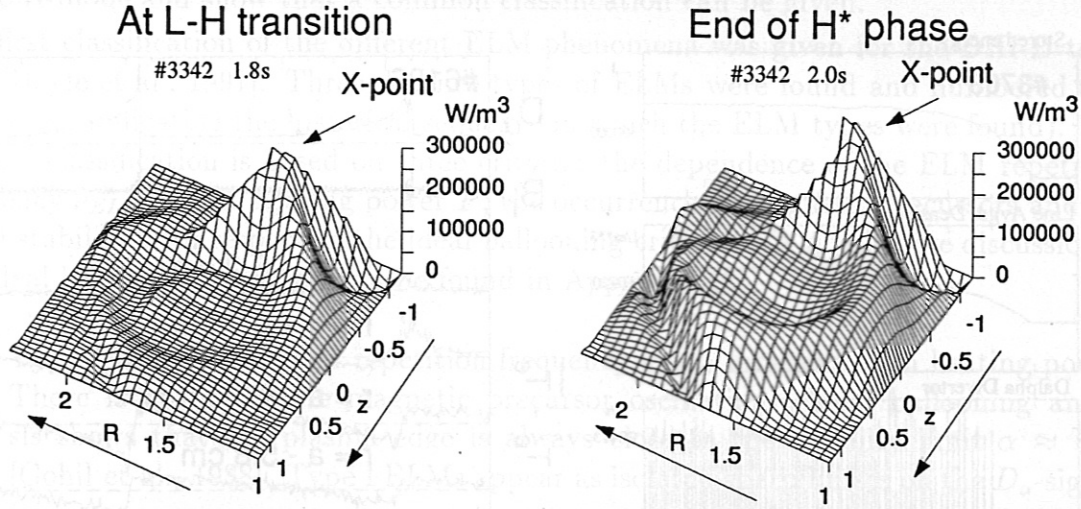

Figure 4.2: *Reconstructed bolometric radiation profiles of the H-mode discharge shown above. It can be seen that prior to the H-L transition, the radiation mainly comes from the plasma edge indicating that line radiation of impurities significantly contributes to the radiation losses.*

This leads to a loss of impurities as well as deuterium (indicated by the decrease of $\bar{n}_e$). As a consequence, P_{rad} and P_{thr}^{HL} decrease and the plasma transits into H-mode again. In other cases, the discharge may suffer a disruption after the back-transition. In the ASDEX tokamak, it was found that discharges attaining the H*-mode have a significantly enhanced probability to disrupt when compared to the ELMy H-modELMy H-mode [Zohm et al., 1993].

From this it is clear that the H* mode is not a suited operation regime for a fusion reactor in which stationarity should be obtained. Also, control of the particle inventory is not possible in the H*-mode. This is especially important for the removal of the He ash in a fusion reactor. It was already shown in Chapter 2 that another type of H-mode discharges, the ELMy H-mode exists. It is characterized by the occurrence of the ELMs, a repetitive loss of particles and energy from the edge.

Fig. 4.3 shows again the time traces from the ELMy H-mode shown in Fig. 2.1. In addition, the temporal evolution of the edge electron temperature is shown for a similar discharge on an expanded timescale. The location of the separatrix is at $r = a$. Outside the separatrix, T_e increases during the ELM, indicating that the rapid outward transport induced by the ELM leads to a temporary heating of the SOL plasma. Inside the separatrix, the effect of the ELMs is to rapidly reduce T_e. It can be seen that the effect of ELMs is really 'edge localized', i.e. T_e is not affected inside a certain radius r_{ELM} (in the case shown above, $r_{ELM}/a \approx 0.8$). The ELM itself happens on a timescale of $\leq$ 1 ms, which is faster than the inverse of typical ELM repetition frequencies of $\nu_{ELM} =$ 10-200 Hz. Thus, ELMs appear as short, separated bursts. In addition, Fig. 4.3 shows

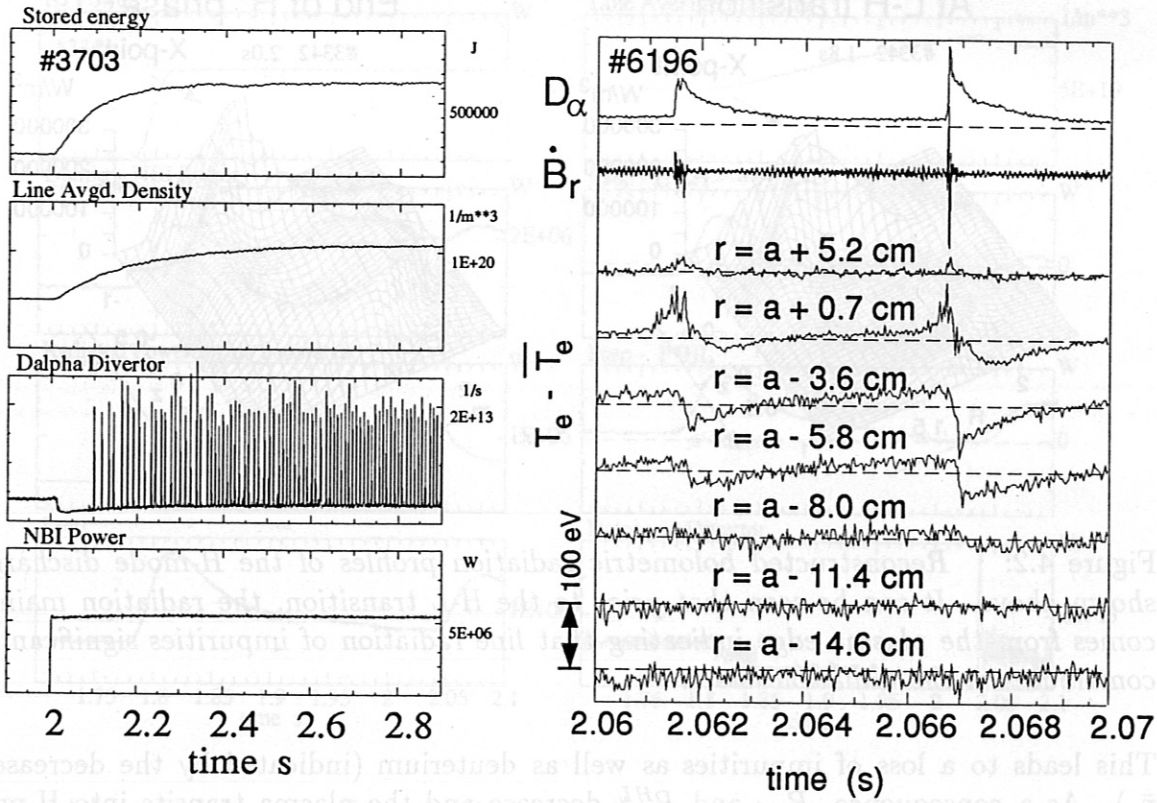

Figure 4.3: *Stationary H-mode discharge with ELMs. The effect of ELMs on T_e in the plasma edge is shown for a similar discharge. There is no effect of the ELMs on T_e for $r \leq 0.8a$.*

the fluctuating magnetic field, measured by a pick-up coil in the outside midplane of the torus (signal $\dot{B}_r$). During ELMs, there is a high level of magnetic fluctuations, indicating that the rapid enancement of transport is due to an MHD instability.

From Fig. 4.3, one can see that the ELMy H-mode leads to stationary conditions on the timescale of τ_E, although the edge temperature undergoes cycles of the rapid ELM loss and a subsequent rise until the next ELM happens. In the DIII-D and the ASDEX tokamak it was demonstrated that ELMy H-mode discharges can be sustained for many (≥ 50) confinement times in stationary state [Burrell et al., 1989], [Vollmer et al., 1991]. This gives a strong motivation for the characterization and the understanding of the ELM phenomenon.

4.2 Phenomenology of ELMs

The physical mechanisms of the different ELM phenomena are complex and no first principles theory describing ELMs exists. We therefore give a phenomenological description

based on the experimental observations of several magnetic fusion experiments operating in the H-mode and show that a common classification can be given.

The first classification of the different ELM phenomena was given for the DIII-D tokamak [Doyle et al., 1991]. Three distinct types of ELMs were found and numbered (the numbering indicating the historical sequence in which the ELM types were found). The original classification is based on three criteria: the dependence of the ELM repetition frequency ν_{ELM} on the heating power P, the occurrence of magnetic precursors and the MHD stability with respect to the ideal ballooning criterion. A qualitative discussion of the ideal ballooning criterion can be found in Appendix C.

- Type I ELMs: the ELM repetition frequency ν_{ELM} increases with heating power. There is no detectable magnetic precursor oscillation. Ideal ballooning analysis shows that the plasma edge is always close to the stability limit $\alpha \approx \alpha_{crit}$ [Gohil et al., 1988]. Type I ELMs appear as isolated sharp bursts on the D_α-signal.

- Type II ELMs: if, in a DIII-D discharge exhibiting type I ELMs, the shape of the plasma cross-section is changed towards higher elongation and triangularity, the appearance of the ELMs may change: they get more frequent and the magnitude of the D_α burst decreases. In this case, the plasma edge is found to be in the connection regime between the first and the second stable region of the ballooning diagram described in Appendix C [Ozeki et al., 1990]. For type II ELMs, no information on the power dependence of ν_{ELM} and the MHD precursor activity exists.

- Type III ELMs: the ELM repetition frequency decreases with heating power. A coherent magnetic precursor oscillation of frequency $\nu_{prec} \approx 50-70$ kHz is observed on magnetic probes located close to the plasma in the outboard midplane. A toroidal modenumber of $n \approx 5 - 10$ was inferred. The plasma edge pressure gradient is significantly below the ideal ballooning limit, i.e. $0.3 \leq \alpha/\alpha_{crit} \leq 0.5$ [Zohm et al., 1995a].

Thus, in a discharge where the heating power increased in steps, type III ELMs occur at heating power close to P_{thr}^{LH}, their frequency decreasing as P is increased until an ELM-free phase appears. At even higher P, type I ELMs occur, their frequency now increasing with P. Fig. 4.4 shows an example.

Another way sometimes used to characterize ELMs is by their D_α-signature: on DIII-D, single, isolated ELMs were called 'giant ELMs', whereas the type II ELMs were dubbed 'grassy ELMs'. Contrary, on ASDEX and JET, highly frequent ELMs occuring at the L-H transition were called grassy ELMs. In addition, the characterization by the D_α signal is not unambiguous, because it depends on the divertor conditions. A somewhat extreme example for this is that in H-mode discharges with a detached divertor, where the energy and particle pulses are buffered in the divertor and do not reach the divertor plates, there is no significant change in the recycling during an ELM and consequently,

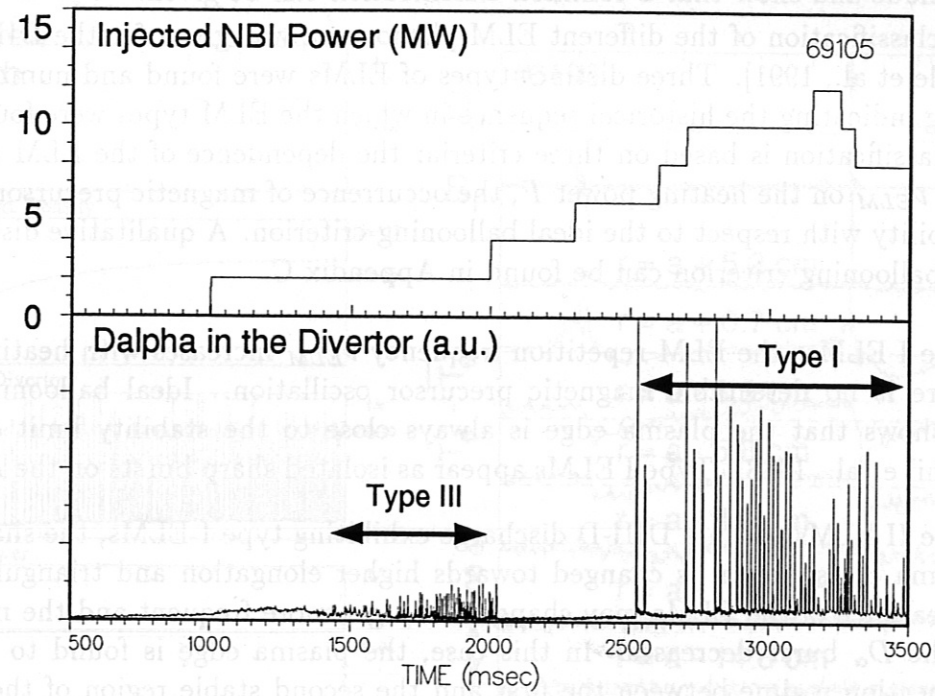

Figure 4.4: *Typical sequence of ELMs during a power rise in DIII-D: at $P \approx P_{thr}^{LH}$, type III ELMs are found, at higher P, type I ELMs occur.*

no peak in the D_α-emission [Kaufmann et al., 1994]. In this case, the characterization of ELMs by the D_α-signal completely fails.

In the following, we will therefore not use the D_α signal for a classification. Instead, we will apply the DIII-D classification to observations from other experiments and point out similarities and differences. After this, a more general classification, taking into account all the experimental results, will be given.

ASDEX

A detailed comparison of the ELM behaviour in ASDEX and DIII-D has been done [Zohm et al., 1995a]. ELMs on ASDEX always exhibit a coherent magnetic precursor oscillation of frequency $\nu_{prec} \approx 180$ kHz and poloidal mode number $m \approx 10 - 15$ [Zohm et al., 1992]. In contrast, the ELM itself is a highly turbulent phenomenon with no clear coherent structure, but a high amplitude of the fluctuating magnetic field. This is shown in Fig. 4.5. The amplitude of the precursor is found to grow explosively before the ELM (see Fig. 4.5 d, which is an enlargement of the second hatched region of Fig. 4.5 b). In other cases, the magnetic mode grows less strongly and then vanish again without the subsequent occurrence of an ELM (see Fig. 4.5 c, enlargement of the first hatched region in Fig. 4.5 b). It was concluded [Zohm et al., 1992], that a critical amplitude of the perturbation must be reached in order to initiate an ELM. In addition

to the occurrence of the magnetic precursor, the ELM repetition frequency on ASDEX decreases with heating power. These observations also hold for type III ELMs in DIII-D. It is therefore concluded that the ELMs appearing on ASDEX are of type III.

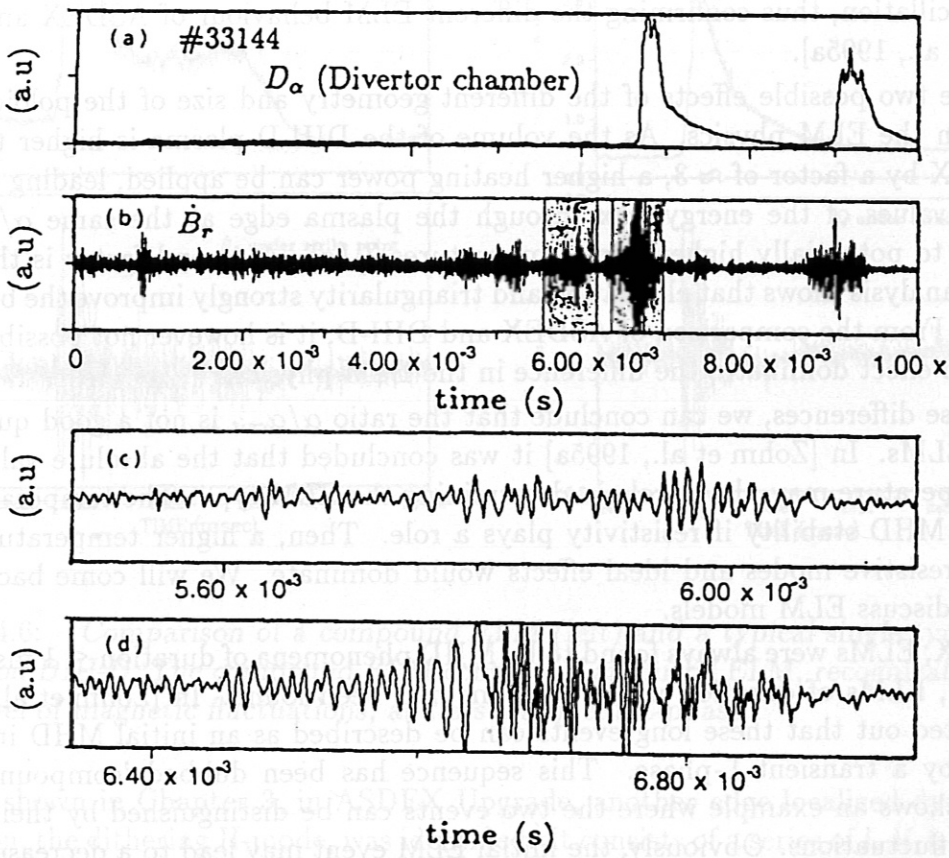

Figure 4.5: *Type III ELMs on ASDEX: Mirnov coil measurements (b) show a coherent precursor. If it grows to sufficient amplitude (d), an ELM is initiated. The ELM itself is a highly turbulent phenomenon (d).*

A pronounced difference exists with respect to the ballooning stability analysis. In ASDEX, only one type of ELM exists during a rise of heating power from the L-H threshold up to the highest available power. For the highest heating power, the plasma was analysed to reach the β-limit. In Appendix C, it is shown that the β-limit is determined by the ideal ballooning stability boundary. This is a clear contradiction to DIII-D, where type III ELMs are only observed at $\alpha/\alpha_{crit} \leq 0.5$ and, at the ideal ballooning limit, type I ELMs occur.

Major differences between DIII-D and ASDEX are the different geometry and the size of the plasma cross-section. Both tokamaks have a major radius of $R_0 = 1.65$ m, but ASDEX has a circular cross-section of minor radius $a = 0.4$ m whereas DIII-D plasmas are normally elongated to $\kappa = 1.8 - 2$ and have a minor radius of $a = 0.63$ m. Experi-

ments were carried out in DIII-D, during which plasmas with cross-section close to the ASDEX shape and size were reproduced. In these discharges, only one type of ELM was found for heating powers from P_{thr}^{LH} up to the β-limit, where the edge was close to the ideal ballooning limit, and it was identified as a type III ELM by its magnetic precursor oscillation, thus confirming the different ELM behaviour of ASDEX and DIII-D [Zohm et al., 1995a].

There are two possible effects of the different geometry and size of the poloidal cross-section on the ELM physics. As the volume of the DIII-D plasma is higher than that of ASDEX by a factor of ≈ 3, a higher heating power can be applied, leading to higher absolute values of the energy flux through the plasma edge at the same α/α_{crit} and therefore to potentially higher edge temperatures $T_e(a)$. A second factor is that MHD stability analysis shows that elongation and triangularity strongly improve the ballooning stability. From the comparison of ASDEX and DIII-D, it is however not possible to find out which effect dominates the difference in the ELM physics.

From these differences, we can conclude that the ratio α/α_{crit} is not a good quantity to classify ELMs. In [Zohm et al., 1995a] it was concluded that the absolute value of the edge temperature may play a role in determining the ELM type. The temperature may influence MHD stability if resistivity plays a role. Then, a higher temperature would stabilize resistive modes and ideal effects would dominate. We will come back to this when we discuss ELM models.

In ASDEX, ELMs were always found to be MHD phenomena of duration ≤ 1 ms whereas in DIII-D, ELMs of duration up to ≈ 10 ms had been found. In [Zohm et al., 1995a], it is pointed out that these long events can be described as an initial MHD instability followed by a transient L-phase. This sequence has been dubbed 'compound ELM'. Fig. 4.6 shows an example where the two events can be distinguished by their level of magnetic fluctuations. Obviously, the initial ELM event may lead to a decrease of T_e to a value below that necessary to sustain the H-mode. The subsequent reheating in the transient L-mode phase then leads to an L-H transition. It was concluded that ELMs are always MHD instabilities of duration ≤ 1 ms which, in a compound ELM, may be followed by a transient L-phase. On DIII-D, the initial ELM event can be either a type I or a type III ELM.

ASDEX Upgrade

In shape and size, the ASDEX Upgrade tokamak is comparable to DIII-D. Consequently, the phenomenolgy is very similar. In ASDEX Upgrade, type I and type III ELMs are clearly identifiable using the power dependence of the repetition frequency. Also, a magnetic precursor oscillation of frequency $\nu_{prec} \approx 70$ kHz and poloidal mode number $m \approx 10$ is found prior to type III ELMs. Compound ELMs can be identified as an MHD event similar to a normal ELM followed by an L-phase lasting for $\approx 5 - 10$ ms. However, no type II ELMs have been identified yet. One reason for this may be that the triangularity in standard ASDEX Upgrade discharges is much lower ($\delta \leq 0.1$) than that in the DIII-D discharges where type II ELMs occurred ($\delta \geq 0.4$).

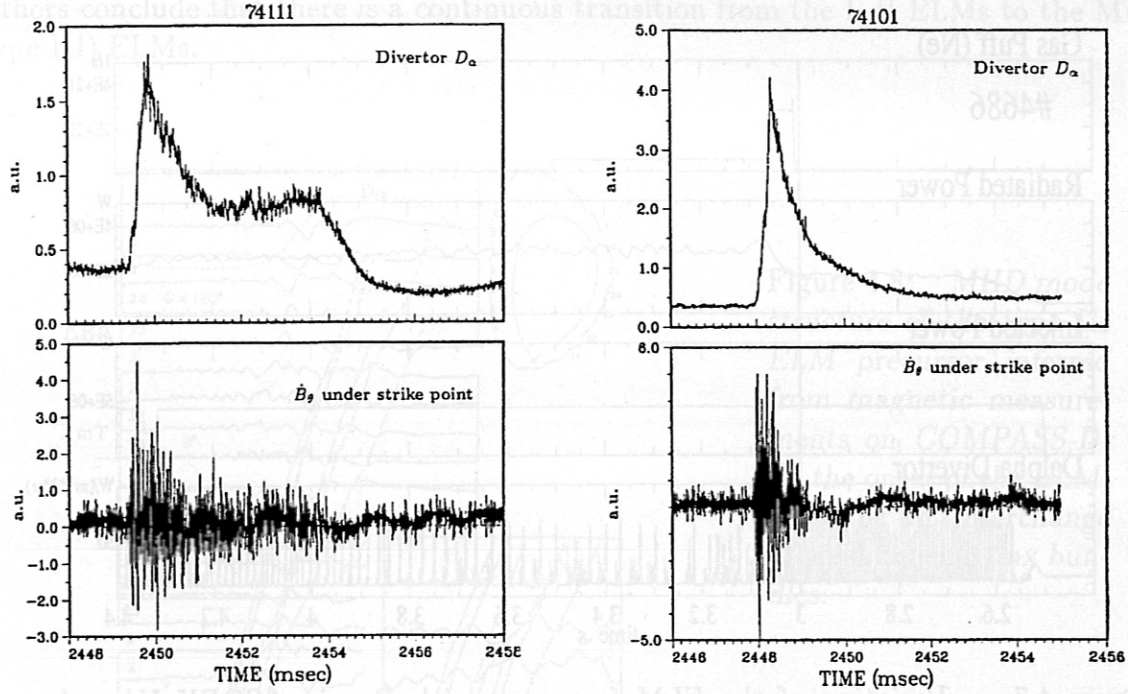

Figure 4.6: *Comparison of a compound ELM (left) and a typical single type I ELM (right) on DIII-D. The compound ELM consists of an initial ELM, recognizable by the high level of magnetic fluctuations, and a subsequent L-phase.*

As was shown in Chapter 3, in ASDEX Upgrade, another edge localized dynamic phenomenon, the dithering H-mode, was identified. It consists of a series of L-H-L transitions when the heating power is of the order of P_{thr}^{LH}. Close to the threshold, also type III ELMs are found. They can be distinguished from the dithering cycles by the occurrence of the magnetic precursor oscillation. Also, as was shown on ASDEX [Zohm et al., 1992], during a type III ELM, the fluctuation level both in the magnetic field and the electron density reaches much higher values than in the temporary L-phase of a dither. However, during a power ramp-up, there is a gradual change from the first cycles that appear right at the transition which show no detectable precursor oscillation up to the last isolated type III ELMs before the ELM-free phase where clear precursor activity is seen. Inbetween, the identification of the first type III ELM is somewhat arbitrary.

In ASDEX Upgrade, it was shown that the power dependence of the ELM frequency is governed by P_{sep}, the energy flux conducted through the separatrix rather than by the absolute value of the applied heating power: the sequence found during a power rise in DIII-D (see Fig. 4.4) is reversed if P_{sep} is reduced by enhancing the radiation losses from the plasma by injection of additional impurities. Fig. 4.7 shows the variation of P_{sep} through injection of Neon, leading to a decrease of the type I ELM frequency. A further increase of the radiated power leads to short ELM-free phases, followed by type

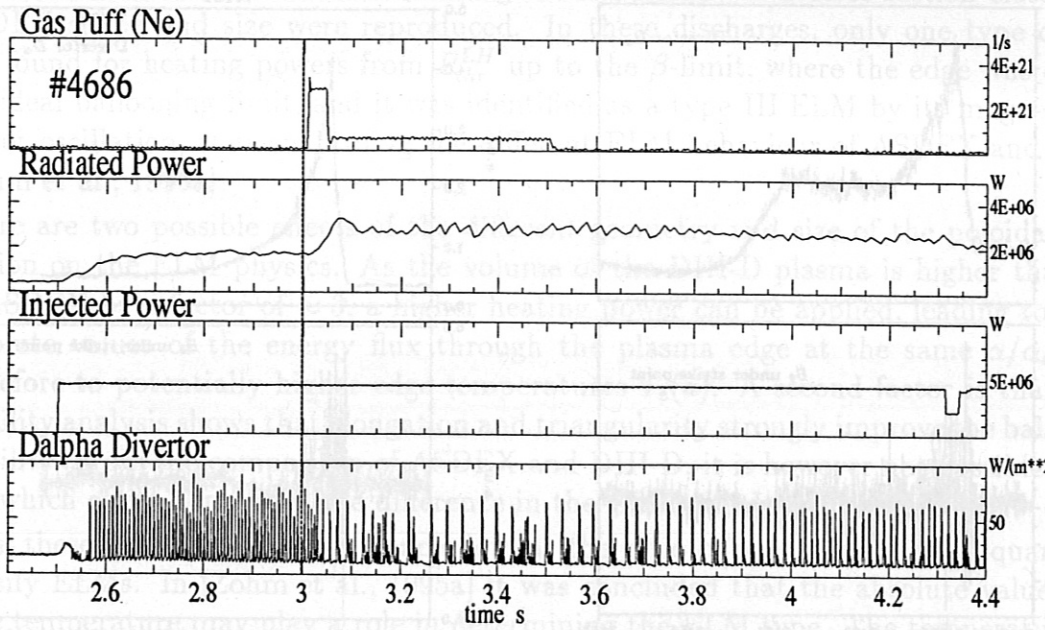

Figure 4.7: *Variation of the ELM frequency with P_{sep} in ASDEX Upgrade. At constant P, P_{sep} is reduced by enhancing the radiative losses through injection of Neon, leading to a decrease of the type I ELM frequency.*

III ELMs.

An interesting observation is that in ASDEX Upgrade, type III ELMs have so far only been observed in discharges with the favorable ion drift direction (towards the X-point). Note that, as shown in Chapter 2, for the unfavorable direction, P_{thr}^{LH} is higher by a factor of ≈ 1.8. For discharges with the same line averaged density, $T_e(a)$ is measured to be higher by a factor of ≈ 2 at the L-H transition for a discharge with the unfavorable drift direction. Again, this points towards an influence of the absolute value of the edge temperature on the type III ELM stability. Another finding presented in Chapter 3 is that for the unfavorable drift direction, no dithering cycles are observed in ASDEX Upgrade either. A possible link between the dithering cycles and type III ELMs will be discussed in section 4.4.

COMPASS-D

The tokamak COMPASS-D has a shape similar to ASDEX Upgrade and DIII-D (elongated cross-section with $\kappa \leq 1.7$), but is smaller (minor radius 0.17 m and major radius 0.56 m). Type III ELMs, characterized by the power dependence of the frequency and the magnetic precursor oscillation have been identified (called 'MHD-ELMs' on COMPASS-D [Valovic et al., 1994]). In contrast, so-called L-H ELMs are distinguished. They appear at the L-H transition and are not single, isolated events, but rather a series of L-H-L transitions, thus bearing similarities to the dithering cycles described in Chapter

2. However, magnetic precursor activity is detected even between these events. The authors conclude that there is a continuous transition from the L-H ELMs to the MHD (type III) ELMs.

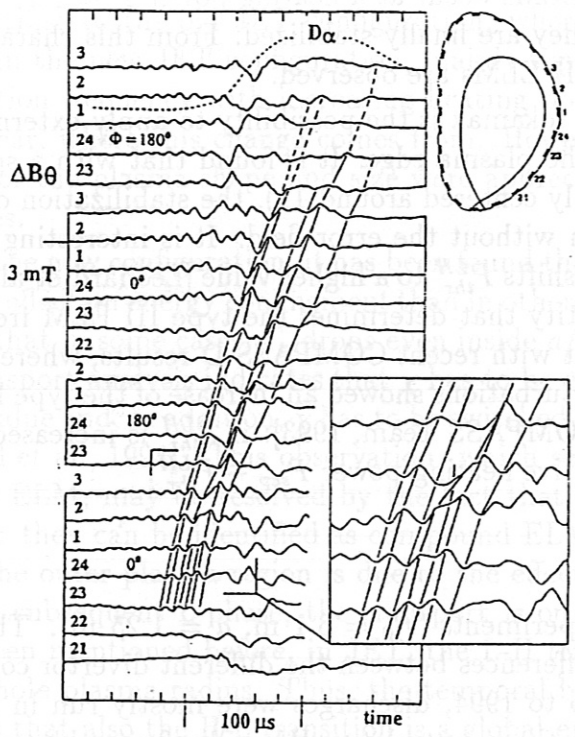

Figure 4.8: *MHD mode structure of the type III ELM precursor inferred from magnetic measurements on COMPASS-D. At the onset of the ELM, there is an interchange of neighbouring flux bundles.*

COMPASS-D is equipped with magnetic pick-up coils close to the plasma on the whole poloidal circumference. With these, it is possible to analyze in detail the structure of the type III ELM precursor [Valovic et al., 1994]. Fig. 4.8 shows such an analysis. The precursor structure (rotating at $\nu_{prec} \approx 100$ kHz) can be traced around the poloidal circumference. A poloidal modenumber of $m \approx 13$ can be inferred. However, at the moment the actual ELM sets in, there is a defect in spatial periodicity which can be visualized as the interchange of poloidally neighbouring field lines carrying current filaments of opposite direction. During the event, the poloidal mode number roughly halves, leading to a wider radial extent of the perturbation. This interchange of neighbouring field lines on a flux surface can also be interpreted as the reconnection of magnetic flux. This would imply that resistivity plays a dominant role in the mechanism initiating the type III ELM.

On COMPASS-D, cases have been found where the magnetic precursor is hardly detectable or does not grow explosively before the ELM event. Therefore, the role of the ELM precursor as the event initiating the ELM is not definitely clear on COMPASS-D.

JFT2-M

In the tokamak experiment JFT2-M ($R_0 = 1.31$ m, $a = 0.21$ m, $\kappa \leq 1.5$), ELMs have been characterized with respect to the power dependence of the repetition frequency [Miura et al., 1991]. It is found that ELMs occur at a heating power $P \approx P_{thr}^{LH}$ and get less frequent as P is increased until they are finally stabilized. From this characteristic it seems clear that in JFT2-M, type III ELMs are observed.

An interesting feature of the JFT-2M tokamak is the possibility to apply external magnetic field perturbations to ergodize the plasma edge. It is found that with a spectrum of high poloidal harmonics (m typically centered around 11), the stabilization of ELMs appears at higher heating power than without the error field. It is interesting to note that application of this error field also shifts P_{thr}^{LH} to a higher value [Leonard et al., 1991]; it seems that $P_{sep} - P_{thr}^{LH}$ is the quantity that determines the type III ELM frequency. These observations could be consistent with recent COMPASS-D results, where the application of external magnetic field perturbations showed an increase of the type III ELM frequency at constant P [Todd and COMPASS Team, 1993]: if P_{thr}^{LH} is increased by the error field, this would reduce the effective heating power $P_{sep} - P_{thr}^{LH}$.

JET

JET is the largest of the tokamak experiments ($R_0 = 3.1$ m, $a = 1.25$ m). The ELM phenomenology of JET shows clear differences between the different divertor configurations installed in the experiment. Up to 1994, discharges were mostly run in X-point configuration with the X-point close to the target plates. We will refer to this configuration as the 'old' divertor. In 1994, a pumped divertor was installed allowing for a longer distance between X-point and target plates. Together with this, the plasma volume was decreased and the standard plasma shape was changed towards lower triangularity. This configuration will be referred to as the 'new' divertor. We will discuss these two configurations separately.

With the old divertor, ELMs were usually observed close to the L-H threshold, their frequency decreasing with heating power. They were therefore identified as type III ELMs. It was shown that the ELM frequency has a strong inverse correlation with ∇p in the edge [Colton and Porte, 1993]. In detail, it was found that ∇n does not change significantly for different H-mode conditions whereas ∇T rises with an increase of heating power, again pointing to a significance of T or ∇T itself in addition to ∇p for the type III ELM behaviour.

Consistent with the classification as type III ELMs, magnetic precursor activity was found [Ali-Arshad et al., 1992]. It consists of a coherent mode at frequency $\nu_{prec} = 80 - 100$ kHz. A toroidal modenumber of $n = 8 - 15$ was inferred. The mode was not found to dramatically grow in amplitude before the ELM. However, the actual ELM, seen as a broadband turbulent event, usually leads to the disappearance of the mode. Thus, a causal relationship between the magnetic oscillation and the ELM seems to exist.

Similar to DIII-D results, an ideal ballooning analysis reveals that during type III ELMs,

the edge pressure gradient is far away from the ideal ballooning limit (typically $\alpha \leq 0.3\,\alpha_{crit}$) [de Blank et al., 1991]. There are also cases where, in the old JET, the edge pressure gradient was found to be close to the ideal ballooning limit; it is suspected that in these cases (e.g. high β_p H-mode [Campbell et al., 1994]), the ELMs are of type I. However, the power dependence of ν_{ELM} in these discharges is not reported.

In contrast to the old JET configuration, where type III was the most common ELM type, in the new JET configuration, mainly type I ELMs, identified by their increasing repetition frequency with increasing heating power, are observed. It is at the moment not clear, where this change comes from. However, as mentioned before, with the new divertor the plasma shape and size were appreciably changed compared to the old discharges.

With the new configuration, it has been found that in some cases, ELMs may have a more severe effect on energy confinement than in others. Spatially resolved measurements of T_e show that in some cases, T_e drops even inside $a/2$ within a few ms after the ELM event. A transport analysis indicates that χ has to be enhanced in the outer plasma region to a high value and, in addition, χ has to be switched to the L-mode value in the whole plasma [Parail et al., 1994]. This observation, which seems to contradict the edge localization of the ELM, may be resolved by the fact that these events last longer than the usual ELMs: they can be identified as compound ELMs. In this interpretation, the enhanced χ in the outer plasma region is due to the effect of the ELM as an MHD phenomenon. In the subsequent L-phase, the transport is on L-mode level in the whole plasma. As has been mentioned before, in JET, the L-H transition happens on a fast timescale on the whole plasma radius. Thus, the temporal behaviour of T_e during compound ELMs proves that also the H-L transition is a global event that propagates to the core plasma much faster than on the diffusive timescale.

Wendelstein VII-AS

In H-mode discharges in the stellarator WVII-AS, short bursts in the D_α light associated with an edge instability are observed. They are identified as ELMs [Wagner et al., 1994]. However, a classification by the criteria applied to the tokamak experiments described above has not yet been made. The power dependence of ν_{ELM} is not yet clear, mainly because ELMs up to now appear as irregular bursts. A magnetic precursor has not yet been found; however, its existence cannot be ruled out on the basis of the experimental results known at present.

WVII-AS differs appreciably from the tokamaks described above. It has a high aspect ratio ($R_0 = 2.0$ m, $a \approx 0.17$ m). The other major difference is that there is no net toroidal current. It should be mentioned that in the edge region, the pressure gradient drives a bootstrap current. A role of this current in determining ELM physics cannot be ruled out [Wagner et al., 1994], although it changes the safety factor by $\leq 1\%$. This points towards a dominant role of the edge pressure gradient rather than the toroidal current as the driving mechanism for the ELMs occuring in WVII-AS.

General classification

From these various experimental observations, we propose to classify ELMs according to the occurrence of the magnetic precursor and the dependence of the ELM frequency on the energy flux through the separatrix, P_{sep}. As has been shown above, ideal ballooning stability is not a good criterion to separate the different ELM types. Also, the shape and magnitude of the D_α-signal in the divertor will not be used to identify a specific ELM type. Finally, we will also not include type II ELMs, because at present, they have only been found in special DIII-D discharges. Instead, we add the dithering cycle as an edge localized phenomenon. We arrive at the following definition

- Type I ELMs: the ELM repetition frequency ν_{ELM} increases with the energy flux through the separatrix:

$$\frac{d\nu_{ELM}}{dP_{sep}} > 0 \tag{4.1}$$

  There is no detectable coherent magnetic precursor oscillation; during the ELM, there is a high level of incoherent magnetic fluctuations.

- Type III ELMs: the ELM repetition frequency decreases with the energy flux through the separatrix:

$$\frac{d\nu_{ELM}}{dP_{sep}} < 0 \tag{4.2}$$

  A coherent magnetic precursor oscillation of toroidal modenumber $n \approx 5 - 10$ and poloidal modenumber $m \approx 10 - 15$ is observed on magnetic probes located close to the plasma. During the ELM, there is a high level of magnetic fluctuations.

- Dithering cycles: For $P_{sep} \approx P_{thr}^{LH}$, repetitive L-H-L transitions may occur. The repetition frequency shows a slight decrease with increasing P_{sep}. Dithering cycles show no magnetic precursor oscillation; the level of turbulence during the temporary L-phase does not significantly exceed that of the L-phase at $P_{sep} \leq P_{thr}^{LH}$.

For both type I and type III, the ELM itself is an MHD event lasting for $0.3 - 1$ ms. Especially, the duration does not seem to vary significantly with the machine size (e.g. JFT-2M and JET report of a duration of ≥ 0.5 ms, although their minor radii vary by a factor of $1.25/0.21 \approx 6$). However, so-called compound ELMs, i.e. ELMs with a subsequent L-phase of 5-15 ms duration have been identified on various experiments. Typical type III repetition frequencies are in the range of 2 kHz (i.e. frequency of the order of the inverse of the duration) down to 200 Hz in steady state ELMy H-mode discharges. Typical type I ELM repetition frequencies are reported in the range of 10-200 Hz. However, for the lowest ELM frequencies, when the inverse of the ELM frequency

is of the order of the confinement time, it remains a matter of definition if one speaks of 'ELM free phases' between the single ELMs.
From the previous discussion, it is clear that classification is valid for all tokamak experiments analysed above.

4.3 ELM Effects on Transport

It was shown above that an ELM leads to a loss of energy and particles from the plasma edge. In this section, we quantify the ELM losses for the two ELM types defined above. Also the effect of an ELM on the plasma outside the last closed flux surface, the so-called scrape-off layer (SOL) is discussed.
The energy loss due to ELMs manifests itself in a reduction of the global energy confinement time τ_E. Studies on DIII-D showed that in a type I ELMy H-mode, τ_E is reduced by roughly 10-15 % [Schissel et al., 1992]. A more general investigation of the influence of ELMs on τ_E was done by establishing a scaling of τ_E in the ELMy H-mode in a way similar to that described in Chapter 2 for the ELM-free scaling, Eqn. (2.4). The result is [ITER H-mode Database Working Group, 1994]

$$\tau_{E,H} = 0.022\, I_p^{0.76} B_t^{0.15} P^{-0.7} M^{0.3} R^{2.6} \bar{n}_e^{0.42} \epsilon^{0.3} \kappa^{1.05} \; [\mathrm{s, MA, T, MW, m}, 10^{19}\mathrm{m}^{-3}] \quad (4.3)$$

A comparison with the ELM-free scaling shows that for present experiments, the reduction in τ_E indeed is of the order of 10-20 %. For bigger devices, especially for the ITER parameters, the ELMy scaling approaches the values of τ_E predicted by the ELM-free scaling (and equals it within the statistical error bars). This might lead to the conclusion that for bigger machines, ELM losses are relatively unimportant in the global power balance. Such a result may be expected if ELMs can be considered a surface effect, i.e. the radius r_{ELM} outside which the ELM affects T and n scales stronger than linear with the absolute dimension of the plasma. However, the scaling given above mixes the different ELM types (type I and type III) with their different power dependence of the repetition frequency. Therefore, the actual conclusion about the importance of ELMs in a big device like ITER has to be examined more carefully in the future.
A different way to estimate the confinement degradation due to ELMs is to assume that ELMs reduce τ_E by a factor η, i.e.

$$\eta = \tau_{E,ELMy} \,/\, \tau_{E,ELM-free} \quad (4.4)$$

We estimate η using a simple model: ELM losses are governed by ν_{ELM}, the ELM repetition rate and ΔE, the energy loss per ELM. It is found on ASDEX Upgrade that, for type I ELMs, $\nu_{ELM} \propto P_{tot}$ and $\Delta E \approx const.$ Thus $P_{ELM} = \nu_{ELM} \Delta E \propto P_{tot}$, and $P_{ELM}/P_{tot} = const.$ The precise value of η has to be found by an analysis of the profile effects due to the ELM. Assuming a diffusive process and spatially separated source and

sink profiles, which is a reasonable assumption for centrally peaked heating profiles, τ_E will be reduced by

$$\eta = 1 - \frac{a^2 - r_{ELM}^2}{a^2} \frac{P_{ELM}}{P_{tot}} \tag{4.5}$$

Typical values from ASDEX Upgrade are $P_{ELM}/P_{tot} \approx 0.3$ and $r_{ELM}/a \approx 0.8$ (see Fig. 4.3) resulting in $\eta = 0.9$, in good agreement with the DIII-D result of 0.85 mentioned above. The scaling of η for future machines critically depends on the scaling of r_{ELM}, which also enters into the scaling of ΔE and therefore P_{ELM}.

Similar to the effect of ELMs on τ_E, the effect on τ_p, the particle confinement time as defined by Eqn. (2.5) is of interest. However, as was pointed out in Chapter 2, an experimental determination of τ_p is very difficult due to the problems with the unknown sources and the recycling of gas. Therefore, a quantitative analysis of the effect of ELMs on τ_p has not yet been given. On the other hand, the ELMy H-mode leads to a stationary behaviour of the density whereas in the ELM-free H-mode, the density normally rises in an uncontrollable way. In both modes of operation, the energy content saturates. From this, we have already concluded that $\tau_E \ll \tau_p^*$ in the ELM-free H-mode. The fact that in the ELMy H-mode the density becomes stationary points towards an increase of the ratio τ_E/τ_p which makes particle density control possible. As was shown in DIII-D, the particle density control in the ELMy H-mode also makes removal of He from the plasma possible [Hillis et al., 1994]. First estimates of the ratio τ_E/τ_p^* yield a number of ≤ 14, which indicates that removal of He ash in a burning plasma may be feasible in the ELMy H-mode.

A difference in the effect of ELMs on particle and energy loss may be due to the different source profiles of energy and particles: as was pointed out in [Lackner et al., 1994], an edge localized loss phenomenon is most severe for a quantity whose source profile is also edge localized, as is the case for particles. For a central source profile, which is mostly the case for plasma heating, the source is not directly affected and the effect is less severe.

The effect of ELMs on the global confinement time as given by e.g. the scaling law (4.3) is temporally averaged over many ELMs. An estimate of the energy and particle loss per single ELM was done on various tokamaks. For type III ELMs, it was found on ASDEX and DIII-D [Zohm et al., 1995b] that the typical energy loss per ELM is of the order of 1-5 % of the total stored energy. The variation comes from the fact that with decreasing type III ELM frequency, the fraction of energy expelled by each ELM increases. However, a quantitative analysis of the frequency dependence has not yet been done. In ASDEX Upgrade, it is found that during a type III ELM the number of particles lost is of the order of 0.5-2 % of the total particle content [Zohm et al., 1994b]. In specific cases, it is found that the assumption of a purely convective loss underestimates the energy loss per ELM, i.e. transport during type III ELMs has a strong conductive component. This is confirmed by the observation that during type III ELMs in ASDEX Upgrade, an energy pulse arrives at the target plates within $\approx 10\mu$s after the ELM onset. This is much faster than the time it takes ions to flow at sound speed along field lines down into the divertor.

It was therefore concluded that the first energy pulse is due to electron heat conduction.

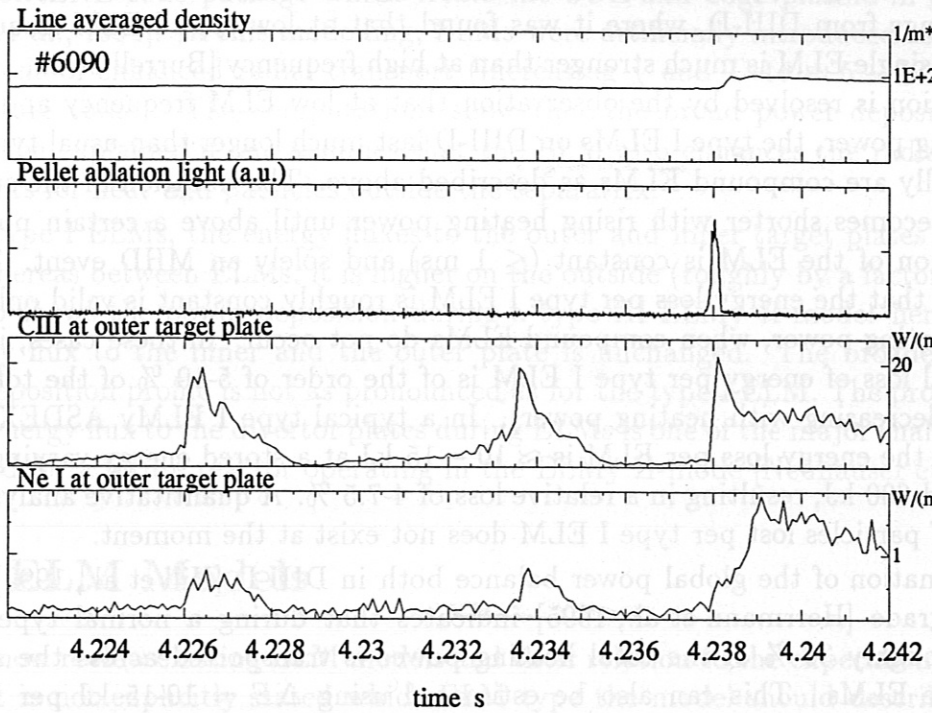

Figure 4.9: *Demonstration of the time delay between the arrival of an ELM generated energy and particle pulse in the divertor. A Neon pellet triggers an ELM. The ELM induced heat pulse reaches the divertor very quickly, as indicated by the almost immediate increase in CIII intensity. The Neon particles reach the divertor with a time delay of* $\approx 0.5 - 1$ *ms.*

The time delay between the particle and energy pulse can be confirmed explicitly for type I ELMs in ASDEX Upgrade. Fig. 4.9 shows a result obtained by the injection of a small Neon pellet into a type I ELMy discharge: due to the increase in edge pressure, the pellet triggers an ELM with a subsequent L-mode. The ablation of the pellet in the midplane can be monitored by the light due to the ablation process viewed by a photodiode. Fig. 4.9 shows the emissivity of a C and a Ne line in the divertor. First, the C line intensity increases, indicating that sputtering of the carbon covered divertor target plates is increased due to the arrival of an energy pulse. However, at this timepoint, the Ne line intensity in the divertor does not increase more than in the preceding ELMs, indicating that the Ne trace impurities brought into the plasma by the pellet have not yet reached the divertor. Again, it must be concluded that the first energy pulse is mainly conductive. After about $0.5 - 1$ ms, the particle pulse arrives at the target plate. This time delay is consistent with the assumption that the particles flow along field lines roughly with the ion sound speed.

It was mentioned above that in ASDEX Upgrade, it was found that the absolute value of the energy loss per type I ELM is roughly constant during a power rise. Together with the linear increase of the ELM frequency with power, this leads to a constant relative

energy loss during a type I ELMy H-mode discharge. This result is somewhat conflicting with findings from DIII-D, where it was found that at low type I ELM frequency, the effect of a single ELM is much stronger than at high frequency [Burrell et al., 1989]. The contradiction is resolved by the observation that at low ELM frequency and therefore low heating power, the type I ELMs on DIII-D last much longer than usual type I ELMs and actually are compound ELMs as described above. The duration of the subsequent L-phase becomes shorter with rising heating power until above a certain power level, the duration of the ELM is constant ($\leq$ 1 ms) and solely an MHD event. Thus, the statement that the energy loss per type I ELM is roughly constant is valid only above a certain heating power, when compound ELMs do not occur. In these cases, in DIII-D, the typical loss of energy per type I ELM is of the order of 5-10 % of the total energy content (decreasing with heating power). In a typical type I ELMy ASDEX Upgrade discharge, the energy loss per ELM is $\approx 10 - 15$ kJ at a stored energy varying between 200 kJ and 600 kJ, resulting in a relative loss of 4-7.5 %. A quantitative analysis for the number of particles lost per type I ELM does not exist at the moment.

An examination of the global power balance both in DIII-D [Hill et al., 1992] and ASDEX Upgrade [Herrmann et al., 1995] indicates that during a normal type I ELMy H-mode roughly 30 % of the total heating power is transported across the separatrix due to the ELMs. This can also be estimated using ΔE = 10-15 kJ per ELM and $\nu_{ELM}/P_{tot} \approx 25$ Hz/MW for typical type I ELMy discharges in ASDEX Upgrade, yielding 20-35 % for the power fraction lost through ELMs. As the duration of the ELM is typically much shorter ($\approx$ 1 ms) than the inverse of the ELM frequency (typically 10-200 Hz), this leads to the occurrence of high peaks in the energy flux to the target plates during ELMs. Fig. 4.10 shows an example from ASDEX Upgrade.

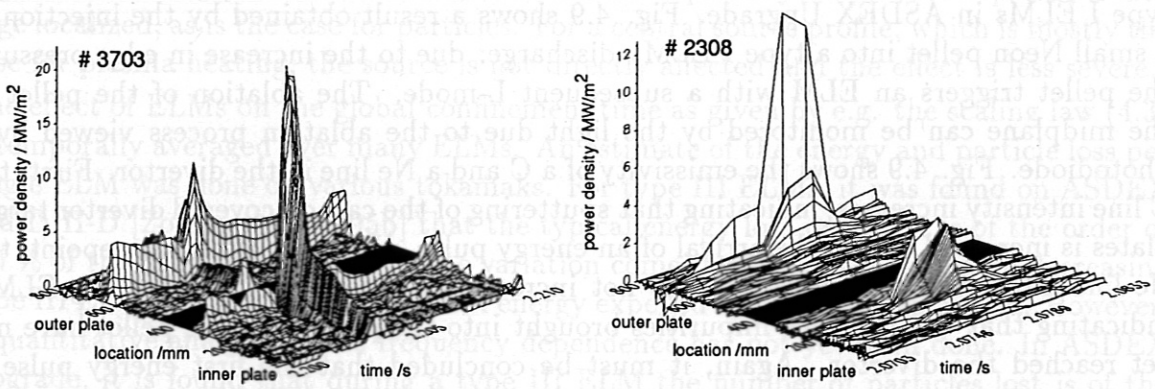

Figure 4.10: *Power deposition on the target plates of ASDEX Upgrade in a type I ELMy H-mode (left) and a type III ELMy H-mode (right).*

During type I ELMs, the energy flux can be as high as 20 MW/m^2, whereas inbetween ELMs, it is below 5 MW/m^2. In addition, a significant broadening of the depo-

sition profile on the target plate is found. The power deposition has been modelled by the B2-EIRENE code package which treats the SOL and edge plasma in great detail [Coster et al., 1994]. In this modelling, ELMs were artificially introduced as short (≈ 1 ms) periods of enhanced radial transport (increasing χ and D to $\approx 5 - 10$ times their steady state value). The computations show that the broad power deposition profile can only be explained if one assumes that the ELM also enhances the radial transport coefficients for heat and particles outside the separatrix.

During type I ELMs, the energy fluxes to the outer and inner target plates are comparable, whereas between ELMs, it is higher on the outside (roughly by a factor of 2). Fig. 4.10 also shows the power deposition during a type III ELMy H-mode: here, the ratio of energy flux to the inner and the outer plate is unchanged. The broadening of the power deposition profile is not as pronounced as for the type I ELM. The problem of the peaked energy flux to the divertor plates during ELMs is one of the major challenges to be addressed for a future reactor operating in the ELMy H-mode [Neuhauser et al., 1992].

4.4 ELM Models

We will now review existing ELM models and their relation to the experimental findings. Often, it is not explicitly stated which ELM type the model should describe; in these cases, we will try to determine the ELM type potentially described by the model. Two basic types of models exist: one is the description of ELMs as a limit cycle oscillation at the L-H threshold or, if additional physics such as a stability limit is put into the model, at higher heating power. These models do generally not describe the detailed physics of the ELM process. The other class of models uses MHD stability analysis to find MHD modes that become unstable at the ELM onset. We will discuss the two classes of models separately and then relate them to the experimental findings.

ELMs as Limit Cycle Oscillations

In Chapter 3 it was shown that, due to the hysteresis of the L-H power threshold, a limit cycle oscillation at the power threshold may occur. The original scope of the bifurcation model used in Chapter 3 to describe the dithering cycles was the explanation of type III ELMs in JFT2-M [Itoh et al., 1991]. It was concluded that the limit cycle oscillation found at the L-H threshold might be a description of type III ELMs. In a recent update of the theory [Itoh, 1994], it was shown that an increased outflux of particles, e.g. due to an MHD instability associated with a type I ELM, can trigger a back-transition to the L-mode followed by an L-H transition. While this model might correctly describe the sequence observed during compound ELMs, it does not give an explicit calculation for the type I ELM itself (the first increase in outflux was artificially prescribed in the model).

Several possible limit cycle oscillations are also found by other authors treating the temporal behaviour of the L-H transition. One example is the theory developed by Dia-

mond et al. [Diamond et al., 1994a]. Here, radially averaged equations for the temporal evolution of the amplitude of the turbulent fluctuations and the poloidal rotation are derived. The poloidal rotation is determined by the torque due to Reynold's stress, i.e. non-ambipolar anomalous transport and the dissipation due to magnetic pumping. The amplitude of the turbulent fluctuations is reduced by radial shear in the poloidal flow. In this system, it is found that at the L-H transition, dithering cycles may occur. If further physics is incorporated in the equations, other limit cycles can be identified. In [Diamond et al., 1994b], the ideal ballooning limit was heuristically incorporated to limit ∇p. In this case, periods of enhanced transport occur. Their repetition frequency increases with the energy flux through the system, thus, they are identified as type I ELMs. If instabilities associated with the rotation dynamics of the plasma edge, such as the Kelvin Helmholtz instability, are incorporated into the model, another limit cycle is found. Here, the edge pressure gradient may be below the ideal ballooning limit, but the rotational instability leads to increased transport. It is found that this instability becomes less frequent with increasing energy flux, hence, it is identified as a type III ELM.

Another system describing the dynamics of the L-H transition was developed by Sugama et al. [Sugama and Horton, 1995]. Here, three radially averaged equations are derived to describe the temporal evolution of the plasma edge pressure gradient, the amplitude of pressure driven resistive turbulence and the poloidal flow velocity. Again, a limit-cycle oscillation is found, not at the level of energy flux required for the L-H transition, but at higher energy flux. Consequently, this model should describe ELMs rather than dithering cycles. The authors conclude that their model describes type III ELMs, in contrast to the dithering cycles described by the model used by Itoh et al. [Itoh et al., 1991] and Zohm [Zohm et al., 1994a].

ELMs as MHD Instabilities

Several authors performed detailed MHD stability analyses of experimental and theoretically specified pressure and current profiles in order to decide whether they are unstable to a specific MHD instability. However, the usual linear stability analysis indicates if a mode will initially grow or not, but it cannot predict the actual effect of the mode on transport. This has to be inferred from nonlinear stability analysis which indicates at what level of perturbation a mode will saturate. Then, the effect of the saturated mode, or the combined effect of several interacting modes, on confinement has to be estimated. The nonlinear part of the MHD stability analysis is usually difficult to compute and thus, usually, theoretical estimates of the ELM effect on transport are not given.

The first MHD stability analysis to infer the ELM mechanism was performed by Gohil et al. [Gohil et al., 1988]. An infinite-n ideal ballooning analysis was done for DIII-D discharges exhibiting type I ELMs (at that time called 'giant ELMs'). It was found that the edge pressure gradient always builds up until the critical value $\alpha \approx \alpha_{crit}$ is reached. Then, a type I ELM occurs. This is a result of linear stability analysis; the authors do not propose an explicit model that describes how the ballooning mode itself leads to the

rapid transport of plasma across the separatrix.

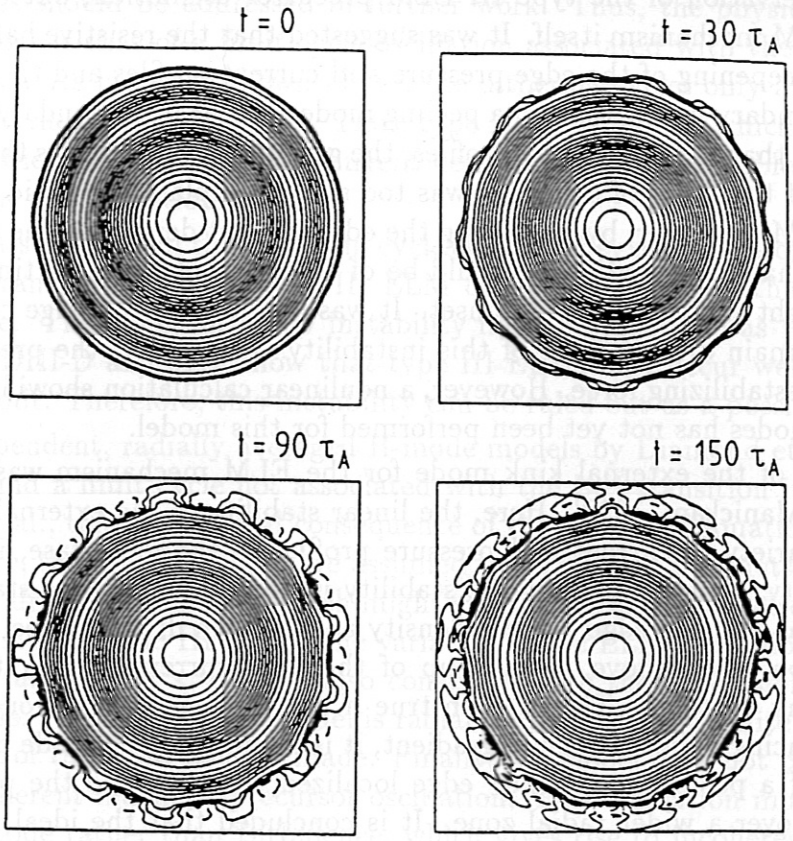

Figure 4.11: *Peeling mode in cylindrical geometry leading to a rapid loss of plasma across the boundary. The plot shows the temporal ecolution of the plasma pressure. This type of mode was suggested as the type III ELM mechanism on ASDEX.*

A different kind of analysis was done by Kerner et al. for ASDEX, i.e. for type III ELMs (reported in [The ASDEX Team, 1989]). Here, a nonlinear calculation in cylindrical geometry with a free boundary was performed. It was found that for sufficiently strong gradients of the edge current density and pressure, a nonlinear turbulent mixture of resistive interchange modes can couple to a kink instability, leading to rapid ($\approx 20\mu s$) destruction of the outer flux surfaces of the plasma ('peeling mode'). In this model, the driving force for the type III ELM is both the current and the pressure gradient in the edge. An example of a 'peeling off' of flux surfaces is shown in Fig. 4.11.

An extension of this type of model was given by Huysmans et al. for JET type III ELMs [Huysmans et al., 1992]. Here, a linear stability analysis with free boundary taking into account the effects of toroidicity and shape of the plasma cross-section was performed. Resistive ballooning modes (as an analogon to the resistive interchange in toroidal geometry) were found to be unstable for high mode numbers ($n \geq 10$). As these modes are

radially very localized and have a slow growth rate, it was concluded that they might explain the observation of the type III ELM precursor oscillation, but cannot explain the type III ELM mechanism itself. It was suggested that the resistive ballooning activity leads to a steepening of the edge pressure and current profiles and then couples to a lower n free boundary mode, to form a peeling mode. Linear free boundary tearing mode analysis showed that for JET model profiles, the growth rate (10^4 times the Alfven time, which itself is of the order of some μs) was too slow to explain the rapid growth at the onset of the ELM. However, by increasing the edge current density or the resistivity, the authors found that the growth time could be of the order of $10 - 100$ times the Alfven time, which might explain the ELM onset. It was shown that the edge current density gradient is the main driving force of this instability. For $n > 1$, the pressure gradient also enters as destabilizing force. However, a nonlinear calculation showing the coupling of the several modes has not yet been performed for this model.

A possible role of the external kink mode for the ELM mechanism was also stressed by Manickam [Manickam, 1992]. Here, the linear stability of the external kink mode is studied for a variety of current and pressure profiles in the ideal case, i.e. neglecting plasma resistivity. It is found that the stability is determined by the stabilizing effect of the edge shear and the edge current density as the main driving force. Thus, similar to the discussion given above, a build-up of the edge current density tends to drive the external kink unstable. This is even true if the analysis is done for a pressureless plasma. Introducing a finite pressure gradient, it is found that the mode can either have the structure of a peeling mode, i.e. edge localized, or couple to the plasma interior thus extending over a wider radial zone. It is concluded that the ideal kink might be a candidate for the type I ELM mechanism (called 'giant ELM' by the author). In particular, it is stated that the short growth times observed in the experiment ($\approx 10\mu$s) are consistent with the ideal external kink. However, no specific comparison to actual experimental profiles is done. Furthermore, the question how the enhanced transport of plasma during the ELM happens is not addressed.

Discussion

Based on the discussion of the experimental findings and the theoretical models, we now try to establish a physics picture of the different ELM phenomena. As was shown above, the ELM models generally give no quantitative description of how energy and particles are lost during the ELM; thus, a comparison to the experimentally determined transport properties of ELMs cannot be done. However, we can compare with the experimentally observed timescales, i.e. the rise time of the ELM, the duration and the behaviour of the ELM repetition frequency.

It was shown above, that time dependent models of the L-H transition can exhibit dithering cycles, i.e. series of L-H-L transitions. This is consistent with the experimental picture that dithering cycles are not primarily MHD events (no precursor, low fluctuation level). It was shown in Chapter 3 that for the model by Itoh et al., the repetition frequency of the dithering cycles is given by the diffusion time in the trans-

port barrier, yielding a timescale consistent with the experiment. The radially averaged model of Diamond et al. does not give quantitative predictions about the timescale of the cycle; this should be addressed in further work. Thus, the physical picture of the dithering cycles is that of a limit cycle oscillation associated with the hysteresis in the L-H transition. As has been shown above, the dithering cycles only affect temperature and density in the transport barrier. Thus, type III ELM models which require sufficient gradients of the edge pressure and current density are not applicable to the dithering cycles right at the transition.

Type III ELMs differ from the dithering cycles in that they exhibit strong MHD activity. The actual transport during a type III ELM can be much higher than in an intermediate L-phase. Therefore, an MHD instability must be identified as the type III ELM mechanism. DIII-D and JET show that type III ELMs may occur well below the ideal ballooning limit. Therefore, this instability can be ruled out as a possible candidate.

The time dependent, radially averaged H-mode models by Diamond et al. and Sugama et al. both find a limit cycle not associated with the L-H transition itself. In the case of Sugama et al., this is a natural consequence of the system of equations treated there. In this picture, the type III ELMs are assumed to correspond to bursts of resistive pressure gradient driven instabilities which might explain the high magnetic turbulence level observed during the type III ELM. The variation of the ELM repetition frequency with input power ($d\nu_{ELM}/dP < 0$) does also consistent with the experimental behaviour of type III ELMs. However, as the model is radially averaged, no definite statement about the timescale of the ELM itself is made. Finally, the model does not predict the occurrence of a coherent magnetic precursor oscillation. This oscillation must be interpreted as a single mode rather than turbulence, which gives rise to incoherent fluctuations of the magnetic field. Thus, at the moment, the model can only be regarded as an idealized description of a limit cycle representative for type III ELMs.

The same criticism holds for the type III ELM limit cycle presented by Diamond et al. It does not appear in the original system of equations describing the dynamics of the L-H transition, but is a consequence of the addition of terms describing a rotational instability such as the Kelvin-Helmholtz instability. While it is stated that the frequency of this repetitive instability decreases with heating power (which would be correct for type III ELMs), there is no statement about the actual timescales involved in the process. Also, a prediction of the spatial structure (precursor, fluctuation spectra etc.) of the instability is, at the moment, not given by the model.

The MHD model by Kerner et al. and Huysmans et al. yield more details about the MHD structure of the type III ELM. However, the identification of resistive ballooning modes with $n > 10$ as the ELM precursor as given by Huysmans et al. does not really match the experimental finding of a single mode with $n \leq 10$. The ELM mechanism itself, a peeling mode coupled to turbulent fluctuations, has been shown to have the right growth time of the order of several tens of μs. The role of the increased edge current density gradient required to drive the mode unstable may be consistent with the experimental observations: it is generally observed that during the H-mode, the internal

inductivity of the plasma decreases, indicating a broadening of the current density profile. In the future, an interesting contribution on this field can be made by stellarators, which exhibit only little edge current.

Both the MHD model and the limit cycle discussed by Sugama et al. interpret the ELM as a resistive phenomenon. This is consistent with the experimental fact that the edge temperature plays a crucial role in the type III ELM behaviour. All experimental evidence discussed above shows the tendency that a higher edge temperature stabilizes type III ELMs. This might also be the explanation for the frequency dependence of type III ELMs: the time interval between two ELMs is governed by the time it takes to build up the pressure and the current density gradients until the stability limit is reached. For a resistive instability, a rise in T due to a rise in heating power will shift the stability boundary to higher values, and increase the time it takes to develop the critical gradients. This is consistent with the observation that in JET, in a case where $T_e(a)$ is increased in steps due to the arrival of sawteeth heat pulses in the edge, at constant n and ∇n, the type III ELM frequency decreases with increasing $T_e(a)$ [Colton and Porte, 1993]. Obviuosly, the driving term due to the increase in ∇p when ∇T is increased is overcome by the stabilization due to the higher absolute value of T_e. This dependence would also explain the fact that the energy loss per type III ELM increases with decreasing frequency (see section 4.3): at higher T_e, a higher edge pressure gradient has been built up; the release of energy due to the ELM can therefore be higher. In addition, as was shown above (Fig. 4.8), the growth of the coherent precursor mode and the event initiating the ELM might be linked to a reconnection of magnetic flux, which is typical for a resistive phenomenon.

The situation is different for type I ELMs. Here, no precursor can be detected and the ELM is a rapid event. In addition, it happens at higher temperature so that it might be linked to an ideal MHD phenomenon. This is consistent with the ideal ballooning analysis which shows that, on JET and DIII-D, the edge pressure gradient reaches $\alpha \approx \alpha_{crit}$ prior to a type I ELM. This would also explain the frequency dependence of type I ELMs: contrary to type III ELMs, the stability boundary is fixed to a large extent by the geometry of the flux surfaces even if the absolute value of T varies. Thus, a higher heating power that leads to a faster buildup of the edge pressure gradient results in a higher ELM frequency. Note that, as the stability boundary does not vary with heating power, the edge pressure gradient does also not change significantly. This might explain that, contrary to type III ELMs, the energy loss per type I ELM does not vary significantly with heating power in cases with high ELM frequency. Another experimental evidence in favor of the ideal ballooning mode as a possible type I ELM mechanism is the fact that in cases where type I ELMs are suppressed, stability analysis often finds that the plasma edge has access to the second stable region of the ideal ballooning diagram. This is especially true for scenarios where strong shaping is applied and long ELM-free phases are observed at high heating power, such as in the VH mode in DIII-D [Osborne et al., 1995] or JET [Stork et al., 1994].

Somewhat conflicting with the interpretation of the type I ELM as an ideal ballooning

mode is the experimental observation that in DIII-D, the edge pressure gradient may reach the ideal ballooning limit and be at this value for several 100 ms without an ELM happening. In this sense, the condition that $\alpha \approx \alpha_{crit}$ may be necessary but not sufficient for a type I ELM. An example for this is the occurrence of type III ELMs even at the ballooning limit in small devices with circular cross-section, i.e. ASDEX and the ASDEX-like plasmas in DIII-D. Also, as was discussed above, no actual model exists that explains how high n ideal ballooning modes can enhance transport to the level observed during an ELM. One might therefore speculate that the ideal ballooning limit clamps the pressure gradient to $\alpha \approx \alpha_{crit}$, but the actual type I ELM happens through coupling of the ideal ballooning mode to another instability. An indication for the existence of another type of instability involved in the type I ELM may is also given by the power deposition pattern on the divertor plates during type I ELMs. As shown in Fig. 4.10, type I ELMs deposit a large energy flux on the inner target plate, whereas for ballooning modes, where the amplitude of the perturbation is high on the low field side, it might be expected that the power deposition is mostly on the outer target plate. This other instability might be of the type of an external kink as discussed by Manickam. If a lower n MHD instability is involved in the process, the 'peeling off' of flux surfaces might explain the very rapid transport during the ELM. Reconstructions of DIII-D equilibria prior to type I ELMs showed indications for a non-zero current density at the plasma edge [Zohm et al., 1995a], which is the main driver for an external kink. As was shown above, type I ELMs change the edge current density, thus potentially reducing the driving force of the edge current density gradient. However, the role of an ideal kink in type I ELMs has not yet been experimentally verified. An exception for this is the termination of the long ELM free phase in a VH-mode in DIII-D: there, the terminating event clearly has a low n component consistent with a kink instability [Osborne et al., 1995].

Thus, we propose the following physical picture of the different ELM phenomena:

- Dithering cycles: at the L-H transition, a limit cycle oscillation due to the hysteresis of the H-mode power threshold may occur. The edge pressure and current gradients are close to their L-mode values, hence, the dithering cycles are not specific MHD instabilities, but L-H-L sequences.

- Type III ELMs: after the L-H transition, steeper gradients of the edge pressure and current density develop due to the edge transport barrier. They are sources of free energy for resistive MHD instabilities as long as T_e in the edge is not too high. These instabilities are the type III ELMs, potentially a complex coupled MHD phenomenon consisting of high n resistive instabilities such as resistive ballooning modes and a low n kink-like free boundary instability that may rapidly enhance transport due to 'peeling off' of flux surfaces. An increase in edge temperature tends to shift the stability boundary for the resistive modes to higher values of pressure and current gradient, resulting in a decrease of the ELM repetition frequency with input power. For sufficient high temperature, resistive effects do not play a role any more and type III ELMs are suppressed.

- Type I ELMs: at high edge temperature, when type III ELMs are suppressed, the ideal ballooning mode limits the achievable edge pressure gradient to $\alpha \approx \alpha_{crit}$. If the ideal ballooning modes couple to a low n instability (potentially again a kink-like instability due to the high edge current density), a type I ELM develops. If, through plasma shaping, the plasma edge has access to the second stability regime of ballooning modes, the type I ELM is suppressed and the limit to the edge pressure gradient is given by the occurrence of low n MHD instabilities.

It should be noted that this physical picture can not yet be taken as a definite description of the complex nonlinear physics of the ELM; however, it matches the experimental observations and is based on the fundamental physics identified by MHD stability analysis. More work has to be done both on the experimental as on the theoretical side in order to validate the ideas expressed above.

Chapter 5

Summary and Conclusion

We have analysed the dynamic behaviour of the High Confinement mode (H-mode) of magnetically confined fusion plasmas. A physics picture of the dynamic phenomena occurring in the H-mode is established. It is based on the present theoretical understanding of the reduction of anomalous transport in the H-mode and describes well the experimental signatures of H-mode discharges in tokamaks.

The H-mode is characterized by its improved confinement with respect to L-mode conditions. The improvement is due to both a decrease of heat conductivity in the core plasma and the build-up of a transport barrier of width 1-3 cm within the plasma edge characterized by very low values of the particle diffusivity and heat conductivity. In this barrier, fluctuations are found to be reduced and the radial electric field shows a strong radial variation exhibiting large negative values in the barrier itself.

The transition from the L-mode to the H-mode happens when the heating power P exceeds a power threshold P_{thr}^{LH} and shows a hysteresis: the back transition into L-mode occurs at a lower heating power P_{thr}^{HL}. Thus, for $P_{thr}^{HL} \leq P \leq P_{thr}^{LH}$, the plasma can be either in the L- or in the H-mode, depending on the history of the discharge.

The basic H-mode model used in this work is the bifurcation theory of the poloidal rotation v_θ (or, equivalently, the radial electric field) of a magnetically confined toroidal plasma. The viscous force opposing poloidal rotation is due to 'magnetic pumping', i.e. a non-adiabatic compression and expansion of a plasma volume during the poloidal turn. At low v_θ, the viscous force increases with v_θ. On the other hand, the collisional damping decreases when the angular velocity of the rotation exceeds the typical collision frequency, i.e when v_θ exceeds the poloidal sound speed, which is of the order of the thermal ion velocity $v_{th,i}$ along field lines projected onto the poloidal direction. Thus, for $v_\theta > v_{th,i}\,\epsilon/q$, there exists a 'negative incremental viscosity'. For a given torque (e.g. due to non-ambipolar loss of ions), this may lead to a multivalued solution of v_θ in a certain range of plasma parameters.

The second idea entering into this H-mode model is the suppression of fluctuations by the sheared ploidal rotation. This is thought to be due to a decorrelation of communicating eddies due to the shear in the poloidal rotation. Although the model cannot quantita-

tively describe anomalous transport itself, it can used to describe the temporal behaviour of the L-H transition. The particle and energy transport equations together with the multivalued poloidal momentum balance form a system of equations describing a phase transition. It exhibits a so-called 'limit-cycle oscillation', i.e. an oscillatory solution at the transition from the L- to the H-state. This is compared with a detailed experimental investigation of the so-called 'dithering H-mode', i.e. a series of L-H-L transitions occuring when the heating power is gradually increased above the power necessary to initiate the first L-H transition. These transitions only affect the plasma edge and can be interpreted as repetitive formation and destruction of the edge transport barrier. Good agreement is found between the simple model and the experimental signatures; in particular, the timescale of the dithering cycles is identified as the time necessary to build up the steep edge gradients of temperature and density observed in the H-mode.

At higher heating power, other characteristic dynamic phenomena appear in H-mode discharges. These are the so-called ELMs (Edge Localized Modes). They differ from the dithering cycles in that they create large perturbations of the magnetic field and lead to rapid expulsion of particles and energy from the plasma edge. ELMs provide the possibility of stationary H-mode discharges with good energy confinement and particle density control. Therefore, ELMs are important for the operation of tokamak discharges in the H-mode. It is shown that, due to the different location of the particle and energy sources, ELMs lead to a stronger degradation of the confinement of particles than that of energy.

Taking into account the experimental evidence from several magnetic fusion experiments and the theoretical ELM models available at the moment, we arrive at a generalized classification of the different ELM phenomena. For historical reasons, they are called 'type III' and 'type I' ELMs (following the classification established in the DIII-D tokamak). They may be described as follows:

- Type III ELMs occur at comparatively low values of the plasma edge temperature. They are characterized by a decrease in repetition frequency with increasing energy flux through the plasma edge. They exhibit coherent magnetic precursor oscillations of toroidal mode number $n = 5 - 10$ and poloidal mode number $m = 10 - 15$ at a signal frequency of 50-200 kHz. The expelled energy per ELM increases with decreasing frequency. Depending on the edge temperature, this ELM type may appear when the normalized edge plasma pressure gradient α is in the region $0.3\,\alpha_{crit} \leq \alpha \leq \alpha_{crit}$ where α_{crit} is the critical pressure gradient given by the ideal ballooning limit. Type III ELMs are thought to be linked to a resistive instability, e.g. resistive ballooning modes, in combination with a global MHD instability such as a free-boundary mode (kink).

- Type I ELMs are characterized by their increase in repetition frequency with increasing energy flux through the plasma edge. At present, no coherent magnetic precursor oscillation has been found in the experiment. The expelled energy per ELM does not significantly vary with repetition frequency. Type I ELMs generally

occur when the pressure gradient at the plasma edge is close to the ideal ballooning limit. However, the criterion $\alpha \approx \alpha_{crit}$ seems to be necessary but not sufficient for the occurrence of a type I ELM. A plausible candidate for the type I ELM mechanism is therefore a combination of ideal ballooning modes coupled to a global ideal MHD instability as e.g. an ideal kink.

In any case, ELMs can be characterized as an MHD event of 0.5 - 1 ms duration. In addition, ELMs may trigger short L-phases lasting for 1-10 ms and ending with an L-H transition ('compound ELMs').

It has been mentioned above that this picture of the dynamic phenomena occurring in H-mode discharges is only a qualitative one. Further investigations remain to be done both in theory and in the experiment.

On the theoretical side, the description of the L-H transition is closely coupled to the understanding of anomalous transport itself. Here, no solid theory exists. The ongoing work on the understanding of anomalous transport will therefore also have impact on the L-H transition theories. On the problem of the poloidal spin-up, an improved quantitative calculation of the various non-ambipolar loss mechanisms that may initiate the rotation is needed. It should be stressed here, that ion orbit loss has not yet been proven to be the dominant mechanism.

The experimental investigation of the L-H transition still lacks the temporal resolution required to make a definitive statement about the causality of the build-up of the sheared poloidal rotation and the suppression of fluctuations. In addition, the experimental characterization of the turbulent processes responsible for anomalous transport and their suppression in the H-mode transport barrier can, at the moment, not give conclusive answers about the nature of the turbulence itself.

The description of ELMs is still qualitative. Obviously, a linear stability analysis of typical current and pressure profiles can give an indication about the unstable MHD modes. However, theoretical ELM studies have to face the need for non-linear calculations that actually describe the enhanced transport during the ELM. In general, this leads to a huge computational effort, but seems to be feasible in the future.

In the experiment, a better quantitative characterization of the stability boundaries of the different ELM types seems to be possible in the near future. This is due to the ongoing improvement in diagnostics that determine the profiles of temperature, particle density and current density with high spatial and temporal resolution. These profiles may serve as input for the theoretical analysis.

Finally, there is a lack of magnetic mode analysis during the ELM itself. The theoretical models described in this work predict global MHD modes of low toroidal mode number to be involved in the ELM mechanism itself. However, their characteristics may be difficult to extract from measurements of the fluctuating magnetic field due to the overlayed broad band turbulence from small scale fluctuations during the ELM. The identification of global MHD modes involved in the ELM process remains a challenge for further experimental investigations.

Appendix A

The Tokamak ASDEX Upgrade

A.1 The Tokamak Principle

The tokamak (from the Russian words for 'toroidal chamber for magnetic confinement') is an axisymmetric toroidal configuration in which the magnetic field lines helically cover nested toroidal surfaces, so-called magnetic surfaces or flux surfaces (see Fig. A.1). The latter term comes from the fact that the poloidal magnetic flux is a constant on the magnetic surfaces and can therefore be used to label the flux surfaces. Fig. A.1 shows an example.

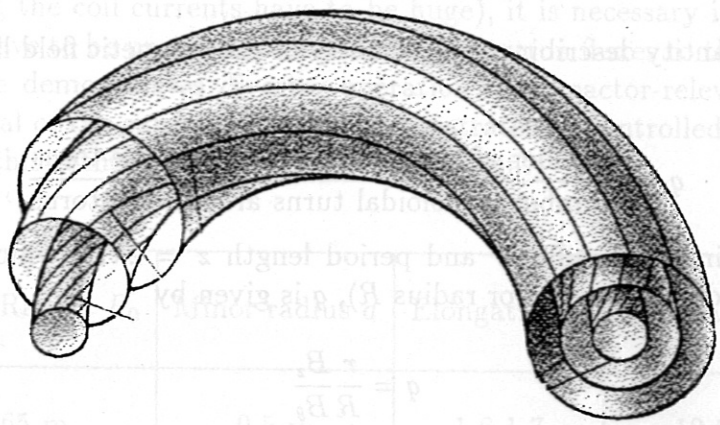

Figure A.1: *Toroidal geometry for magnetic confinement. The field lines helically wind around the torus to form magnetic surfaces.*

The toroidal field component is generated by coils; the poloidal component comes from a toroidal current I_p flowing in the plasma. This current is induced by the action of a transformer, normally a central solenoid. The current provides effective heating via the plasma resistance (OH = Ohmic Heating) for temperatures $T_e \leq 1-2$ keV. However, as

the plasma resistance decreases $\sim T^{-3/2}$, additional heating has to be applied in order to further increase the plasma temperature.
Poloidal field coils are used for controlling the plasma shape and position. Fig. A.2 gives a sketch of the tokamak principle.

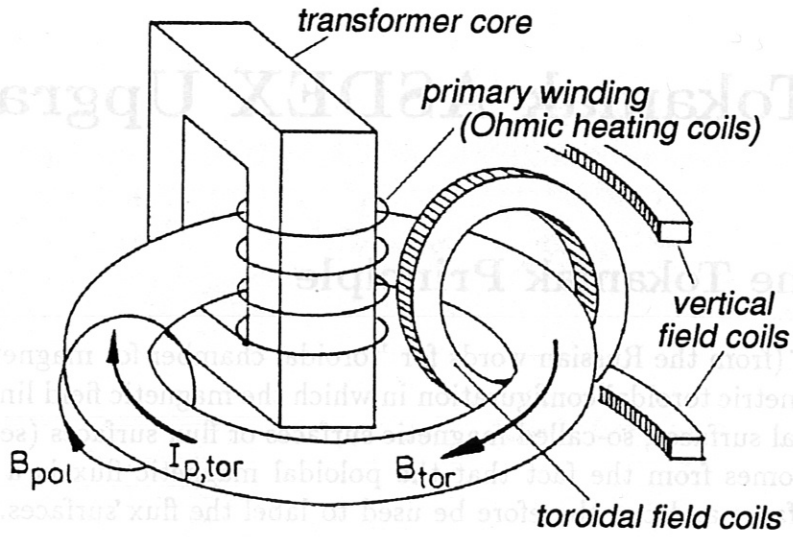

Figure A.2: *Sketch of the tokamak principle.*

An important quantity describing the geometry of the magnetic field lines is the number q defined by

$$q = \frac{\text{Number of toroidal turns around the torus}}{\text{Number of poloidal turns around the torus}} \tag{A.1}$$

In a periodic cylinder of radius r and period length $z = 2\pi R$ (which approximates a torus of minor radius r and major radius R), q is given by

$$q = \frac{r}{R}\frac{B_z}{B_\theta} \tag{A.2}$$

It can be shown that the configuration is unstable to the so-called *kink-instability* if $q < 1$ (therefore q is also called the safety factor). In tokamak experiments, it is found that, due to other instabilities, the safety factor at the edge, $q(a)$, has to be larger than 2. Typical tokamak experiments operate at $q(a) \approx 3$. Inserting this value and a typical aspect ratio of $R/r \approx 3$, we find that $B_z \approx 10 B_\theta$.
The poloidal cross-section of the tokamak does not necessarily have to be circular; it is found that the confinement can be more efficient if the cross-section is vertically elongated, i.e. the vertical minor radius b is bigger than the horizontal minor radius a. The elongation of a flux surface is then defined as

$$\kappa = \frac{b}{a} \tag{A.3}$$

A higher moment of non-circular shape is the triangularity δ. For a flux surface paramtrized in the poloidal cross-section R, z, it is defined by

$$\delta = \frac{R_{ave} - R_{zmax}}{a} \tag{A.4}$$

where $R_{ave} = 1/2(R_{max} - R_{min})$ is the average major radius and $a = 1/2(R_{max} - R_{min})$ the minor radius. R_{zmax} is the position where z has a maximum.

A.2 ASDEX Upgrade

As an example, we describe the tokamak experiment ASDEX Upgrade, on which many of the results discussed in the previous chapters were obtained. The acronym ASDEX stands for AXisymmetric Divertor EXperiment, due to the divertor configuration. The action of the divertor principle has already been discussed in Chapter 1. ASDEX Upgrade is the successor of the ASDEX experiment which was the first tokamak to demonstrate the successful operation of the divertor configuration, including the discovery of the H-mode operation regime. In ASDEX Upgrade, the divertor configuration is produced by poloidal field coils located outside the toroidal field coils, i.e. far away from the plasma. Although this configuration is not simple to control (due to the large distance between plasma and coils, the coil currents have to be huge), it is necessary in a future reactor, where the coils have to be protected from the large neutron fluxes to the first wall. Thus, ASDEX Upgrade demonstrates divertor operation in a reactor-relevant configuration. Another main goal of the experiment is to demonstrate the controlled exhaust of energy and particles in this rather open divertor configuration.

Major Radius R_0	Minor radius a	Elongation κ	Plasma Volume
1.65 m	0.5 m	1.6-1.7	12.5 m^3

Table A.1: Geometric parameters of a typical ASDEX Upgrade plasma.

Figure A.3 shows a poloidal cross-section of ASDEX Upgrade. It can be seen that the plasma cross-section is elongated. In order to form the divertor configuration, a separatrix with an X-point at the lower end of the cross-section is produced. This

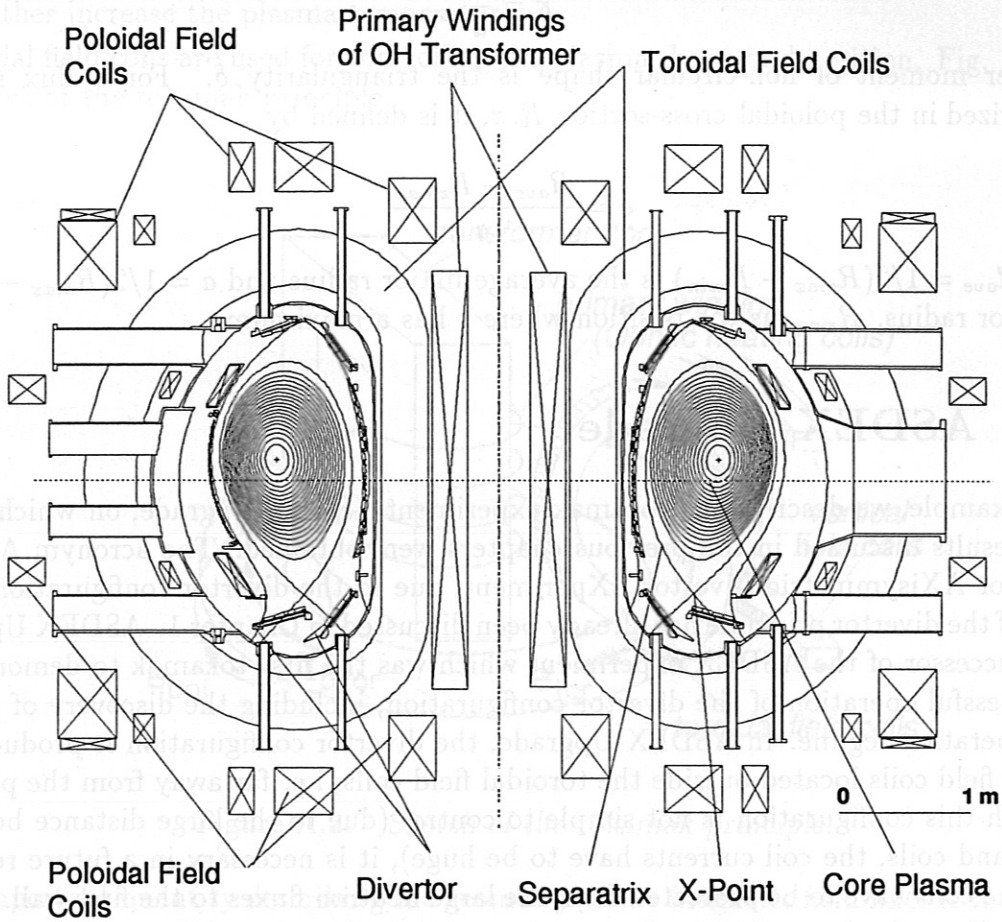

Figure A.3: *Poloidal cross-section of the ASDEX Upgrade tokamak.*

configuration is also called 'lower single-null'. It is the standard configuration in which ASDEX Upgrade is run. Typical geometric parameters are given in table A.1.

In this configuration, the plasma current and toroidal field may be changed to alter the edge safety factor $q(a)$. In addition, the particle density can be varied over a wide range. The temperatures obtained in these experiments depend on the operating regime as well as the heating power: In addition to the ohmic heating by the plasma current, which amounts to ≈ 1 MW, it is possible to heat the plasma with so-called additional heating. One possibility installed on ASDEX Upgrade is heating by radiofrequency waves: the ion cyclotron resonance heating (ICRH) method makes use of the resonance of waves and gyrating ions at the cyclotron frequency. The highest ICRH power obtained so far was 4 MW (1995). Another way to heat the plasma is the injection of highly energetic neutral deuterium (65 keV); this so-called neutral beam injection (NBI) routinely delivers a heating power of up to 10 MW. The range of plasma parameters realized in ASDEX Upgrade is given in table A.2.

Plasma Current I_p	Toroidal field B_t	Safety factor q	Central electron density $n_e(0)$	Central ion temp. $T_i(0)$	Energy conf. time τ_E
0.6-1.4 MA	1.0-3.0 T	2-7	$0.1 - 1.4 \times 10^{20}$ m^{-3}	0.8-3.5 keV	70-150 ms

Table A.2: Range of plasma parameters obtained in typical ASDEX Upgrade discharges.

In the discharge with the highest fusion product obtained so far (# 4930), the plasma parameters were $n_e(0) = 1.1 \times 10^{20}$ m^{-3}, $T_i(0) = 3.4$ keV and $\tau_E = 118$ ms, yielding $nT\tau_E = 4.4 \times 10^{22}$ m^{-3} eV s. These values were obtained in a stationary type I ELMy H-mode.

Appendix B

Neoclassical Transport Theory

In a magnetized plasma, the transport coefficients parallel and perpendicular to the magnetic field, e.g. the particle diffusivities $D_{\parallel}$ and $D_{\perp}$, are different. In general, the condition $D_{\parallel} \gg D_{\perp}$ holds, so that density and temperature are constant on flux surfaces but develop gradients in the perpendicular direction. Thus, the confinement properties of a magnetic configuration are governed by the perpendicular coefficients; we will therefore focus on those.

The simplest approach to calculate diffusion coefficients comes from the random-walk ansatz. Here, we assume that, due to collisions with other particles, a particle makes a step Δx perpendicular to the magnetic field after a time Δt. If the step can be done in either direction $\pm\Delta x$ with equal probability, the process is purely diffusive and the diffusion coefficient D is given by

$$D \approx \frac{\Delta x^2}{\Delta t} \tag{B.1}$$

In order to estimate D, we have to evaluate Δx and Δt. The latter is given by the inverse of the collision frequency ν_c. With appropriate averaging we obtain the following relations for a 90° scattering (made up of many small angle scatterings) of electrons off electrons (ee), electrons off ions (ei), ions off electrons (ie) and ions off ions (ii) (we assume a pure hydrogen plasma):

$$\nu_{ee} \approx \nu_{ei} \propto \frac{ne^4}{\sqrt{m_e} T_e^{3/2}} \tag{B.2}$$

$$\nu_{ie} = \left(\frac{m_e}{m_i}\right) \nu_{ee} \tag{B.3}$$

$$\nu_{ii} = \left(\frac{m_e}{m_i}\right)^{1/2} \left(\frac{T_e}{T_i}\right)^{3/2} \nu_{ee} \tag{B.4}$$

In the so-called classical approach to transport, we take Δx to be the Larmor radius ρ

$$\Delta x = \rho = \frac{\sqrt{2mkT}}{|q|\,B} \tag{B.5}$$

where q is the particle's charge. However, the location $\vec{R}$ of the guiding centre of the gyro-motion relative to the position of the particle itself is given by

$$\vec{R} = \frac{\vec{p} \times \vec{B}}{qB^2} \tag{B.6}$$

In a collision, momentum balance requires $\Delta\vec{p}_a = -\Delta\vec{p}_b$, where $\vec{p}$ is the particle momentum. Thus, for like-particle collisions, $\Delta\vec{R}_a = -\Delta\vec{R}_b$. Therefore, at each collision, the particles just change place so that like-particle collisions do not contribute to particle transport (note that heat can be transferred that way, because a hot particle may change place with a cold one).

The situation is different for electron-ion collisions. Here, $q_a = -q_b$ and therefore $\Delta\vec{p}_a = -\Delta\vec{p}_b$ leads to $\Delta\vec{R}_a = \Delta\vec{R}_b$. Thus diffusion is ambipolar, electrons and ions make a step of equal magnitude and direction per collision. The diffusion coefficient is then given by

$$D_{e,class} = \nu_{ei}\,\rho_e^2 = \nu_{ie}\,\rho_i^2 = D_{i,class} \tag{B.7}$$

For the thermal conductivities, similar arguments can be applied to show that the relation $\chi_i \approx (m_i/m_e)^{1/2}\chi_e \approx 40\chi_e$ for hydrogen should hold.

Experimentally determined diffusion coefficients in tokamaks are larger by a factor of $\approx 10^5$! Also, the electron heat conductivity is found to exceed that of the ions. Therefore, classical transport cannot be the dominating process in a tokamak plasma.

So far, we did not consider the effects of the toroidal geometry. This is the subject of the so-called *neoclassical* transport theory. The main differences to classical transport theory arise from two facts:

- Along a magnetic field line, $|B|$ is not constant; a particle moving along a field line sees a higher field on the inside of the torus and, for sufficient $v_\perp/v_\parallel$, may be reflected in this magnetic mirror. Therefore we have to distinguish between *trapped* and *passing* particles. It can be shown that the number density of trapped particles is given by $n_t/n = \sqrt{2\epsilon}$ where $\epsilon = r/R$ is the inverse aspect ratio of the flux surface. A simple result of this effect is that the electrical conductivity is lowered in neoclassical theory as trapped particles cannot contribute to the toroidal current.

- Due to the (vertical) ∇B drift (forces on the particle due to curvature and gradient of the magnetic field), the path of a particle deviates from the original flux surface. For a trapped particle, this means that the projection of its orbit in a poloidal plane is not a sector of a circle, but rather has a banana-like shape (see Fig. B.1). These orbits are known as *banana orbits*. One can show that the banana width is given by

$$r_B = \rho\sqrt{\epsilon}\frac{B_t}{B_\theta} = \rho_p\sqrt{\epsilon} \tag{B.8}$$

where the poloidal gyro-radius is denoted by ρ_p. It is bigger than ρ by the ratio $B_t/B_\theta \approx 10$.

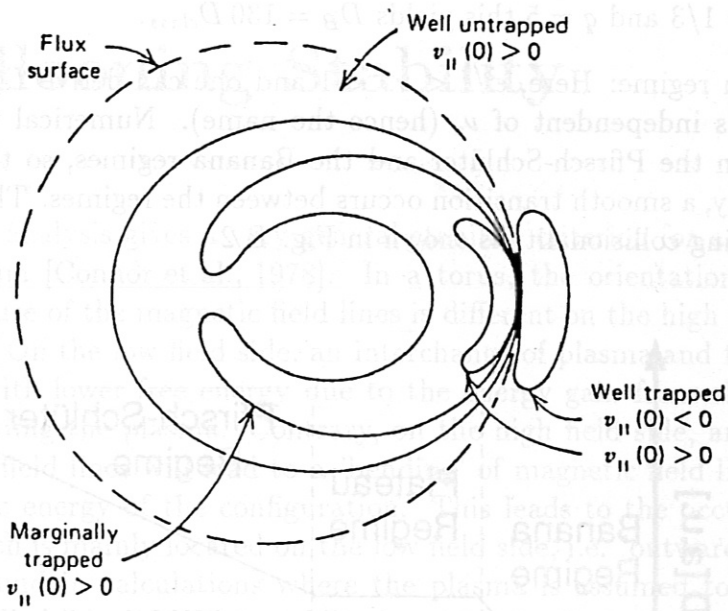

Figure B.1: *Banana orbits in a toroidal configuration.*

The existence of banana orbits leads to the so called *effective* collision frequency for trapped particles, $\nu_{eff} \approx \nu_c/(2\epsilon)$, where ν_c can be any of the collisionalities discussed above. Finally the so-called collisionality, i.e. the ratio $\nu_* = \nu_{eff}/\nu_t$, where ν_t is the inverse of the time a particle needs to transit the banana, determines whether the particle can complete a banana orbit between two collisions.

There are three different regimes of neoclassical transport:

- Collisional or Pfirsch-Schlüter regime: Here, $\nu_* > 1$, particles do not complete their banana orbits but are scattered before. In this case, D is evaluated to be

$$D_{PS} = q^2\,\rho^2\,\nu_c = q^2\,D_{class} \tag{B.9}$$

  where q is the safety factor defined by Eqn. (A.1). As we have seen, q typically ranges between 2 and 5, so transport is strongly increased.

- Banana regime: Here, $\nu_* < \epsilon^{3/2}$, particles follow the banana orbit several times before they are scattered. We can apply the random walk argument for the $\sqrt{2\epsilon}$ trapped particles with step size r_B and typical time interval $1/\nu_{eff}$:

$$D_B \propto \sqrt{2\epsilon}\, r_B^2\, \nu_{eff} = \frac{\rho^2 q^2}{\epsilon^{3/2}} \nu_c = \frac{q^2}{\epsilon^{3/2}} D_{class} \tag{B.10}$$

  For $\epsilon = 1/3$ and $q = 5$ this yields $D_B = 130\, D_{class}$.

- Plateau regime: Here, $\epsilon^{3/2} < \nu^* < 1$ and one can derive $D_{Pl} \approx v_{th}\, r_L^2\, q/R$. This result is independent of ν_c (hence the name). Numerical values for D_{Pl} are in between the Pfirsch-Schlüter and the Banana regimes, so that, with rising collisionality, a smooth transition occurs between the regimes. The variation of D with increasing collisionality is shown in Fig. B.2

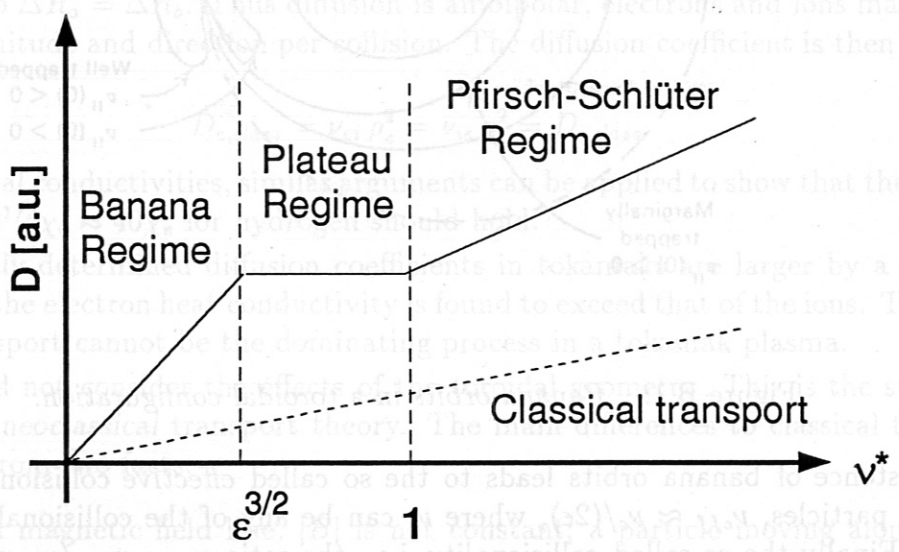

Figure B.2: *Variation of the particle diffusivity D in the different neoclassical regimes.*

These neoclassical terms have to be added to the classical terms. However, they completely dominate the latter. We have seen that, due to neoclassical effects, transport coefficients can be increased by two orders of magnitude, nevertheless, they still cannot explain the experimental observations, especially for the electron heat conductivity. Today, theory tries to explain this so-called *anomalous transport* by nonlinear fluid turbulence models.

Appendix C

Ideal Ballooning Stability

The ideal ballooning analysis gives a very general stability criterion for a magnetically confined fusion plasma [Connor et al., 1978]. In a torus, the orientation of ∇p with respect to the curvature of the magnetic field lines is different on the high field side and on the low field side. On the low field side, an interchange of plasma and field lines can lead to a situation with lower free energy due to the energy gain from shortening the field lines and expanding the plasma. Contrary, on the high field side, an interchange between plasma and field lines will lead to a 'bending' of magnetic field lines and thus increase the magnetic energy of the configuration. This leads to the occurrence of an MHD instability which is mainly located on the low field side, i.e. 'outward ballooning'. This instability is found in calculations where the plasma is assumed to be perfectly conducting (i.e. so-called 'ideal' MHD instability) and for the limit that the modes have no radial extent. In a Fourier decomposition of the perturbation along the toroidal coordinate ϕ, i.e. $\tilde{B} \sim \sin(n\phi)$, this means that $n \to \infty$. Therefore, this type of stability calculation is also called 'infinite n ideal ballooning stability analysis'.

In ballooning mode analysis (see e.g. [Lortz and Nührenberg, 1978]), it is found that the interchange of field lines and plasma on the low field side can be suppressed by the shear of the magnetic field, i.e. a variation of the safety factor q defined by Eqn. (A.1) between neighbouring flux surfaces. It is therefore convenient to express ballooning stability in a diagram that relates the pressure and the shear, i.e.

$$\alpha = \frac{2\mu_0 R_0 q^2}{B_t^2} \nabla p \tag{C.1}$$

where the kinetic pressure gradient has been normalized to the pressure gradient associated with the toroidal magnetic field and

$$s = \frac{r}{q}\frac{dq}{dr} \tag{C.2}$$

the normalized shear.

A result of such a calculation is shown in Fig. C.1. For a given s, the pressure gradient

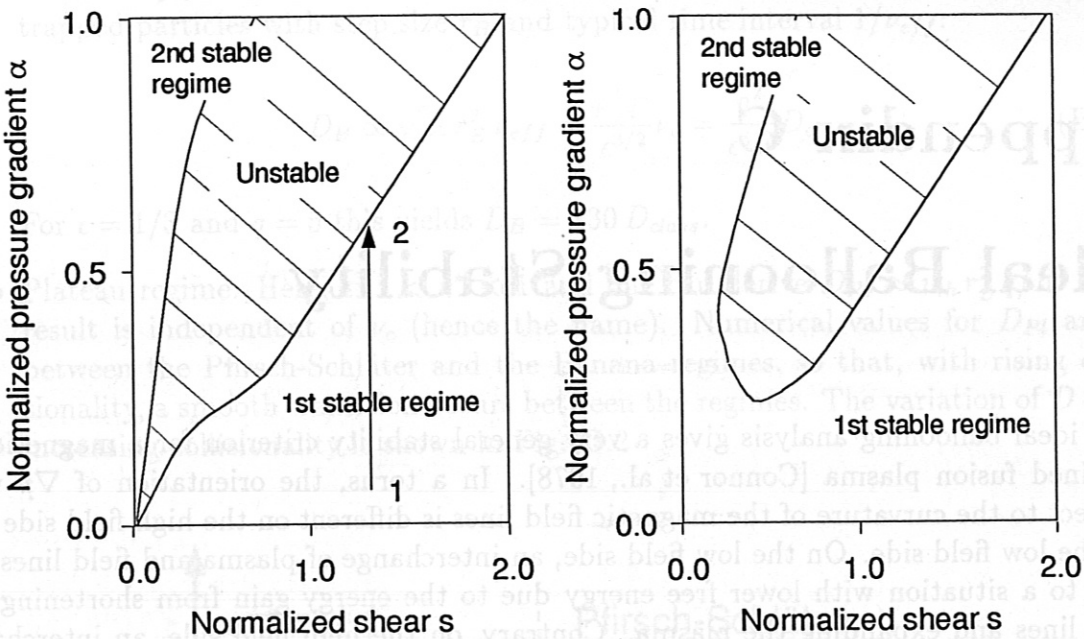

Figure C.1: *Ideal ballooning stability diagram for a tokamak with circular cross-section (left) and for elongated and triangular cross-section (right).*

α can be increased until the stability boundary indicated in the figure is reached as indicated by the path $1 \rightarrow 2$ in the left diagram of Fig. C.1. The value of α describing the stability boundary is often called the critical pressure gradient α_{crit}. It can be seen that with increasing shear, the value of α_{crit} rises. For sufficiently large shear ($s \geq 0.5$), the stability boundary can be approximated by a straight line

$$\alpha_{crit} \approx 0.6\, s \tag{C.3}$$

The left diagram diagram has been calculated for a plasma with circular cross-section. It can be seen that, for low shear, another stable region, which is not accessible in the left diagram, exists. This is the so-called '2nd stable regime' (the case discussed above is normally referred to as '1st stable regime'). Calculations show that in a plasma with non-circular cross-section, an access to the 2nd stable regime may be possible at low shear; this is sketched in the right diagram of Fig. C.1. A discussion of the effect of elongation and triangularity of the cross-section on the access to the 2nd stable regime ca be found in [Ozeki et al., 1990].

The ideal ballooning limit sets a limit to the achievable value of β_t, the plasma pressure normalized to the pressure associated with the magnetic field:

$$\beta = \frac{2\mu_0 \langle p \rangle}{B^2} \tag{C.4}$$

where the brackets denote the average over the whole plasma. This can be seen by integrating Eqn. (C.4) by parts, re-writing it in terms of α and using Eqn. C.3 to express α as function of s:

$$\beta = \frac{4\mu_0 \int_0^a p(r) r \, dr}{a^2 B^2} = -\frac{\int_0^a \alpha r^2/q^2 \, dr}{Ra^2} = 0.3 \frac{1}{a^2 R} \int_0^a \frac{d}{dr}\left(\frac{1}{q^2}\right) r^3 \, dr \qquad \text{(C.5)}$$

This formulation again reflects the fact that the available shear limits the achievable pressure. In principle, Eqn. (C.5) can be used to derive an arbitrarly shaped q-profile optimized in order to obtain a maximum of β. However, as mentioned before (see Appendix A), stability against the internal kink instability sets a lower limit to the value of the safety factor, i.e. $q \geq 1$ everywhere in the plasma. An optimization of Eqn. (C.5) with the constraint $q \geq 1$ and $q(a) \geq 2$ yields [Wesson and Sykes, 1985]

$$\beta_{max} = g \frac{I}{aB_t} \qquad [\%, \mathrm{MA}, \mathrm{m}, \mathrm{T}] \qquad \text{(C.6)}$$

This result, first obtained by Troyon et al. [Troyon et al., 1984], is also known as the β-limit or Troyon-limit and is well confirmed by experimental results. Numerical values of the constant are found to be $g \geq 3$. In the experiment, other MHD instabilities such as the external kink may lead to lower values of β_{max}.

Appendix D

Glossary

Anomalous transport: Transport of heat and particles in excess of the neoclassical transport. It is presumably caused by the effects of plasma turbulence and field line stochasticity.

Aspect ratio: Ratio of major and minor radius of a torus.

Ballooning mode: Pressure driven MHD instability that has a high amplitude on the low field side of the torus ('outward ballooning').

D_α-light: Light emitted by neutral Deuterium atoms (Balmer α spectral line); D_α-light emitted in the divertor yields a rough measure of the particle flux out of the plasma.

Dithering H-mode: Series of repetitive L-H-L transitions.

Divertor: Magnetic configuration that leads the open field lines outside the separatrix onto target plates some distance away from the core plasma.

ECE: Electron Cyclotron Emission. The intensity of the cyclotron radiation emitted by gyrating electrons can be used to infer T_e.

ELM: Edge Localized Mode, instability typical for the H-mode that expells heat and particles from the plasma edge on a fast (≤ 1 ms) timescale.

Elongation: Vertical elongation of a magnetic surface, defined as the ratio of vertical to horizontal extension of the poloidal cross-section of the surface.

Favorable drift direction: Direction of B_t, for which the drift of ions due to curvature and gradient of the magnetic field is directed towards the X-point. For the favorable drift direction, the H-mode power threshold is lower than for the unfavorable direction, in which B is in the opposite direction.

Flux surface: Toroidal surface mapped by magnetic field lines. Nested flux surfaces are though to be essential for toroidal confined plasmas. On this surface, the poloidal and toroidal magnetic fluxes are constant.

ICRH: Ion Cyclotron Resonance Heating, plasma heating by radio frequency waves using the ion cyclotron resonance.

Ideal MHD: MHD description of the plasma in the case of negligible resistivity. Here, the topology of the flux surcfaces cannot change.

Kink mode: MHD instability driven by the plasma current. It leads to a kink-like bending of the initially axisymmetric flux surface.

Magnetic confinement: Containment of a plasma in a magnetic field; due to the gyromotion, the particles are tied to the field lines but may move freely along them.

Magnetic pumping: Dissipation of energy due to non-adiabatic compression and expansion of a plasma volume, e.g. during poloidal rotation of a plasma in a torus.

Magnetic shear: Radial variation of the safety factor; in a sheared magnetic field, field lines on neighbouring flux surfaces have different angles with respect to a fixed direction.

Magnetic surface: Same as flux surface.

MHD: Magneto Hydro Dynamic description of a plasma. A set of fluid equations which, together with Maxwell's equations, describes the plasma as a neutral, electrically conducting fluid imbedded in a magnetic field.

MHD mode: Linear instability described by the MHD equations; it leads to a displacement of fluid elements.

Mirnov coil: Magnetic pick-up coil installed inside the vacuum vessel of a magnetic fusion experiment. It measures the fluctuating magnetic field.

Mode number: In a torus, MHD modes may be Fourier-decomposed in the toroidal and the poloidal angle. Each harmonic is characterized by a poloidal mode number m and a toroidal mode number n.

NBI: Neutral Beam Injection, plasma heating by the injection of fast neutral particles that become ionized in the plasma and heat it by collisions.

Neoclassical transport: Transport theory based on binary collisions in a toroidal plasma. Neoclassical transport is dominated by processes specific to the toroidal geometry.

Peeling mode: Edge localized MHD instability that 'peels off' the outermost flux surfaces.

Poloidal direction: The direction the short way around the torus.

Resistive MHD: MHD description of a plasma taking into account the effects of resistivity. In resistive MHD, the topology of the flux surfaces may change.

Safety factor: The number of toroidal turns of a field line until it completes one poloidal turn.

Separatrix: The flux surface separating closed magnetic surfaces and open field lines. A separatrix has one or more X-points.

Shear viscosity: Viscous damping of the differential rotation of neighbouring flux surfaces.

Stellarator: Toroidal confinement device in which the total magnetic field is produced by external coils. The magnetic configuration necessarily is non-axisymmetric.

SOL: Scrape Off Layer, the flux surfaces outside the last closed flux surface. Magnetic field lines in the SOL are connected with a material wall.

Target plate: Plate in the divertor where the magnetic field lines intersect the wall. Here, the energy and particle fluxes across the separatrix arrive.

Tokamak: Axisymmetric toroidal confinement device in which the toroidal magnetic field is produced by external coils and the poloidal field comes from a toroidal plasma current.

Toroidal direction: The direction the long way around the torus.

Triangularity: A number describing the deviation of a flux surface from a circle to a triangle. It is $\pm$ 1 for an up-down symmetric triangle and 0 for a circle.

X-point: A point on the poloidal cross-section of a flux surface where the poloidal field is zero. On a flux surface with an X-point, the field lines come arbitrarily close to the X-point but never reach it.

Bibliography

[Ali-Arshad et al., 1992] Ali-Arshad, S., Campbell, D., Colton, A., Cripwell, P., de Kock, L., Kramer, G. J., Nave, M. F. F., and Neill, G. F. (1992). ELM precursors in JET. *Controlled Fusion and Plasma Physics, Proceedings of the 19th European Conference, Innsbruck*, I:227–230.

[Bessenrodt-Weberpals et al., 1993] Bessenrodt-Weberpals, M. et al. (1993). The isotope effect in ASDEX. *Nuclear Fusion*, 33(8):1205–1238.

[Biglari et al., 1990] Biglari, H., Diamond, P. H., and Terry, P. W. (1990). Influence of Sheared Poloidal Rotation on Edge Turbulence. *Phys. Fluids B*, 2(1):1–3.

[Burrell et al., 1989] Burrell, K. H., Allen, S. L., Bramson, G., Brooks, N. H., Callis, R. W., Carlstrom, T. N., Chu, M. S., Colleraine, A. P., Content, D., et al. (1989). Confinement physics of H-mode discharges in DIII-D. *Plasma Physics and Controlled Fusion*, 31(10):1649–1664.

[Campbell et al., 1994] Campbell, D. et al. (1994). H-modes under steady state conditions in JET. *Plasma Physics and Controlled Fusion*, 36:A255–A260.

[Colton and Porte, 1993] Colton, A. and Porte, L. (1993). Correlation between ELMs and the edge plasma profiles during the L-H transition in JET. *Controlled Fusion and Plasma Physics, Proceedings of the 20th European Conference, Lisbon*, I:11–14.

[Connor et al., 1978] Connor, J. W. et al. (1978). Shear, Periodicity, and Plasma Ballooning Modes. *Physical Review Letters*, 40(6).

[Cordey et al., 1994] Cordey, J. G. et al. (1994). The time behaviour of the thermal conductivity during the L-H and H-L transitions in JET. *Plasma Physics and Controlled Fusion*, 36:A267–A272.

[Coster et al., 1994] Coster, D. P. et al. (1994). B2-EIRENE modelling of ELMs on ASDEX Upgrade. *Controlled Fusion and Plasma Physics, Proceedings of the 21st European Conference, Montpellier*, I:846–849.

[De Blank, 1995] De Blank, H. J. (1995). *Priv. Comm.*

[de Blank et al., 1991] de Blank, H. J., Nave, M. F. F., Kerner, W., and Huysmans, G. T. A. (1991). Resistive ballooning mode ananlysis for Edge Localized Modes in JET discharges. *JET-R(91)08.*

[de Blank and Zohm, 1994] de Blank, H. J. and Zohm, H. (1994). Test of theory of the L-H transition in ASDEX Upgrade discharges. *Controlled Fusion and Plasma Physics, Proceedings of the 21st European Conference, Montpellier*, II:632–635.

[Diamond et al., 1994a] Diamond, P. H. et al. (1994a). Dynamics of the L-H transition, VH ode Evolution, Edge Localized Modes and R.F. Driven Confinement Control in Tokamaks. *15th International Conference on Plasma Physics and Controlled Nuclear Fusion Research, Sevilla, IAEA-CN-60 /D-2-II-6.*

[Diamond and Kim, 1991] Diamond, P. H. and Kim, Y.-B. (1991). Theory of mean poloidal flow generation by turbulence. *Phys. Fluids B*, 3(7):1626–1633.

[Diamond et al., 1994b] Diamond, P. H., Liang, Y. M., Carreras, B. A., and Terry, P. W. (1994b). Self-Regulationg Shear Flow Turbulence: A Paradigm for the L-H Transition. *Physical Review Letters*, 72(16):2565–2568.

[Doyle et al., 1991] Doyle, E. J., Groebner, R. J., Burrell, K. H., Gohil, P., Lehecka, T., Luhmann, N. C., Matsumoto, H., Osborne, T. H., Peebles, W. A., and Philipona, R. (1991). Modifications in Turbulence and Edge Electric Fields at the L-H transition in the DIII-D Tokamak. *Phys. Fluids B*, 3(8).

[Erckmann et al., 1993] Erckmann, V. et al. (1993). The H-mode of the W 7-AS Stellarator. *Physical Review Letters*, 70(14):2086–2089.

[Galeev and Sagdeev, 1968] Galeev, A. and Sagdeev, R. (1968). Transport Phenomena in a Collisionless Plasma in a Toroidal Magnetic System. *Sov. Phys. JETP*, 26(1):233–240.

[Gohil et al., 1988] Gohil, P., Ali Mahdavi, M., Lao, L., Burrell, K. H., Chu, M. S., De Boo, J. C., Hsieh, C. L., Ohyabu, N., Snider, R. T., Stambaugh, R. D., and Stockdale, R. E. (1988). Study of Giant Edge-Localized Modes in DIII-D and Comparison with Ballooning Theory. *Physical Review Letters*, 61(14).

[Gohil et al., 1994] Gohil, P., Burrell, K. H., Doyle, E. J., Groebner, R. J., Kim, J., and Serayderian, R. P. (1994). The phenomenology of the L-H transition in the DIII-D tokamak. *Nuclear Fusion*, 35(8):1057–1068.

[Groebner, 1993] Groebner, R. J. (1993). An emerging understanding of H-mode discharges in tokamaks. *Phys. Fluids B*, 5(7):2343–2354.

[H-mode Database Working Group, presented by O. Kardaun, 1992] H-mode Database Working Group, presented by O. Kardaun (1992). ITER: Analysis of the H-mode confinement and threshold databases. *14th International Conference on Plasma Physics and Controlled Nuclear Fusion Research, Würzburg, IAEA-CN-36 / IF-1-3.*

[Herrmann et al., 1995] Herrmann, A., Junker, W., Günther, K., Bosch, S., Kaufmann, M., Neuhauser, J., Pautasso, G., Richter, T., Schneider, W., and ASDEX Upgrade-Team (1995). Energy flux to the ASDEX Upgrade divertor plates determined by thermography and calorimetry. *Plasma Physics and Controlled Fusion*, 37(1):17–29.

[Hill et al., 1992] Hill, D. N., Futch, A., Leonard, A. W., Mahdavi, M. A., Petrie, T. W., Buchenauer, D., Campbell, R., Cuthbertson, J. W., Watkins, J., and Moyer, R. (1992). The effect of ELMs on edge plasma scaling in DIII-D. *J. Nucl. Mater.*, 196-198:204–209.

[Hillis et al., 1994] Hillis, D. et al. (1994). Helium transport and exhaust studies of H-mode discharges in the DIII-D tokamak. *Plasma Physics and Controlled Fusion*, 36:A171–A177.

[Hinton and Chu, 1985] Hinton, F. and Chu, M. (1985). Neoclassical Ion Transport through the Separatrix in Divertor Tokamaks. *Nuclear Fusion*, 25(3).

[Hinton et al., 1994] Hinton, F. L., Kim, J., Kim, Y.-B., Brizard, A., and Burrell, K. H. (1994). Poloidal Rotation near the Edge of a Tokamak Plasma in H-mode. *Physical Review Letters*, 72(8):1216–1219.

[Hugill, 1994] Hugill, J. (1994). Rotation and improved confinement modes. *Plasma Physics and Controlled Fusion*, 36:B173–B180.

[Huysmans et al., 1992] Huysmans, G. T. A., de Blank, H. J., Kerner, W., Goedbloed, J. P., and Nave, M. F. F. (1992). MHD Stability Models of Edge Localized Modes in JET Discharges. *Controlled Fusion and Plasma Physics, Proceedings of the 19th European Conference, Innsbruck*, I:247–250.

[ITER H-mode Database Working Group, 1994] ITER H-mode Database Working Group (1994). ITER H-mode confinement database update. *Nuclear Fusion*, 34(1):131–167.

[Itoh, 1994] Itoh, K. (1994). Theoretical Progress on H-mode Physics. *Plasma Physics and Controlled Fusion*, 36:A307–A318.

[Itoh and Itoh, 1988] Itoh, S. and Itoh, K. (1988). Model of L- to H-mode Transition in Tokamak. *Physical Review Letters*, 60(22):2276–2279.

[Itoh and Itoh, 1989] Itoh, S. and Itoh, K. (1989). Model of the H-mode in Tokamaks. *Nuclear Fusion*, 29(6):1031–1045.

[Itoh et al., 1991] Itoh, S., Itoh, K., Fukuyama, A., and Miura, Y. (1991). Edge Localized Mode Activity as a Limit Cycle in Tokamak Plasmas. *Physical Review Letters*, 67(18):2485–2488.

[Jackson et al., 1991] Jackson, G. L. et al. (1991). Regime of Very High Confinement the Boronized DIII-D Tokamak. *Physical Review Letters*, 67(22):3098–3101.

[Kallenbach et al., 1990] Kallenbach, A., Mayer, H. M., Fussmann, G., Büchse, R., Gruber, O., Klüber, O., Mertens, V., Vollmer, O., and Zohm, H. (1990). Improvement of angular momentum confinement with density peaking on ASDEX. *Nuclear Fusion*, 30(4):645–656.

[Kallenbach et al., 1991] Kallenbach, A., Mayer, H. M., Fussmann, G., Mertens, V., Stroth, U., and Vollmer, O. (1991). Characterization of the angular momentum transport in ASDEX. *Plasma Physics and Controlled Fusion*, 33(6):595–605.

[Kaufmann et al., 1994] Kaufmann, M. et al. (1994). Divertor Characteristics During High Density H-mode Discharges in ASDEX Upgrade. *15th International Conference on Plasma Physics and Controlled Nuclear Fusion Research, Sevilla, IAEA-CN-60 /A4-I-1.*

[Köppendörfer et al., 1992] Köppendörfer, W., Andelfinger, C., Ballico, M., Becker, W., Behler, K., Bessenrodt-Weberpals, M., Bosch, H.-S., Braun, F., Büchl, K., et al. (1992). Results of the first operational phase of ASDEX Upgrade. *14th International Conference on Plasma Physics and Controlled Nuclear Fusion Research, Würzburg, IAEA-CN-56 / A-2-3.*

[Lackner et al., 1994] Lackner, K. et al. (1994). Recent results from divertor operation in ASDEX Upgrade. *Plasma Physics and Controlled Fusion*, 36(12B):B79–B92.

[Leonard et al., 1991] Leonard, A. W. et al. (1991). Effects of applied error fields on the H-mode power threshold in JFT-2M. *Nuclear Fusion*, 31(8):1511–1518.

[Lortz and Nührenberg, 1978] Lortz, D. and Nührenberg, J. (1978). Ballooning Stability Boundaries for the Large-Aspect-Ratio Tokamak. *Phys. Lett. A*, 68A(1).

[Manickam, 1992] Manickam, J. (1992). The role of edge current density on kink mode stability and its implication for magnetohydrodynamic activity associated with edge localized modes. *Phys. Fluids B*, 4(7).

[Mertens et al., 1990] Mertens, V., Bessenrodt-Weberpals, M., Dodel, G., et al. (1990). Physics of enhanced confinement with peaked and broad density profiles. *Plasma Physics and Controlled Fusion*, 32(11):965–981.

[Miura et al., 1991] Miura, Y. et al. (1991). Studies of improved confinement on JFT-2M. *13th Int. Conf. on Plasma Physics and Controlled Nuclear Fusion Research, Washington*, (paper IAEA-CN-53/A-IV-6).

[Neuhauser et al., 1992] Neuhauser, J. et al. (1992). The physics of power exhaust from toroidal magnetoplasmas. *Plasma Physics and Controlled Fusion*, 34(13):2015–2022.

[Osborne et al., 1995] Osborne, T. H. et al. (1995). Confinement and stability of VH-Mode discharges in the DIII-D tokamak. *Nuclear Fusion*, 35(1):23–38.

[Ozeki et al., 1990] Ozeki, T., Chu, M. S., Lao, L. L., Taylor, T. S., Chance, M. S., Kinoshita, S., Burrell, K. H., and Stambaugh, R. D. (1990). Plasma Shaping, Edge Ballooning Stability and ELM behaviour in DIII-D. *Nuclear Fusion*, 30(8):1425–1432.

[Parail et al., 1994] Parail, V. et al. (1994). The Physics of L- and H-mode Confinement in JET. *15th International Conference on Plasma Physics and Controlled Nuclear Fusion Research, Sevilla, IAEA-CN-60 /A-2-II-3.*

[Pogutse et al., 1994] Pogutse, A., Kerner, W., Gribkov, V. abd Berzdenkov, S., and Osipenko, M. (1994). The resistive interchange convection in the edge of tokamak plasmas. *Plasma Physics and Controlled Fusion*, 36(12):1963–1985.

[Reiter et al., 1990] Reiter, D., Wolf, G., and Kever, H. (1990). Burn Condition, Helium Particle Confinement and Exhaust Efficiency. *Nuclear Fusion*, 30(10).

[Ryter et al., 1994] Ryter, F. et al. (1994). H-mode results in ASDEX-Upgrade. *Plasma Physics and Controlled Fusion*, 36:A99–A104.

[Ryter et al., 1993] Ryter, F., Gruber, O., Büchl, K., Fuchs, J. C., Gehre, O., Murmann, H., Noterdaeme, J.-M., and Zohm, H. (1993). Ohmic H-mode and H-mode Power Threshold in ASDEX-Upgrade. *Controlled Fusion and Plasma Physics, Proceedings of the 20th European Conference, Lisbon*, I:23–26.

[Sakai et al., 1993] Sakai, O., Yasaka, Y., and Itatani, R. (1993). High Radial Confinement Mode Induced by dc Limiter Biasing in the HIEI Tandem Mirror. *Physical Review Letters*, 70(26):4071–4074.

[Schissel et al., 1992] Schissel, D. P., Osborne, T. H., Carlstrom, T. N., and Zohm, H. (1992). A Quantitive Analysis of the Effect of ELMs on H-mode Thermal Confinement in DIII-D. *Controlled Fusion and Plasma Physics, Proceedings of the 19th European Conference, Innsbruck*, I:235–238.

[Shaing, 1992] Shaing, K. C. (1992). Poloidal magnetic field dependence of the edge electric field layer width in the H mode in tokamaks. *Phys. Fluids B*, 4(2).

[Shaing and Crume, 1989] Shaing, K. C. and Crume, E. C. (1989). Bifurcation Theory of Poloidal Rotation in Tokamaks: A Model for the L-H Transition. *Physical Review Letters*, 63(21):2369–2372.

[Stork et al., 1994] Stork, D. et al. (1994). Overview of High Performance H-modes in JET. *Plasma Physics and Controlled Fusion*, 36:A23–A38.

[Stringer, 1993] Stringer, T. (1993). An explanation of the L to H transition induced by applied radial voltage. *Nuclear Fusion*, 33(9).

[Sugama and Horton, 1995] Sugama, H. and Horton, W. (1995). L-H Confinement Mode Dynamics in three-dimensional State Space. *Plasma Physics and Controlled Fusion*, 37(3):345–362.

[The ASDEX Team, 1989] The ASDEX Team (1989). The H-mode of ASDEX. *Nuclear Fusion*, 29(11):1959–2040.

[Todd and COMPASS Team, 1993] Todd, T. N. and COMPASS Team (1993). MHD Control and ECCD in COMPASS-D. *Plasma Physics and Controlled Fusion*, 35(12):B231–B240.

[Troyon et al., 1984] Troyon, F., Gruber, R., Saurenman, H., Semenzato, S., and Succi, S. (1984). MHD Limits to Plasma Confinement. *Plasma Physics and Controlled Fusion*, 26(1A).

[Valovic et al., 1994] Valovic, M. et al. (1994). L-H transitions and ELMs on COMPASS-D. *Controlled Fusion and Plasma Physics, Proceedings of the 21st European Conference, Montpellier*, I:318–321.

[Vollmer et al., 1991] Vollmer, O., Ryter, F., Steuer, K. H., Wagner, F., and Zohm, H. (1991). Long pulse stationary h-mode with ELMs on ASDEX. *Controlled Fusion and Plasma Physics, Proceedings of the XVIII Conference, Berlin*, I:385–388.

[Wagner, 1994] Wagner, F. (1994). New Subjects of the H-mode. *Plasma Physics and Controlled Fusion*, 36(12):A319–A328.

[Wagner et al., 1982] Wagner, F. et al. (1982). Regime of Improved Confinement and High Beta in Neutral-Beam-Heated Divertor Discharges of the ASDEX Tokamak. *Physical Review Letters*, 49(19):1408–1412.

[Wagner et al., 1984] Wagner, F. et al. (1984). Development of an Edge Transport Barrier at the H-mode Transition of ASDEX. *Physical Review Letters*, 53(15):1453–1456.

[Wagner et al., 1994] Wagner, F. et al. (1994). The H-mode of WVII-AS Stellarator. *Plasma Physics and Controlled Fusion*, 36:A61–A74.

[Wesson, 1987] Wesson, J. A. (1987). *Tokamaks*. Clarendon Press, Oxford.

[Wesson and Sykes, 1985] Wesson, J. A. and Sykes, A. (1985). Tokamak Beta Limit. *Nuclear Fusion*, 25(1):85–88.

[Weynandts and Taylor, 1990] Weynandts, R. R. and Taylor, R. J. (1990). Dynamics of H-mode like edge transitions brought about by external polarisation. *Nuclear Fusion*, 30(5):945–949.

[Yushmanov et al., 1990] Yushmanov, P., Takizuka, T., Riedel, K., Kardaun, O. J. W. F., Cordey, J. G., Kaye, S. M., and Post, D. E. (1990). Scalings for Tokamak Energy Confinement. *Nuclear Fusion*, 30(10).

[Zohm et al., 1994a] Zohm, H., ASDEX Upgrade-Team, ICRH-Group, and NI-Group (1994a). Dynamics of the L-H transition. *Physical Review Letters*, 72(2):222–225.

[Zohm et al., 1993] Zohm, H., Lackner, K., and Ludescher, C. (1993). Statistical Analysis of Disruptions in ASDEX. *Nuclear Fusion*, 33(4):655–662.

[Zohm et al., 1995a] Zohm, H., Osborne, T. H., Burrell, K. H., Chu, M. S., Doyle, E. J., Gohil, P., Hill, D. N., Lao, L. L., Taylor, T. S., and Turnbull, A. D. (1995a). ELM Studies on DIII-D and a Comparison to ASDEX Results. *accepted for publication in Nuclear Fusion.*

[Zohm et al., 1994b] Zohm, H., Ryter, F., Fuchs, C., Herrmann, A., Kaufmann, M., Neuhauser, J., Salmon, N., ASDEX Upgrade-Team, and ICRH-,NBI-Group (1994b). Dynamic behaviour of the H-mode in ASDEX Upgrade. *Plasma Physics and Controlled Fusion*, 36(4):A129–A134.

[Zohm et al., 1994c] Zohm, H., Ryter, F., and Wagner, F. (1994c). The H-mode: Current Understanding and Extrapolability. *ISPP-16, Tokamak Concept Improvement, Edited by S. Bernabei, N. Sauthoff and F. Sindoni, SIF, Bologna ISBN 88-7794-067-0*, pages 149–162.

[Zohm et al., 1995b] Zohm, H., Suttrop, W., Büchl, K., de Blank, H., Gruber, O., Kallenbach, A., Mertens, V., Ryter, F., Schittenhelm, M., and ASDEX Upgrade-Team (1995b). Investigation of the Bifurcation Character of the H-mode in ASDEX Upgrade. *Plasma Physics and Controlled Fusion*, 37(4):437–446.

[Zohm et al., 1992] Zohm, H., Wagner, F., Endler, M., Gernhardt, J., Holzhauer, E., Kerner, W., and Mertens, V. (1992). Studies of Edge Localized Modes on ASDEX. *Nuclear Fusion*, 32(3):489–494.